12-2024

A Mass Balance Model of the Great Salt Lake, UT With Adaptive Management Applications

Diana Dunn
Utah State University

A MASS BALANCE MODEL OF THE GREAT SALT LAKE, UT WITH ADAPTIVE MANAGEMENT APPLICATIONS

by

Diana Dunn

A thesis submitted in partial fulfillment
of the requirements for the degree

of

MASTER OF SCIENCE

in

Civil and Environmental Engineering

Approved:

Brian Crookston, Ph.D., P.E. Major Professor	Bethany Neilson, Ph.D. Committee Member
Som Dutta, Ph.D. Committee Member	D. Richard Cutler, Ph.D. Vice Provost of Graduate Studies

UTAH STATE UNIVERSITY
Logan, Utah

2024

ABSTRACT

A Mass Balance Model of the Great Salt Lake, UT with Adaptive Management Applications

by

Diana Dunn, Master of Science

Utah State University, 2024

Major Professor: Dr. Brian M. Crookston
Department: Civil and Environmental Engineering

The Great Salt Lake, Utah, USA is a critical ecologic and economic asset. In 1959, it was bisected into north and south sections by an east-west rockfill, railroad causeway. Distinct water surface elevation and density gradients have formed because all streamflow enters the lake through the south section. The north section has reached halite saturation, around 300 g/L, while the south section has fluctuated between 130-180 g/L in recent years. Ecologic and economic productivity of the lake relies on maintaining a salinity threshold of 180 g/L within the south section. Since construction, various openings in the causeway have been built to maintain healthy salinity levels by allowing water and salt mass exchange between the sections. Most recently the New Breach was constructed and includes a submerged rock berm that can be raised or lowered to control exchange flows in response to varied hydroclimatic conditions.

Great Salt Lake water level and salinity are interdependent and functions of multiple variables which complicates development of adaptive management strategies. To inform utility of the berm, this research focused on developing a mass balance model of the Great Salt Lake that can predict water elevation and salinity in response to various hydroclimatic conditions and New Breach berm heights. In developing the model, relevant hydroclimatic data was gathered and evaluated which highlighted current data limitations at the lake and informed use of available lake datasets. Results from this study validated the model formulation and utility. Through model application, the berm was found to be a useful adaptive management tool, but long-term salinity management necessitates minimizing upstream water withdrawals to increase streamflow to the lake. The model and datasets developed herein are open access and will aid future work at the Great Salt Lake as conditions continue to evolve.

(160 Pages)

PUBLIC ABSTRACT

A Mass Balance Model of the Great Salt Lake, UT with Adaptive Management Applications

by

Diana Dunn, Master of Science

Utah State University, 2024

Major Professor: Dr. Brian M. Crookston
Department: Civil and Environmental Engineering

The Great Salt, Utah, USA is a saline lake that provides critical habitat for ecologic communities and generates $1.3 billion annually. It has gone through detrimental change since the 20th century. Streamflow reaching the lake has been decreased by upstream withdrawal for industrial and municipal use, causing the lake level to drop and salinity to increase to unhealthy levels. Further, in 1959, it was segregated into north and south sections by a railroad causeway. Due to the causeway and limited exchange of water through two bridges, the lake sections have significantly different water surface elevation and salinity levels. The most recent bridge in the causeway, known as the New Breach, was constructed with a rock berm that is raised or lowered to control exchange of water between the sections and can be used to maintain healthy salinity levels. Lake managers have utilized the New Breach berm to adaptively manage salinity; raising it 1.2 m in 2022 and another 1.5 m in 2023 in response to record low lake

level and high salt concentrations in the south section. To inform future adaptive management decisions such as these, this research developed a model that can predict salinity and water level of both sections in response to various inflow, climate, and berm height conditions. Results from application of the model showed that the New Breach berm is a helpful tool, but long-term salinity management of the Great Salt Lake will require increasing streamflow to the lake. Additional analysis of data gathered for use in developing the model highlighted data limitations and how monitoring of the Great Salt Lake can be improved in the future to better aid decision making.

ACKNOWLEDGMENTS

This study was funded by the State of Utah through the Department of Natural Resources Forestry, Fire and State Lands and through the Utah Water Research Laboratory at Utah State University. Throughout my time at USU I had the support and guidance of a phenomenal committee: Dr. Som Dutta, Dr. Bethany Neilson and my faculty advisor Dr. Brian Crookston. Modeling guidance and field support was supplied by Dr. Dutta whose provision of New Breach flow models was invaluable. Thank you to Dr. Neilson who devoted her time and expertise toward every aspect of this research. And special thanks to Dr. Crookston whose kind oversight creates an encouraging environment for all his graduate students. He exemplifies hard work and humility which inspires those who work alongside him.

Thank you to my friends and fellow graduate students, I cherish the time spent together in and outside the lab. And a final thanks to my parents. Your unconditional love and support have made me who I am today and I am grateful for your continuous encouragement throughout my time at USU.

Diana Dunn

CONTENTS

Page

LIST OF TABLES

Page

LIST OF FIGURES

Page

NOMENCLATURE

AWWA	American Water Works Association
BR	Bear River
CI	Confidence interval
CLF	cold low-flow
CSTR	continuously stirred tank reactor
DBL	deep brine layer
DWiR	Utah Department of Wildlife Resources
EOS	equation of state
EQL	Environmental Quality Lab
FB	Farmington Bay
GD	Goggin Drain
GSL	Great Salt Lake
GSLBSC	Great Salt Lake Brine Shrimp Cooperative
GSLFM	Great Salt Lake Fortran Model
HLF	hot low-flow
L	Lakeside
MAPE	mean absolute percent error
NS	north to south
NWIS	National Water Information System
PC	principal component
PCA	Principal Component Analysis
psu	practical salinity units
RO	runoff

RMSE	root mean squared error
RMSPE	root mean squared percent error
SN	south to north
UBL	upper brine layer
UCC	Utah Climate Center
UDNR	Utah Department of Natural Resources
UDWQ	Utah Department of Water Quality
UPR	Union Pacific Railroad
USGS	U.S. Geological Survey
UGS	Utah Geological Survey
USU	Utah State University
UWRL	Utah Water Research Lab
WSE	water surface elevation
WR	Weber River
A	surface area [m^2]
a	DGSLM calibration parameter
b	rating curve fit parameter
C	salt concentration, equivalent to salinity [$kg/m^3 \approx g/L$]
Cc	corrective coefficient for tuning parameter, c
C_d	drag coefficient for air
C_{sat}	salt concentration of water at saturation [kg/m^3]
C_w	discharge coefficient for water
CF	Correction factor for $\%C$ conversion
E	evaporation volume flux [m^3/d]

E_d	evaporative depth off GSL [m/d]
E'	bulk turbulent diffusion coefficient [m^3/kg·d]
$\%\varepsilon$	measurement uncertainty
e_a	actual vapor pressure of air [kPa]
e_s	saturation vapor pressure at water surface [kPa]
G	volumetric inflow from groundwater [m^3/d]
K_E	bulk latent heat transfer coefficient [mm·s/m·kPa·d]
M	total dissolved salt mass flux [metric tons/d]
P	precipitation volume flux [m^3/d]
P_d	depth of precipitation over the Great Salt Lake [m/d]
p_{site}	atmospheric site pressure [kpa]
Q	surface water discharge [m^3/d]
q	groundwater discharge [m^3/d]
R_n	net energy available at water surface [MJ/m^2 ·d]
SC	specific conductance µS/cm]
SG	specific gravity
T	temperature [°C]
TDS	Total dissolved solids [kg/m^3]
T_a	mean air temperature [°C]
$T_{a,max}$	maximum daily air temperature [°C]
$T_{a,min}$	minimum daily air temperature [°C]
T_d	dewpoint temperature of air [°C]

V	water velocity [m/s]
$\forall$	volume [m^3]
α	rating curve fit parameter
β	water activity coefficient
γ	psychrometric constant [kPa/°C]
Δ'	saturation vapor pressure gradient [kPa/°C]
λ_v	laten hear of evaporation [MJ/kg]
v_w	wind velocity at water surface [m/s, m/d]
ρ	density of water [g/cm^3, kg/m^3]
ρ_a	density of air [g/cm^3]
ρ^0	density of pure water [g/cm^3]
ρ_{20}	density of water at 20 °C [g/cm^3]
σ	standard deviation
σ_T	total standard deviation
$\%C$	percent salinity
$\%_d$	percent difference

1 INTRODUCTION

1.1 Background and Motivation

The Great Salt Lake (GSL), located in Utah, USA, is the remnant of the historical Lake Bonneville (Bedford, 2005). GSL is the largest saline lake in the western hemisphere with salinities that can exceed 250g/L, among the highest in the world (Null, 2020). Its waters, neighboring wetlands, and springs support diverse biota and economic industry. Millions of resident and migratory birds rely on the lake's macroinvertebrate populations (Donnely, 2020; Yang et al., 2020) while brine shrimp and minerals harvested from the lake's hypersaline brine generate $1.3 billion annually to the state of Utah's economy (Bioeconomics, 2012; Wurtsbaugh, 2014; Figure 1).

Figure 1

Anthropogenic and Environmental Linkages within the Great Salt Lake Watershed

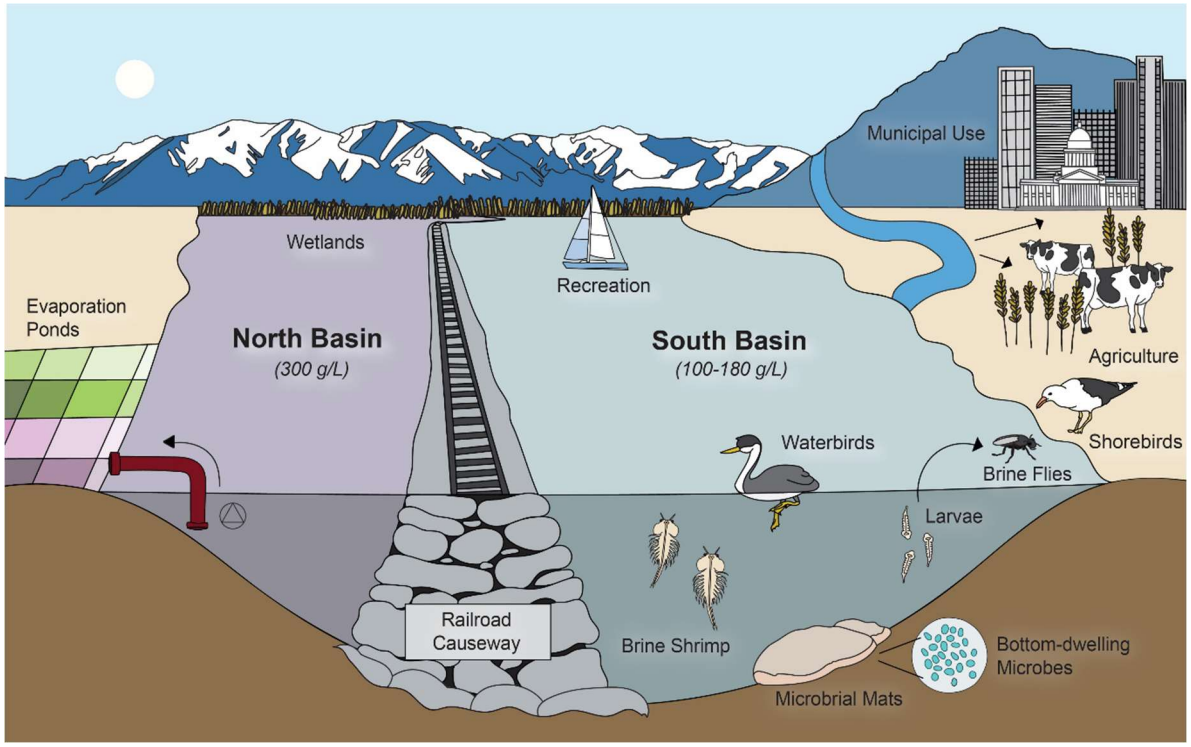

Note. Visual created with help from the UWRL communication team.

An East-West rockfill, railroad causeway was constructed in 1959, segregating the lake into north and south basins (Figure 1). The north basin has salt concentrations near saturation, around 300 g/L, rendering it inhabitable (Wurtsbaugh, 2014). All freshwater inflow to the lake enters the south section causing it to be more dilute with salinity that fluctuates from 50-180 g/L, conducive for brine fly and brine shrimp habitat (Null et al., 2013). Water within the GSL's main tributaries is diverted for agriculture and metropolitan/industrial consumptive use, affecting the critical balance between inflows and outflows that determines its volume (Null & Wurtsbaugh, 2020). The effect of these

diversions has been compounded by variable climate patterns (Wang et al., 2010; Baxter and Butler, 2020) causing the lake to exhibit a decline in annual, average lake level. GSL reached a record low in November 2022 and has recorded south section salinity values that exceed the optimal range for ecosystem health, >160 g/L, since 2021 (GSL Salinity Advisory Committee, 2021; Brown et al., 2023). These conditions have caused millions of dollars in damage to the economic industry and long-lasting harm to the ecologic communities (Potential Cost of Declining Great Salt Lake, 2019).

Different management approaches have been taken to slow the decline in lake volume including enhancing water conservation, improving watershed management, and optimizing agricultural tools (Great Salt Lake Strike Team, 2024). Additionally, various modifications have been made to the causeway throughout its history to adaptively manage salinity and water surface elevation in the south section (Figure 2). It was originally constructed with two culverts allowing for limited exchange of water between the sections. Most recently, the New Breach was opened in 2017 to replace the culverts that were decommissioned in 2012/2013. This New Breach includes an adjustable rock berm that can be raised or lowered to control bi-directional flow exchange, compensating for changes in climatic cycle and inflow. For example, in July of 2022 the Utah Department of Natural Resources (UDNR) raised the berm 1.2 m to limit the volume of north section water entering the south section, counteracting the historic low lake level and high salinity. Despite this raise in berm height, unhealthy salinity levels persisted. It was raised again in 2023, in preparation for a substantial spring runoff that returned the south section to a healthy salt concentration.

Figure 2

Great Salt Lake Railroad Causeway Modification Timeline from 1959 to Present

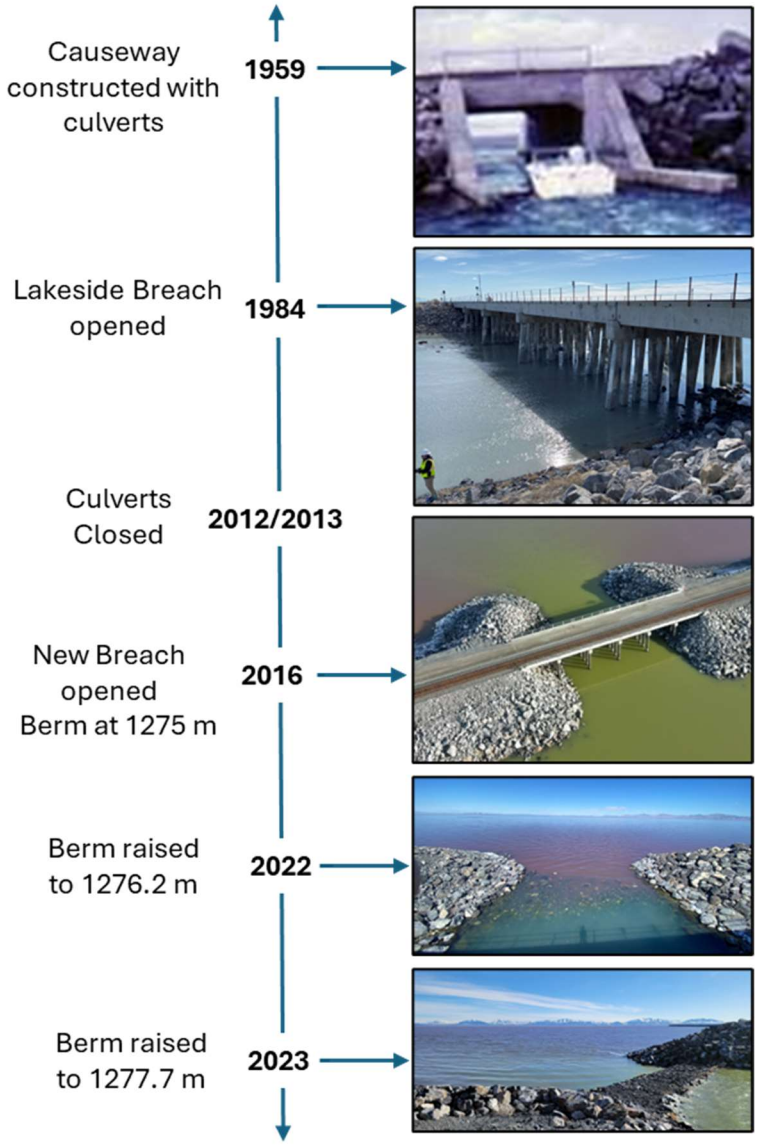

Note. 1959 culvert photo courtesy of Union Pacific Railroad, 2016 berm photo courtesy of Brian Crookston.

With each berm modification and shift in climatic conditions, GSL internal salt cycling changes. Knowledge of the key drivers of lake level and salinity fluctuations and the lake's response to different berm heights is necessary to effectively manage salinity in the south section. Various studies have been carried out to inform past salinity management (Brown, 2023; Merck & Tarboton, 2023; Yang, 2020; Naftz, 2014). Mass balance models have also been developed for the GSL to understand how changes to the causeway effect the relationship between lake level and salinity and to determine the most productive mechanisms for salinity management (Holley and Waddell, 1976; Wold et al., 1997; Loving et al., 2000; Mohammed & Tarboton, 2012; GSLIM, 2019; Jewell, 2021). Further, multiple flow models have been developed for the New Breach by Larsen (2024) and Rasmussen (2022) which have informed the generation of empirical rating curves that can predict exchange flows as a function of berm elevation and the density/elevation gradients between the two sections.

While informative, previous GSL mass balance models have yet to incorporate the newly developed rating curves nor have they utilized all available salinity data at the lake. In addition, no studies have been conducted or models developed to quantify lake response to incremental changes to berm elevation located at the New Breach over a spectrum of lake conditions. Managing for sustainability requires an understanding of management actions and their consequences on dynamic systems (UDNR, 2013). Therefore, as lake conditions continue to evolve, there is an immediate need to determine the most effective means to adaptively manage salt concentrations in response to a variety of circumstances.

1.2 Research Objectives and Questions

This study seeks to fill the above-mentioned gaps in knowledge and inform sustainable salinity management of the Great Salt Lake within the context of social, economic, and environmental wellbeing. To do so, a comprehensive salinity dataset was curated, and a process based, mass balance model was developed that accurately predicts lake level and salinity in response to varying hydrologic conditions, exchange scenarios at the New Breach, and management actions. Application of the model also highlighted effective strategies for maintaining healthy salinity levels at the lake for current and future generations. The main objectives of this study were:

1. Compile a comprehensive salinity dataset for the Great Salt Lake since the New Breach opened, 1 January 2017, and derive a representative time series for use in model formulation and testing.
2. Formulate a Great Salt Lake mass balance model that can predict lake level and salinity.
3. Evaluate the performance of the GSL model using historical lake elevation and salinity observations.
4. Use the validated model to simulate management scenarios and explore effective adaptive management strategies.

While completing these objectives, specific research questions were assessed:

[Q1] What inflow, salinity, climatic and lake elevation data are available for use in the GSL mass balance model?

[Q2] How can historical salinity datasets be combined to create a dataset with adequate temporal and spatial resolution for mass balance modeling?

[Q3] How should a Great Salt Lake mass balance model be formulated to accurately predict lake elevation and salinity?

[Q4] How can the berm at the New Breach be used to effectively manage salinity in the south section of the GSL?

2 SEASONAL WATER AND SALT CYCLING AT THE GREAT SALT LAKE, UTAH DUE TO THE NEW CAUSEWAY BREACH AND RECENT HYDROLOGIC DRIVERS

2.1 Introduction

Saline lakes are found on every continent and constitute nearly half the total volume of lakes worldwide (Hannam et. al. 1993). These lakes are important ecologic, cultural, and economic assets, yet increased water diversions or withdrawals, point and non-point source pollution, hydroclimate change, and increasing extraction activities (e.g., mineral harvesting) have negatively impacted many saline lakes. These threats have reduced lake biodiversity, altered salinity composition and limnology, and will continue to cause lake desiccation (Williams, 2003). Examples of saline lakes include Lake Urmia in Iran, Mono Lake in California, USA, the Aral Sea in Kazakhstan, and the Great Salt Lake among others (Wurtsbaugh et al., 2017).

The Great Salt Lake (GSL), a remnant of ancient Lake Bonneville, is located in northern Utah, USA. It is the largest inland saline lake in North America, the 8th largest in the world and has been significantly influenced by human activity. An east-west rockfill railroad was constructed in 1959 that segregated the lake into north and south sections. It was constructed with two culverts to facilitate water and salt mass exchange between the sections, however distinct water surface elevation and density gradients have formed causing salinity, water residence time, ecologic community structure, and nutrient dynamics within the Great Salt Lake to be heterogeneous.

Despite alterations to its natural state, the lake supports a productive endemic ecosystem with brine shrimp, brine flies, various phytoplankton, and benthic microbial communities (Brown, 2023). The GSL is used by large avian populations for breeding and migration and is one of a limited number of wetland sites within North America's Pacific Flyway (Donnely, 2020; Yang et al., 2020). Harvested brine shrimp cysts are used as food sources for global commercial aquaculture operations. The lake is estimated to contain 90 billion USD in minerals; minerals extracted from the hypersaline brine are utilized for various salt-containing products, metal alloys, fertilizer, and in the production of glass and paper (Bioeconomics, 2012).

During the past 50 years the Great Salt Lake has experienced significant lake level fluctuations and, due to upstream water withdrawals for agriculture and periodic droughts, record high salt concentrations (Null and Wurtsbaugh, 2020, Williams et al., 2020). These conditions have threatened the livelihood of brine shrimp and other organisms (Barnes and Wurtsbaugh, 2015; Lindsay et al., 2019) and caused loss of habitat for water and shorebird populations (Wurtsbaugh, 2014). Lake fluctuations have also caused millions of dollars in economic damage to brine shrimp cyst harvesting and mineral extraction industries (Cost of Declining Great Salt Lake, 2019). Dry sections of the lakebed are exposed to wind erosion. The transported dust poses a significant human health risk (Perry, 2019) for the 2.7 million residents of the Salt Lake City metropolitan area, located approximately 20 kilometers east of the GSL.

To retain ecologic and economic function of the south section, lake levels and salinity must be managed in a way that balances human and ecologic needs. This requires

an understanding of lake response to anthropogenic and environmental stressors. The GSL is challenging due to unique lake conditions, uncertainties with hydrologic processes at the lake, the complex hydraulics of water and salt mass exchange across the causeway, and other uncertainties such as unmeasured seepage through the causeway and groundwater conditions. Moreover, various lake stakeholders collect water quality datasets using different methodologies and instruments which presents additional challenges.

Monitoring salinity and its forcing variables at appropriate spatial and temporal scales is crucial for evaluating previous management actions and developing future management strategies. Currently, monitoring at the lake is at the center of discussion and collaboration between researchers and leads at the State of Utah (Great Salt Lake Strike Team, 2024). Although multiple entities monitor water quality parameters to describe salinity at the lake, they use different methods (Great Salt Lake Salinity Advisory Committee, 2020) and prior to 2020 there was minimal cross entity coordination of field or analytical methods (Great Salt Lake Salinity Advisory Committee, 2020). Previous salinity quantification and modeling efforts have not incorporated all available salinity datasets due to uncertainties, lack of methods to accurately estimate salinity, or an inability to combine data from different sources (Brown, 2023; Merck and Tarboton, 2023; Yang, 2020; Jewell, 2021; Great Salt Lake Strike Team, 2023; GSLIM, 2019).

Therefore, to support adaptive lake management efforts this study was conducted to identify the primary drivers of salinity for the Great Salt Lake, to gain new insights

into lake dynamics, and to explore current data limitations. This was accomplished by 1) compiling all available water quality data across multiple entities, 2) developing a new specific conductance salinity conversion equation applicable to hypersaline environments, and 3) quantifying the variance across sampling locations, datasets and analytical methods. Once the curated dataset was prepared, principal component analysis was performed on salinity observations and key lake mass balance terms to characterize the spatial and temporal patterns of salinity and its controls within the southern section of the lake. This provided insights into lake dynamics and allowed for filtering of the south section salinity data to derive time series that reflected general lake conditions. Finally, this study used the south section time series data to consider adaptive lake management efforts by quantifying the seasonal influence of salinity forcing variables via correlation analysis. A discussion of the implications of lake stressors and data limitations on sustainably managing the lake for current and future generations is also provided.

2.2 Study Area

The Great Salt Lake experiences a semi-arid climate with inflows primarily provided to the south section via three rivers and their corresponding subbasin drainage areas (Figure 3). Being a closed basin lake, it is sensitive to climate variability where fluctuations in its surface area and volume are determined by the balance between water inflows (river discharge, precipitation, surface runoff and groundwater seepages) and evaporation (Wang et al., 2010). Water from the Great Salt Lake's main tributaries is diverted for agriculture and metropolitan consumptive use influencing the lakes natural

hydrologic balance and compounding the effects of long-term periods of drought. Great Salt Lake elevation also varies interannually. Water surface elevations typically fluctuate less than 1 m per year, with net increase from November to June due to precipitation (in the form of snow) and spring runoff and net decrease from July to October due to increasing temperature and a dry climate (Figure 3).

Figure 3

Location and Key Features of the Great Salt Lake Including its Bays, Tributaries, and the New Breach.

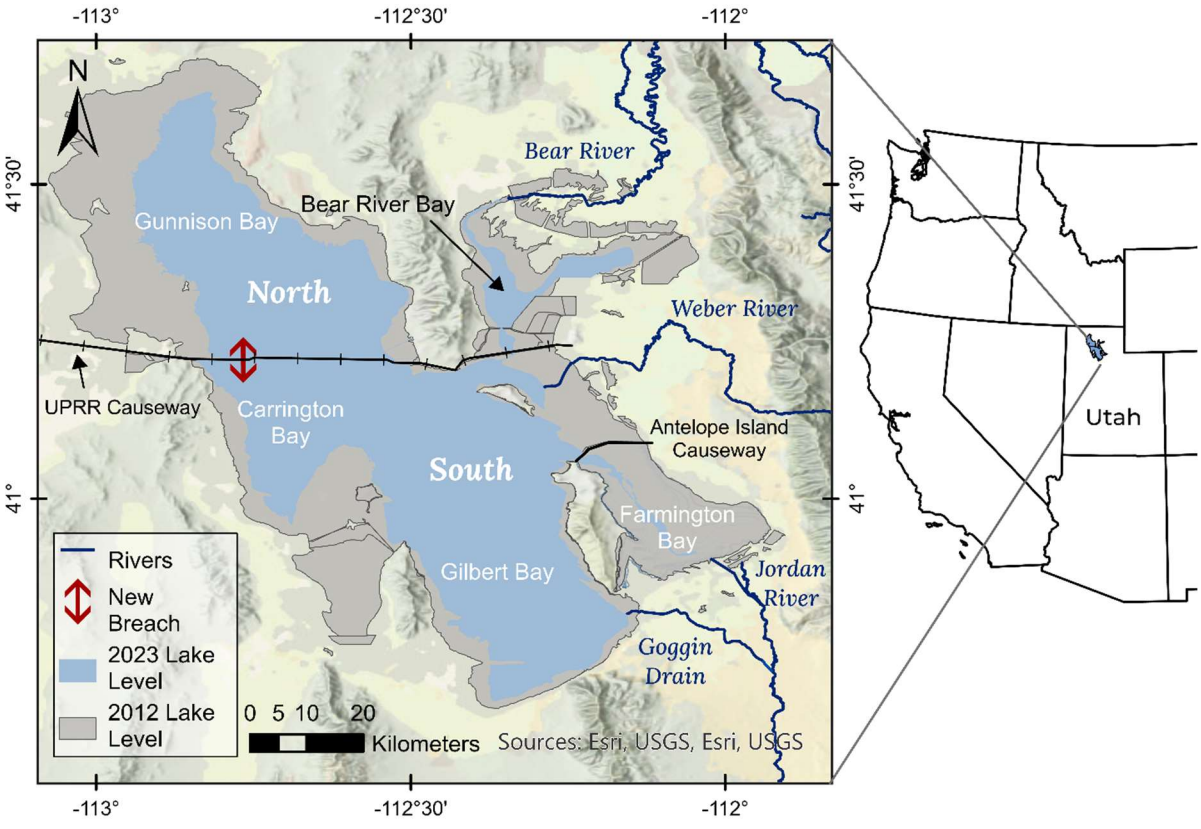

Figure 4

Gilbert Bay Water Surface Elevation and Salinity

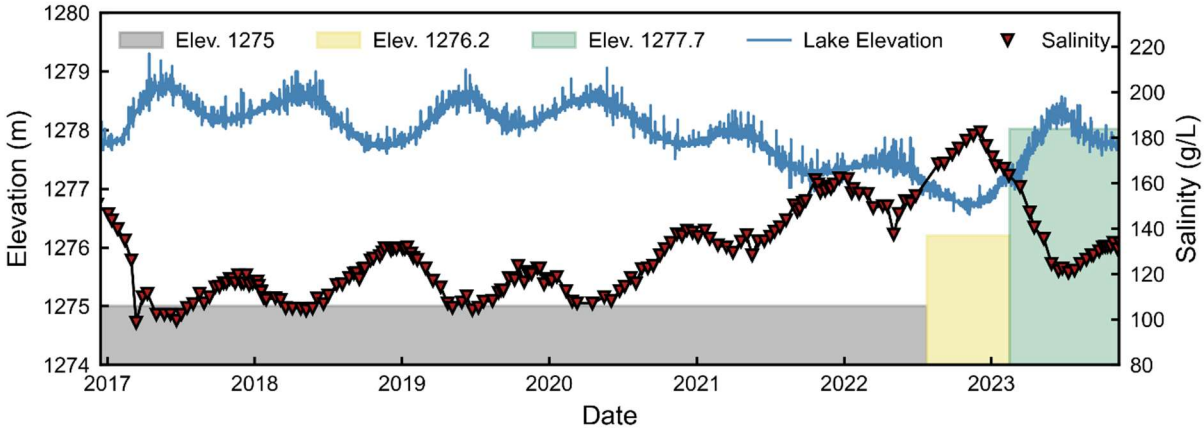

Note. Water surface elevation data was taken from USGS site 10010000 and salinity data from DWiR site 3510. The gray shaded region represents the time period where the elevation of the New Breach berm was 1275 m, yellow shaded region represents the time when the New Breach berm was at 1276.2 m and the green shaded region represents the time when the New Breach berm was at 1277.7 m.

Prior to anthropogenic influence, GSL salinity ranged from 60-330 grams per liter (g/L) but was generally less than 200 g/L (Null et al., 2013). The east-west rockfill, separates the lake which is comprised of Gunnison Bay (north section) and Gilbert/Carrington Bay (south section)(Marden et al., 2020; Figure 3). The lake is further partitioned by a vehicle causeway segregating Farmington Bay in the southeast corner of the lake (Figure 3). Currently, Gunnison Bay has salt concentrations near saturation, around 330 g/L, while concentrations south of the causeway fluctuate from 50-180 g/L (Wurtsbaugh, 2014; Figure 3). Elevation and density gradients between the segregated sections of the lake are present because river inflows only enter the south section, which

has a water surface commonly 0.3-0.6 m higher in elevation than the north section. The south section also features two well defined intermittent brine layers, the upper brine layer (UBL) and the deep brine layer (DBL) (Madison, 1970). The DBL is formed by the higher salinity north waters entering the south section through the causeway and plunging below the less saline water in the UBL (Naftz, 2014). This DBL disappears without northern water additions or significant mixing events due to high winds.

Alterations to the rockfill causeway have occurred periodically for various reasons. For many years several culverts allowed for limited mass exchange between the two lake sections. In 1984, an additional breach was added on the far west side of the causeway, known as the Lakeside Breach, to reduce the 1.5 m rise in the south section lake elevation from flooding (Gwynn, 1986). However, due to drought and historically low lake levels in the 2000s, the Lakeside Breach became ineffective in exchanging flows (Jewell, 2021). The culverts were decommissioned in 2013 and 2014 since they had subsided into the lakebed and deteriorated (White and Null, 2015). A 55 m breach, known as the New Breach, was opened in 2017 to once again provide exchange flows (Figure 5). It features a submerged rock berm that can be raised or lowered to adaptively manage the buoyancy-driven bi-directional (north to south and south to north) flow exchange (Rasmussen, 2022); water flows through the New Breach from south to north driven by the water surface elevation gradient while also flowing north to south due to the density gradient (Rasmussen et al., 2021).

Figure 5

Aerial Photos of the New Breach

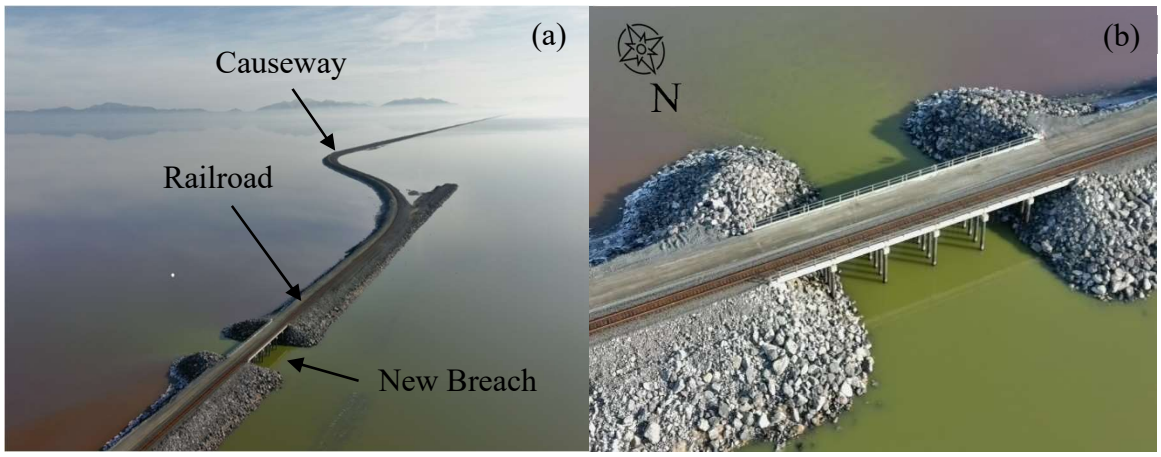

Note. Photos courtesy B. Crookston.

Since 2017 and completion of the New Breach, the Great Salt Lake has exhibited a decline in annual, average lake level reaching a record low of 1276.7 m in November 2022 due to decreased streamflow reaching the lake and the recent megadrought experienced across the southwest United States (Great Salt Lake Strike Team, 2023; Figure 4). Salinity values that exceed optimal range for ecosystem health (>160 g/L) have been recorded since 2021, emphasizing the need for sustainable management of the Great Salt Lake and its watershed (Great Salt Lake Salinity Advisory Committee, 2021; Brown et al., 2023; Figure 4). To reduce south section salinity levels, the New Breach berm was raised from El. 1275 m to El. 1276.2 m in July 2022, effectively lessening north to south flow and mass loading. The berm was raised above lake surface elevations to El. 1277.7 m prior to spring runoff in 2023 (Figure 4) to further limit mass flux; however, the berm was overtopped and partially breached prior to summer 2023. To increase flows into the northern section in

2024, the berm was not repaired and lowered but rather the breach was widened with the entire berm overtopped Spring 2024 and creating further erosion.

2.3 Methods

2.3.1 Data Collection and Compilation

Data pertaining to the opening of the New Breach began January 2017. Since then, multiple entities within Utah gathered and reported hydrologic data for the Great Salt Lake (Table 1; Appendix C) that includes the Utah Geological Survey (UGS), the US Geological Survey (USGS), Utah Division of Wildlife Resources (DWiR), HDR Engineering, the Great Salt Lake Brine Shrimp Cooperative (BSC), and Utah State University (USU) (Great Salt Lake Salinity Advisory Committee, 2020). Observations of salt concentration, C(g/L), from five entities were compiled into a single Great Salt Lake dataset (Dunn, 2024a) which required determining appropriate methods for converting various water quality measurements from these entities to C. This also required the development of a conversion equation for specific conductance, SC (μS/cm), since existing, published conversion methods have not been developed for hypersaline environments. Additional hydrologic data including New Breach flow exchange, streamflow and climate variables were gathered to quantify New Breach salt mass fluxes, river inflows, and evaporation for use in exploring seasonal controls on south section SC.

Table 1

Open Water Salinity Datasets

Entity	Parameter Reported	Number of South Section Sites	Measurement Type	Frequency	Depth	Period of Record (Yr./Mo/Day)
USGS	SC (µS/cm)	13	in-field	twice a year	0.3 m increments	2017/1/1 - 2022/12/31
	ρ (g/cm^3)	9	sample	monthly, bi-monthly	0.2-0.5 m below surface, 0.5m above bottom	
	SG					
UGS	ρ (g/cm^3)	5	sample	4 months	1.5 m below surface, 0.15 m from bottom	2017/1/1-2022/5/23
DWiR	$\%C$	16	sample	2 weeks	at water surface	2017/1/1-2022/12/31
HDR	SC (µS/cm)	6	in-field	3 months	0.15 - 0.3 m increments	2017/1/1 - 2021/12/1
	ρ (g/mL)				at surface, 1.5 m increments, 0.3 m above bottom	
*BSC	C (g/L)	2	in-field	monthly	1, 3, 5, 6, 7 and 8-m	2017/1/1 - 2021/11/4

Note. BSC reports salinity in g/L computed by a YSI 556 conductivity meter using conductivity and temperature readings in-situ.

New Breach Salinity

From August 2020 to February 2022, Utah State University's Utah Water Research Lab (UWRL) has nearly continuous 15-minute SC data and monthly water samples taken at the New Breach that were collected as part of the field campaign outlined in Rasmussen (2022) (Table C3). The 15-minute continuous SC data was collected using two In-Situ AquaTroll 600 Multiparameter Sondes placed on the north and south sides of the New Breach. Due to dropping lake elevations during the recent drought, these instruments were relocated from February 2022 to February 2023 to a vertical slotted casing attached to a pier on the north side of the bridge (Figure 6), directly south of the berm, with instruments placed at an elevation of 1272.7 m (in the DBL -near the bottom of the water column) and at 1277 m (in the UBL - middle of the water column). North and south section water samples were also collected monthly and analyzed at the Utah Water Research Lab (UWRL) for density, ρ (g/cm^3), and total dissolved solids, TDS (g/L) (J. McLean, personal communication, 20 April 2023; Rasmussen, 2022).

Figure 6

Field Data Instrumentation and SC Profile Location at the New Breach

South Section Open Water Salinity

Each entity measured various water quality variables and utilized different field methodologies for their data collection. Therefore, it was necessary to gather the water quality data then determine and develop appropriate methods to convert observations to S so that the data could be compared and easily combined. All available data was converted and combined into the comprehensive dataset. This study focused on the open water portion of the south section, UBL thus a data subset pertaining to measurements from Gilbert Bay and Carrington Bay were analyzed herein. During the period of analysis, USGS measured south section water sample ρ, temperature, T (°C), and SC for 8 sites in the south section and at the New Breach, which was compiled from the National Water Information System (NWIS) (U.S. Geologic Survey, 2023;Figure 7; Table 1). UGS measured ρ, T, and ion composition at 5 sites in the south section (Figure 7; Table 1). This data was compiled

from the Brine Chemistry database available through the Utah Department of Water Quality (UDWQ) (Utah Geological Survey, 2020). HDR Engineering measured ρ and SC at 5 sites in the south section and at the New Breach (Figure 7; Table 1). Reported HDR data pertained to the Great Salt Lake Causeway Culvert Closure and Bridge Construction Project, accessed through the Utah Division of Water Quality (UDWQ)(Utah DWQ, 2022). DWiR collected percent salinity ($\%C$) data at 16 sites, only in the south section (Figure 7; Table 1, Great Salt Lake Salinity Advisory Committee, 2020) while BSC reported C at two sites in the south section (Brown, 2022; Figure 7).

Figure 7

Map of Data Collection Sites Including South Section Open Water Salinity Sampling, Inflow Gage Stations, and Climate Data Sites.

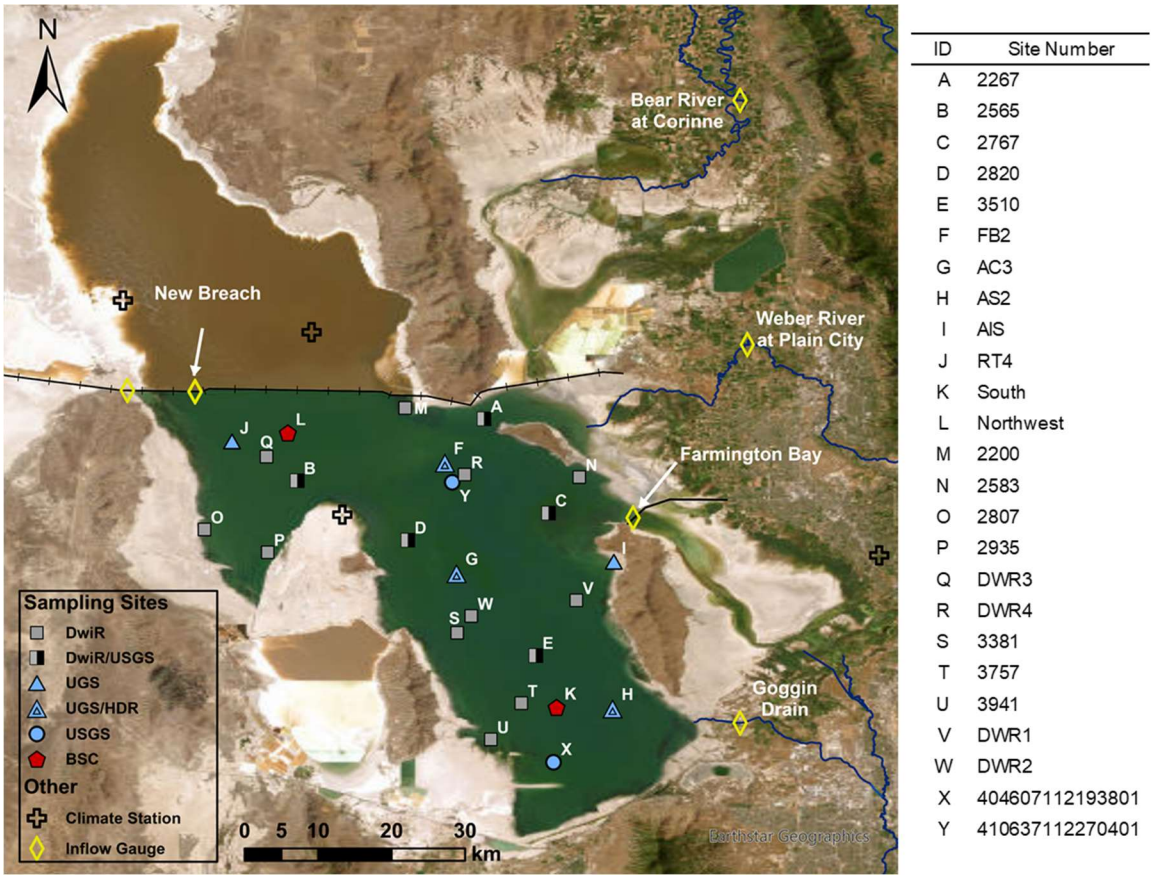

ID	Site Number
A	2267
B	2565
C	2767
D	2820
E	3510
F	FB2
G	AC3
H	AS2
I	AIS
J	RT4
K	South
L	Northwest
M	2200
N	2583
O	2807
P	2935
Q	DWR3
R	DWR4
S	3381
T	3757
U	3941
V	DWR1
W	DWR2
X	404607112193801
Y	410637112270401

Note. The site key includes the letter ID associated with each sampling location site number. Only sample sites within Gilbert Bay and Carrington Bay were included in the analysis.

USGS sampled ρ 0.2-0.5 m below the lake surface and 0.5 m above the lake bottom (Table 1). Samples were analyzed at the USGS laboratory following published protocols with ρ values adjusted to 20 °C equivalent values (USGS, 2002; C. Rumsey, personal correspondence, 8 June 2023). UGS sampled ρ 1.5 m below the water surface and 0.15 m

above the lake bottom (Table 1). Samples were also analyzed at a commercial lab for ion composition (Great Salt Lake Salinity Advisory Committee, 2020; Figure 7). HDR Engineering analyzed samples for ρ at the water surface, in 1.5 m descending intervals, and at 0.3 m from the lake bottom (Utah DWQ, 2022; Table 1). USGS, UGS and HDR report an accuracy of ±0.001 g/cm^3 for all ρ measurements (Great Salt Lake Salinity Advisory Committee, 2020a).

Both USGS and HDR datasets include SC data measured in the field; however, USGS SC was determined in the laboratory from collected sample which were measured using a multiparameter sonde, ±5%. HDR measured vertical profiles of SC in the field, using an In-Situ Aqua TROLL multiprobe water quality meter (±0.8%); depth intervals included: every 10 cm for the first meter, every 0.3 m from 1 m down to the beginning of the DBL, and every 15 cm in the DBL (Table 1). BSC also conducted vertical profiling, measuring SC at 1, 3, 5, 6, 7, and 8 m depths using a YSI-556 multimeter with an accuracy of ± 0.5%. SC profiles were then converted to C and corrected using a regression equation (Brown et al., 2022 Table 1). Finally, DWiR collected $\%C$ data at the water surface using a refractometer with an accuracy of ± 0.2% (Table 1).

New Breach Discharge

Flows through the New Breach are a significant challenge to estimate due to 1) observed daily fluctuations and lack of high frequency discrete discharge measurements, 2) the high salinity content and water density difference across the New Breach, 3) the buoyancy-driven bi-directional flow pattern common to the New Breach, and 4) the geometry of the New Breach opening and periodic adjustment in height to the submerged

rock berm. To consider these challenges, several new models were developed by USU to predict south to north (SN) and north to south (NS) discharge, Q (m^3/s), as formulated by Larsen (2024). A deep neural network (DNN) model was developed to predict 15-minute Q estimates (Larsen 2024) for the 1275 m berm case and a Generalized Area Based Index (GABI) model for the 1276.2 m berm case.

The input for the DNN model consisted of the USGS Acoustic Doppler Current Profiler (ADCP) up-looker data (sampled at 15 min frequency) that recorded velocities in 10 equidistant cells. An 11th cell was added to complete the velocity profile and mimic a no slip boundary, due to a blanking distance (no observed velocity near the berm surface). The DNN model output was informed by discharges estimated by an index velocity rating curve developed by USGS for exchange flows at the New Breach. 80% of the data was used for training the DNN model with 10% reserved for validation and 10% used for testing. For the testing data, the trained DNN had the Nash-Sutcliffe Efficiency, NSE, of about 0.95. Further, the accuracy of the DNN was blind tested using the USGS discrete monthly measurements. The root means square error (RMSE) was found to be about 0.5 with an NSE of 0.8, which indicates that the DNN model effectively followed the true value curve comprised of USGS data.

The GABI model is similar in principle to the DNN model as it is also based upon the USGS up-looker velocity data; however, it is able to consider the 1276.2 m berm and three distinct flow cases: bi-directional flow and either SN or NS unidirectional flows. The GABI model was developed because there were not enough discrete flow measurements available for the 1276.2 m berm scenario to train a deep neural network. Thus, GABI uses

the measured velocity and the known area of the cross-section to estimate the NS and SN flow through the breach. To accomplish this, Larsen (2024) estimated the vertical location of any interface between NS and SN flows via a hydrostatic analysis based upon the difference between lake elevations and density on either side of the New Breach, referencing the top of the berm (note that the USGS ADCP does not identify the exact interface location due to the 10-cell approach for the vertical velocity profile). The available ADCP measurements are assigned to the vertical midpoint of each cell with linear interpolation used between. This interface location and augmented vertical velocity profile is then used to estimate any discharges to the north or south sections of the lake. NSE for the GABI model was 0.7 and RMSE was 0.6.

A daily time series of New Breach discharge was developed utilizing monthly discrete Q measurements from USGS, retrieved from NWIS, and outputs from the USU models. From January 2017 to July 2017, the discrete measurements were linearly interpolated. From July 2017 to July 2022, a daily average of the 15-minute DNN model discharge estimates were used and from August 2022 to December 2022, the GABI model outputs were used. Any gaps in the USU models were filled with linear interpolations of the discrete Q data.

River Inflow

USGS measured continuous stream flows to the south section of the Great Salt Lake at Farmington Bay Bridge (FB), Weber River (WR) at Plain City, UT, Goggin Drain (GD), and the Bear River (BR) near Corinne, UT (Figure 7; Table C3). Limited discrete Q measurements were taken monthly or bimonthly at the BR Bay Bridge where there

currently is no gaging station due to ice flows and bed loads. However, these measurements are significantly different from the Corinne gage, which is approximately 110 km from this BR-GSL confluence. Flows pass through the Great Salt Lake Bird Refuge between the Corinne gage and the confluence, which is also not gaged. Methods used to measure continuous and discrete discharge are summarized in Turnipseed and Sauer (2010) and Levesque and Oberg (2012). USGS New Breach Q measurements and continuous discharge records from the four major tributaries were also gathered from NWIS using the dataretrieval package in Python (Horsburgh, 2022; Table C3).

Climate

Continuous hourly climatic data was available at three sites at the Great Salt Lake from the Utah Climate Center (UCC), managed by Utah State University (USU, 2024). Hourly dewpoint temperature, T_d (°C), wind velocity, v_w (m/s), and site pressure, p_{site} (hPa), since 2017 was gathered along with daily maximum and minimum air temperature, $T_{a,max}$ and $T_{a,min}$ (°C) (Figure 7; Table C2). The USGS also measured 15-minute v_w at the New Breach, which was compiled from the USGS NWIS database.

2.3.2 Data Curation

Evaluation of Great Salt Lake Salinity

As noted, the various available datasets (Table 1) used different field methods to collect water quality data for use in estimating C, necessitating appropriate conversion methods for hypersaline environments. In this study, all north section and south section water quality data from each entity was converted to C in g/L and compiled into the salinity dataset. Data pertaining to the south section was apportioned to either the UBL or the DBL

using a depth to DBL dataset developed by the USGS which utilized profile measurements from only two sites, Carrington Bay and Gilbert Bay (C. Rumsey, personal communication, April 11, 2024). Direct ρ measurements were prioritized in this analysis due to accuracy and since ρ was the most common measurement across agencies (Salinity Advisory Committee, 2020).

To convert ρ to C, an equation of state (EOS, see Eq. 1) derived specifically for the Great Salt Lake for C ranging from 0 to 180 g/L and for T ranging from 4 to 50 °C was applied (Naftz, 2011):

$$\rho - \rho^0 = 184.01062 + 1.04708C - 1.21061T + 3.14721 - 4C^2 + 0.00199T^2 \\ -0.00112ST \tag{1}$$

where ρ = measured density of Great Salt Lake water [$\mathrm{g/cm^3}$], ρ^0 = density of pure water at the sample temperature [$\mathrm{g/cm^3}$], T is in [°K], and C = sample salinity [g/L]. Density of pure water at the sample temperature was calculated using Eq. 2 (Spieweck and Bettin, 1992):

$$\rho^0 = [999.83952 + 16.952577(T - 273.15) - 7.9905127 - 3(T - 273.15)^2 \\ - 4.6241757 - 5(T - 273.15)^3 + 1.0584601 - 7(T - 273.15)^4 \\ - 2.8103006 - 10(T - 273.15)^5\ ]/[1 + 0.016887236(T - 273.15)] \tag{2}$$

These existing curve-fit polynomials are regularly used by Utah DNR; and were extended by the USGS for salinity values up to 275 g/L and current lake conditions (C. Rumsey, personal communication, May 24, 2023).

Note that ρ varies with T yet each entity measures ρ at different temperatures. Thus, all ρ measurements needed to be converted to a reference temperature of 20 °C, which has been used by the USGS since 2017. The USGS provided a linear regression equation for Great Salt Lake waters (C. Rumsey, personal communication, June 8, 2023):

$$\rho_{20} = \rho + 0.0004417(T - 20) \tag{3}$$

where ρ_{20} i=estimated sample density at 20 °C [g/cm^3] and T is in [°C]. For this study, all ρ samples not measured at 20 °C, including data from HDR and UGS, were converted to ρ_{20} using Eq. 3 before being used in Eq. 1 and Eq. 2.

The American Water Works Association (AWWA) developed Eq. (4 to convert SC to C (Schemel, 2001):

$$C = K_1 + K_2R^{0.5} + K_3R + K_4R^{1.5} + K_5R^2 + K_6R^{2.5} \tag{4}$$

where C=salinity in practical salinity units (psu), K_1 = 0.0120, K_2 = -0.2174, K_3 = 25.3283, K_4 = 13.7714, K_5 = -6.4788, K_6 = 2.5842, and R is calculated to be:

$$R = \frac{SC_{sample}}{SC_{seawater}} \tag{5}$$

with SC_{sample} = SC of the water sample at 25 °C in [µS/cm] and $SC_{seawater}$ = SC of standard seawater at 25 °C (53,087 µS/cm). However, this equation is only valid for C ranging from 2 to 50 g/L whereas recorded values of Great Salt Lake brine during the period of analysis were as high as 300 g/L. An equation to convert SC of hypersaline brine to S was not available. Therefore, a new conversion equation (Eq. (6) was developed in

this study at the Environmental Quality Laboratory (EQL) in the UWRL at USU for 20 g/L $\leq C \leq$ 290 g/L:

$$SC = (-3.85 \times 10^6)\rho_{20}^2 + (9.48 \times 10^6)\rho_{20} - 5.61 \times 10^6 \quad (6)$$

where SC is in [µS/cm].

Eq. (6 was developed using a prepared solution of brine with a concentration of 300 g/L and the same ion composition as Great Salt Lake. Correct ion composition for the brine solution was calculated by averaging all percent by weight measurements for each major ion in GSL brine based on data from the UGS Brine Chemistry Database from March 2017 to September 2020 (Utah Geological Survey, 2020; Appendix A. USU UWRL EQL Experiment Data. Ion composition for the north section differs from the south thus the average of both compositions was used and assumed to be representative of the whole lake.

After preparing the solution, density was directly measured by removing a subsample with volume, ~~V~~, and measuring total mass of the subsample, M. Using these measurements, sample ρ was calculated via $\rho = M/$~~V~~. As with in-situ field measurements, the solution was also measured for SC [µS/cm] and T [°C] with the In-Site Aqua Troll 600 series water quality sonde. $\%C$ of the sample was measured using an Atago MASTER-S28a refractometer. These measurements were repeated on solutions ranging from 20-290 g/L that were prepared by diluting and thoroughly mixing the stock solution for 24 hours using a stirring plate. Five repeat measurements of ρ, SC and $\%C$ were performed on 10 samples chosen randomly to ensure consistency in the measurement methods (Figure A1).

A simple regression equation (Eq. (6) obtained from the USU UWRL EQL SC vs. ρ data produced a conversion relationship applicable for the full range of C observed at the Great Salt Lake. The performance of Eq. (1, Eq. (4 and Eq. (6 to calculate C via the USU UWRL EQL dataset (Table A; Table A) were plotted as a function of ρ and considered via calculated Mean Absolute Percent Error (MAPE) values (see chapter 2.4.1 for results). The EQL experiment data was also used to evaluate the conversion between $\%C$ to C [g/L] using Eq. (7 (Chapra, 1997):

$$C = \%C \times \frac{1}{100} \times \rho \tag{7}$$

where ρ is in [kg/m3]. For this conversion when compared to the ρ method, it was found to overestimate C. Therefore, a correction factor was developed by plotting the $\%C$ method against the ρ method for each sample. The computed slope of the linear regression line was used as a correction factor, CF, by C/CF. This correction was applied to all the DWiR observations within the compiled salinity dataset. While USU UWRL EQL sample T recordings were within a small range, 20 to 23 °C, all ρ measurements were standardized to 20 °C using Eq. (3 to minimize any potential variability in ρ due to any T differences between samples.

New Breach Salt Flux

To calculate NS and SN New Breach salt flux (M, metric tons/d) for use in the principal component and correlation analysis, C from both USGS and HDR New Breach samples (January 2017 to August 2020) and the USU 15-minute continuous C record (August 2020 to December 2022) were used. The analysis also included the USU New

Breach Q dataset (January 2017 to December 2022). Any gaps in the C record at the New Breach were linearly interpolated to pair with the 15-minute continuous Q dataset. New Breach M was calculated separately for NS and SN flow through the New Breach using (Chapra, 1997):

$$M = QC \tag{8}$$

where M is in [metric tons/d], Q is in [m^3/d], and C is in [metric tons/m^3].

Evaporation

A daily, arithmetic average was applied to the hourly climate data at each site including: v_w, p_{site}, T_d, $T_{a,max}$ and $T_{a,min}$ (Figure C2). These daily values were spatially averaged across sites to produce a single, daily time series for each variable, representative of Great Salt Lake conditions. The representative climatic data and a modified version of the Penman equation (see Eq. (9) was used to calculate depth of evaporation (E_d) off the Great Salt Lake at each salinity sampling location (Mohammed et al., 2012):

$$E_d = \frac{\Delta'}{\gamma + \Delta'} \cdot \frac{R_n}{\lambda_v \rho_w} + \frac{\gamma}{\gamma + \Delta'} \cdot K_E v_a (e_s(T_a)\beta(T_a, C) - e_a(T_d)) \tag{9}$$

where E_d is in [m/d], Δ' = saturated vapor pressure gradient for a saline surface [kPa/°C], γ = psychrometric constant [kPa/°C], R_n = net energy available at the water surface [MJ/m^2·d], λ_v =the latent heat of evaporation [MJ/kg], ρ_w =density of water [kg/m^3], K_E = bulk latent heat transfer coefficient approximated to be 1.28x10^{-3} [mm·s/m·kPa·d (Mohammed, 2006), v_a =wind velocity at the water surface [m/d], e_s = saturated vapor pressure of a freshwater surface at air temperature, e_a = actual air vapor pressure at

dewpoint temperature [kPa], β =water activity coefficient, T_a = mean daily air temperature [°C], T_d = mean daily dewpoint temperature [°C], and C = salinity of the Great Salt Lake water [g/L].

Evaporative depth is proportional to the difference between the e_s at the water surface and the e_s of the air, functions of air temperature at the water surface and air temperature, T_s and T_a respectively. Salinity controls the water e_s which is lower for saline water than for freshwater at the same temperature (Mohammed and Tarboton, 2012). The reduction is dependent on the β which is the ratio of vapor pressure over salt water to the vapor pressure over freshwater at the same temperature. e_s of a saline water surface in terms of the water activity coefficient is given by (Mohammed, 2006):

$$e'_{sat}(T_s, C) = e_s(T_s)\beta(T_s, C) \tag{10}$$

where e'_s =saturation vapor pressure of the saline water surface [kPa], a function of surface temperature, T_s, and surface water salinity, C, and e_s = saturation vapor pressure of a freshwater surface [kPa].

T_s is difficult to measure and not available for the salt lake, therefore Δ' was calculated using the traditional approach for deriving the Penman equation which is based on the assumption that T_s and vapor pressure can be approximated using T_a, humidity, and the gradient of the saturation vapor pressure-temperature curve (Mohamad, 2006). This is accomplished using a Taylor series approximation where:

$$e_s'(T_s, C) \cong e_s'(T_a, C) + \Delta'(T_s - T_a) \tag{11}$$

$$\Delta' = \left.\frac{e_s'}{dT}\right|_{T_a,C} \tag{12}$$

$$\Delta' = \frac{\partial e_s}{\partial T_s}\beta + e_s \left.\frac{\partial \beta}{dT_s}\right|_{T_a} \tag{13}$$

with T_a = mean daily air temperature [°C]. e_s and e_a are described by the general equation for vapor pressure (Chapra, 1977):

$$e = 4.596 e^{\frac{17.27T}{237.3+T}} \tag{14}$$

where T is in [°C]. To calculate e_a, Eq. 14 was evaluated at the air dewpoint temperature, T_d. To calculate e_s, Eq. 14 was evaluated at the daily average air temperature, T_a, calculated as (Allen et al., 1998):

$$T_a = \frac{T_{a,max} + T_{a,min}}{2} \tag{15}$$

with $T_{a,max}$ = maximum daily air temperature [°C] and $T_{a,min}$ = minimum daily air temperature [°C]. Using Eq. 14 and derivation rules, Eq. 13 simplifies to Eq. 16:

$$\Delta' = \beta \left[\frac{4098.17}{(237.3 + T_a)^2}\right]\left[4.596e^{\frac{17.27\ a}{237.3+T_a}}\right]$$

(16)

β is calculated by summing the weighted reduction in e_s due to each of the constituent salt ions. Estimation of β is accomplished by solving the Pitzer equations, which was done by Mohammed (2006) for a range of T_a and C values at the GSL (Pitzer, 1973; Table B1). This table was employed to calculate the activity coefficient at each sampling location for each day during the period of analysis by linearly interpolating between C and T_a values within the table to obtain a β value for the given T_a and C.

The psychrometric constant was calculated using:

$$\gamma = \frac{c_a p_{site}}{0.622\lambda_v}$$

(16)

where c_a = heat capacity of air equal to 1x10^{-3} [MJ kg^{-1} °C^{-1}], p_{site} = atmospheric pressure [kPa], and λ_v = latent heat of vaporization [MJ kg^{-1}] calculated using (Mohammed, 2006):

$$\lambda_v = 2.5 - 2.36 \times 10^{-3} T_a$$

(17)

Net energy available at the water surface was calculated using (Allen et al., 1998):

$$R_n = R_{ns} - R_{nl}$$

(18)

where R_{ns} = net solar short-wave radiation [MJ m^{-2} day^{-1}] and R_{nl} = net outgoing long wave radiation [MJ m^{-2} day^{-1}]. Net solar short-wave radiation was calculated using (Allen et al., 1998):

$$R_{ns} = (1 - \alpha)R_s \tag{19}$$

where α = short wave radiation reflection coefficient suggested to be 0.08 for open water (Shuttleworth, 1993) and R_s = incoming shortwave solar radiation [MJ m^{-2} day^{-1}]. Net outgoing longwave radiation [MJ m^{-2} day^{-1}] was calculated using (Allen et al., 1998):

$$R_{nl} = \sigma \left(\frac{T_{max,K}^4 + T_{min,K}^4}{2} \right) \left(0.34 - 0.14\sqrt{e_a}\right) \left(1.35 \frac{R_s}{R_{so}}\right) \tag{20}$$

where σ = the Stefan Boltzman constant taken as 4.903x10^{-9} [MJ K^{-4} m^{-2} day^{-1}], $T_{max,K}$ = maximum daily air temperature [°K], and $T_{min,K}$ = minimum daily air temperature[°K], R_{so} = clear sky solar radiation [MJ m^{-2} day^{-1}], and e_a = actual vapor pressure of the air [kPa], a function of dewpoint temperature, T_d [°C], and calculated using Eq. 14.

Clear sky solar radiation was calculated using (Allen et al., 1998):

$$R_{so} = (a_s + b_s)R_a \tag{21}$$

where a_s = 0.25 and b_s = 0.5 as suggested in Shuttleworth (1983), and R_a = extraterrestrial radiation [MJ m^{-2} day^{-1}] calculated as:

$$R_a = \frac{24(60)}{\pi} G_{sc} d_r [\omega_s \sin\varphi \sin\delta + \cos\varphi \cos\delta \sin\omega_s] \tag{22}$$

with G_{sc} = solar constant, equal to 0.0820 [MJ m^{-2} day^{-1}], d_r = inverse relative distance Earth-Sun, ω_s = sunset hour angle [rad], δ = solar declination [rad], and φ = latitude [rad]. Inverse relative distance Earth-Sun was calculated using (Allen et al., 1998):

$$d_r = 1 + 0.033 \cos\left(\frac{2\pi}{365} J\right) \tag{23}$$

where J = number of the day in the year. Solar declination was calculated using (Allen et al., 1998):

$$\delta = 0.409 \sin(\frac{2\pi}{365} J) \tag{24}$$

and the sunset hour angle was calculated by (Allen et al., 1998):

$$\omega_s = \cos^{-1}[-\tan\varphi \tan\delta] \tag{25}$$

2.3.3 Great Salt Lake Principal Component Analysis

The New Breach was constructed to aid management of south section UBL *S*, yet the spatial and temporal influence of New Breach M compared to other influential variables is not well understood. Therefore principal component analysis, PCA (Helsel et al., 2020), was performed to explore the spatial and temporal patterns of fluctuating UBL *S* since opening of the New Breach so that general lake conditions can be characterized for use in salinity modeling efforts. The PCA was preformed using the SciKitLearn package in Python (VanderPlas, 2016). Discrete south section open water C observations from the UBL were paired with daily averages of: E_d, New Breach M, and Q from lake inflows. Due to limited temporal data, only open water sites where there were at least three water samples per year over three consecutive years during the period of analysis were included to ensure seasonality was retained in the dataset. For sites where a water quality profile was reported,

C profiles above the DBL interface (determined by the USGS depth to DBL dataset) were averaged to represent the UBL as a daily average at the time of sampling. M_{NS}, M_{SN} and FB, BR, WR, and GD Q were included as separate variables in the PCA. Groundwater q (unmeasured) and precipitation P (arid, local annual average of 472 mm) contributions to the lake were not included based upon unmeasured q to the lake and the hydrologic analysis of the GSL by Mohammed and Tarboton (2012), which found these parameters to be negligible.

In this study, data seasonality and exploratory, PCA results merited a three-season PCA application: spring during snowmelt and high runoff (RO) between March and June, summer and fall where conditions are typically hot with low river inflows (HLF) between July and October, and winter when temperatures are lowest accompanied by low river inflow (CLF) between November and February. Since a PCA is sensitive to outliers and the differing variable magnitudes, histograms and descriptive statistics were compiled for the datasets used in the PCA. Any variable that demonstrated a skewed distribution was log-transformed and all variables were standardized before performing the analysis.

2.3.4 Representative South Section Salinity

When examining the Great Salt Lake south section UBL C dataset, a small subset of measurement sites exhibited daily deviations likely due to topographic effects and any routine mineral extraction activities. Therefore, results from the PCA were used to assist with data filtering; seasonal outliers were removed revealing a clear central trend in C within the dataset. A daily, south section UBL C time series was then calculated by 1) preparing daily time series of C at each sampling location, with supplemental temporal data

estimated through linear interpolation, then 2) determining the daily median value across sampling locations. Since the filtered dataset revealed a strong central trend, this daily time series is presumed to be representative of general south section, UBL conditions.

Measurement uncertainty compounded by multiple independent data sets, C conversion, and a daily, spatial average of C with linear interpolation to fill missing temporal data were of great concern when developing the south section C time series. Therefore, to gain greater insight into these uncertainties and given the simplification of spatial homogeneity, the filtered UBL C data was segregated into measurements derived from ρ, SC and $\%C$. The daily standard deviation, σ, for each parameter and set of sites was calculated and the average used as a metric regarding spatial uniformity for the Great Salt Lake. Two additional subsets were taken from the C data, one including observations from sites B and L and another with observations from sites E and K. These additional subsets encompass sampling locations from BSC, DWiR and USGS that were closest in proximity to each other and were used to quantify uncertainty in combining C data from multiple datasets. Measurement uncertainties due to instrumentation accuracy as reported by manufacturer documentation were also referenced. Additional quantification of measurement uncertainties by various entities and their field programs was not considered herein.

These sources of uncertainty were assumed to be uncorrelated. Total standard deviation (σ_T) for the representative C time series was calculated using a first order error analysis approach (Brown and Hambley, 2002):

$$\sigma_T = \sqrt{\sum_{i=1}^{n} \sigma_1^2 + \sigma_2^2 + \sigma_3^2 + \cdots + \sigma_n^2}$$

(26)

where σ_T [g/L] = total standard deviation in median C given all error sources, n = total number of error sources, and σ_1^2 , σ_2^2, σ_3^2, σ_n^2 = average variance associated with each error source during the period of analysis [g^2/L^2]. A 90% confidence interval for the median UBL C time series was then calculated assuming a normal C distribution:

$$CI_{90\%} = \overline{C} \pm 1.65\sigma_T$$

(27)

where $CI_{90\%}$ = 90% confidence interval and $\overline{C}$ =median UBL section salinity [g/L] on any given day during the period of analysis.

2.3.5 Seasonal Salinity Drivers

The seasonal influence of each forcing variable on the representative south section C time series was investigated by performing a regression analysis using the non-parametric Theil-Sen method, which is resistant to outliers and represents the median regression line. The regression was performed on the log transformed data used in the PCA, subset for water year 2020 and further segregated into RO, HLF, and CLF seasons. The entire time series was not selected since an initial analysis showed the magnitude of salinity values within each season fluctuated across years and formed data clusters within the analysis period. To clarify the results, data from a single water year 2020 was selected as it exhibited average hydroclimatic conditions compared to the entire period of analysis.

The 95% confidence intervals surrounding the calculated Theil-Sen slopes were determined and used to evaluate the significance of the linear relationships between log transformed C and E_d, M_{SN}, M_{NS}, and river Qs across seasons.

2.4 Results

2.4.1 Data Curation and Characterization

The results from (Eq. (6) showed that the equation is valid for ρ up to 1.25 g/cm^3 (Figure 8a). The water sample prepared at the USU UWRL EQL and the Great Salt Lake USGS samples taken at the New Breach were in close agreement and followed the same nonlinear trend. The USGS data exhibited significant measurement uncertainties ($\%\varepsilon$) for $\rho \geq 1.2$. This can be attributed to potential field uncertainties because the USU laboratory experiment required significant mechanical mixing to achieve sample uniformity at these salt concentrations. Mean absolute percent errors (MAPE) of the AWWA conversion (Eq. (4) when compared to Naftz EOS (Eq. (1) was 10.1% while MAPE of (Eq. (6) was 3.3%. The performance difference is due to the original range of C used to formulate the AWWA method (Schemel, 2001), as good agreement exists for $\rho < 1.10$ g/cm^3. Performance of (Eq. (6) favors implementation for converting open water ρ to SC for the Great Salt Lake and for saline lakes of similar ion composition. It further supports the expanded usage of the AWWA conversion method above the 50 g/L limit documented in Schemel (2001). However, prediction uncertainties via Eq. (4 increased for $\rho \geq 1.1$ g/cm^3.

Figure 8

USU UWRL EQL Experiment Results

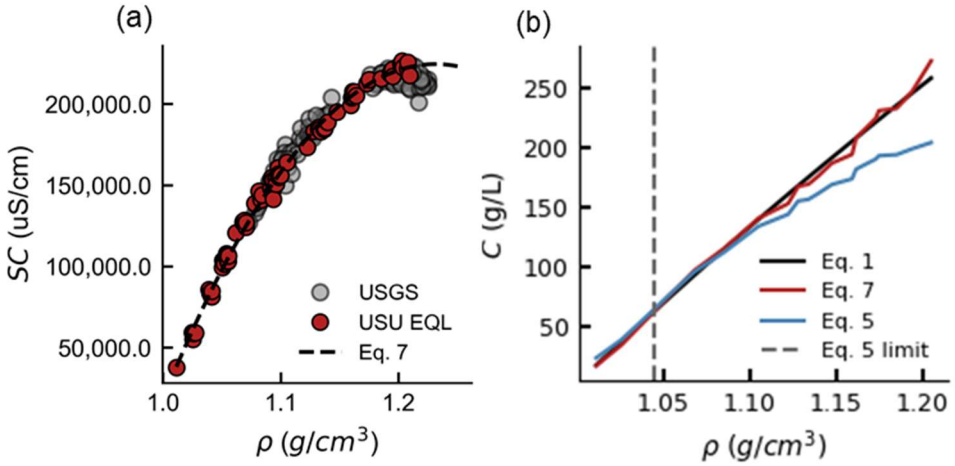

Note. Experiment results included in the figure are (a) ρ versus SC including USGS data pairs collected from the New Breach and (b) comparison of the C conversion methods.

The correction constant $CF = 1.24$, based upon the relationship between C measured in the laboratory and C predicted via Eq. (7, indicated that $\%C$ measurements at the Great Salt Lake tended to overpredict C when compared to ρ measurements (Figure 9). The DWiR dataset, based upon a refractometer, was adjusted accordingly herein.

Figure 9

USU UWRL EQL Experiment Data Pairs

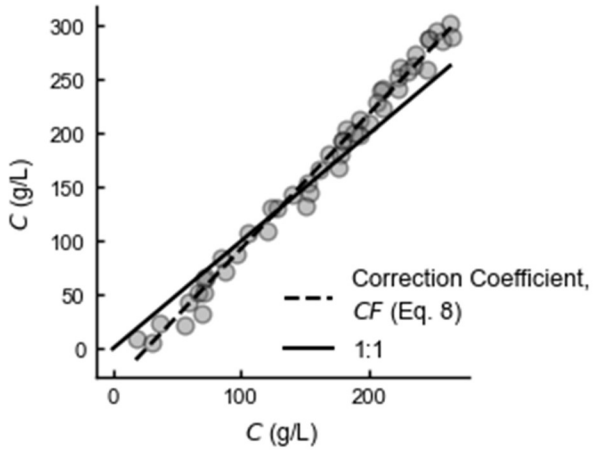

Note. Salinity in g/L derived from ρ is plotted along the x-axis versus C derived from $\%C$ on the y-axis.

The histograms and descriptive statistics prepared for exploratory analysis preceding the PCA provided insight into the magnitude and frequency of key variables observed at the GSL (Figure 10;

Table 2). During the study period, all datasets, except for inflows from FB, exhibited positively skewed distributions that confirmed applying a log transformation to the data as part of the PCA data processing (Figure 10). Daily E_d showed a high frequency of lower values due to the semi-arid climate with winters generally lasting from November to April. During the period of analysis, total M_{SN} was 2.30×10^{12} metric tons while total M_{NS} was 1.67×10^{12} metric tons indicating that more salt left the south section via Q_{SN} flow through the New Breach than entered via Q_{NS} through the New Breach. The BR, being the largest source of river inflow to the GSL, exhibited the highest range and median of Q.

Deviating from the other inflows, Farmington Bay had a normal distribution, periodically recording negative Q values due to the location of the measurement gage at a bridge along the Antelope Island causeway that segregates Gilbert Bay from Farmington Bay (Figure 7). Specifically, when inflow from the Jordan River into FB is low and southerly wind is high, south section water from Gilbert Bay flows back into FB causing a short-term flow reversal event (Naftz et al., 2014).

Figure 10

Histograms of Great Salt Lake Water Quality and Quantity Data Used in the Principal Component Analysis from January 2017 to December 2022

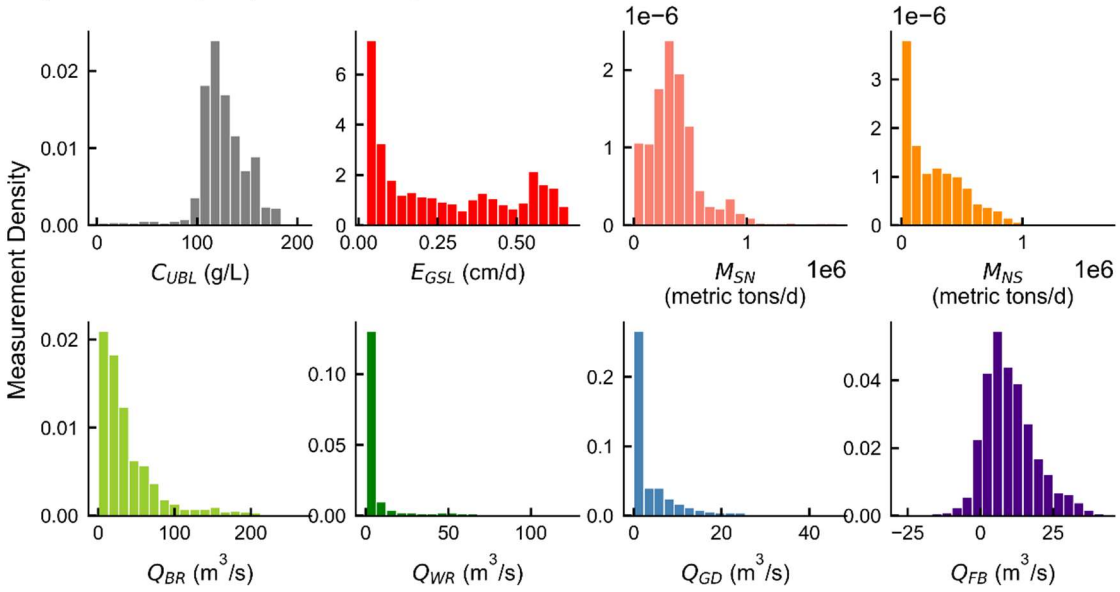

Table 2

Descriptive Statistics for the Data Prepared for the Principal Component Analysis

*Variable	Range	Median	Units
C	[90, 204]	124	g/L
E_d	[0.025, 0.66]	0.2	cm/d
M_{SN}	$[0, 1.8 \times 10^6]$	3.3×10^5	metric tons/d
M_{NS}	$[0, 1.6 \times 10^6]$	2.1×10^5	metric tons/d

Q_{BR}	[0.67, 266]	26.2	m^3/d
Q_{WR}	[0.3, 122]	2.74	
Q_{GD}	[0.03 , 46]	0.62	
Q_{FB}	[-27, 42.4]	8.79	

Note. Statistics reflect values from January 2017 to December 2022.

2.4.2 Spatial and Temporal Filters for GSL Salinity Data

Results from the PCA (Figure 11) revealed spatial patterns of the south section, UBL C across seasons in response to its primary drivers. This insight aided in filtering observations from sampling sites included in the comprehensive GSL C dataset (Figure 11). Regarding seasonality, Principal Component 1 (PC1), Principal Component 2 (PC2), and Principal Component 3 (PC3) explained 72.7% of dataset variation during runoff (RO), 73.3% of variation during hot low-flow (HLF) months, and 62.7% of variation during cold low-flow (CLF) months (Table 3). During RO, HLF, and CLF, the majority of UBL C observations responded similarly to PC1, PC2 and PC3. Data points from DWiR/USGS sites A, C, M, and N consistently deviate from the main cluster (Figure 11). The magnitude of C from these sites is consistently lower than the other observations and occurred when river Qs were higher as indicated by the 2D projections of C and Q in PC space. Additional outliers were observed during HLF and CLF that had higher C compared to the main cluster (Figure 11d, Figure 11f), but these observations did not occur consistently at the same sites nor across seasons. While they may not be representative of south section conditions, the lack of consistency in sampling location and season did not support exclusion from the representative dataset.

Figure 11

Principal Component Analysis Results

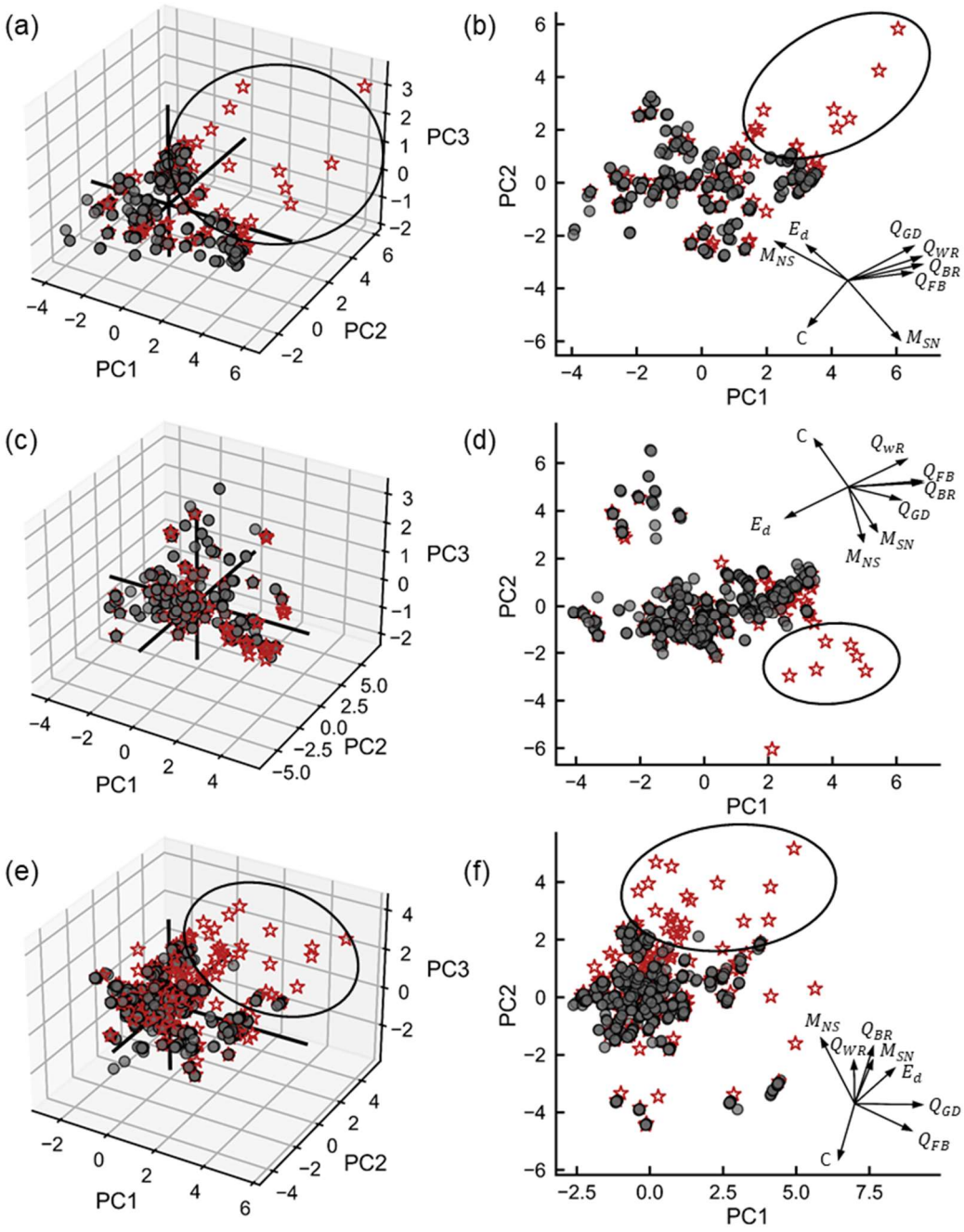

*Note. P*rincipal components for discrete measurements of south section UBL C are paired with daily values of E_d, M_{SN}, M_{NS}, Q_{BR}, Q_{WR}, Q_{FB}, and Q_{GD} during (a,b) spring runoff

between March and June, (c, d) hot low flow between July and October and (e, f) cold low flow between November and February. Gray circular symbols represent data from sites that were found to be representative of south section conditions, and red star symbols represent data from sites that were left out of the representative south section C dataset. Normalized, 2D projections of each variable in PC space are included in (b, d, f) and are offset from the origin for clarity.

Table 3

Principal Component Values for Runoff, Hot Low-Flow and Cold Low-Flow Seasons

Months	Season	Principal Component	Explained Variance	Total (%)
3 - 6	Runoff (RO)	PC1	0.405	72.7
		PC2	0.199	
		PC3	0.123	
7 - 10	Hot Low-Flow (HLF)	PC1	0.38	73.3
		PC2	0.249	
		PC3	0.104	
11 - 2	Cold Low-Flow (CLF)	PC1	0.245	62.7
		PC2	0.222	
		PC3	0.16	

The compiled C time series (Figure 12), including all available observations of UBL C, verified the patterns revealed in the PCA and showcased the general trend in UBL C that included the New Breach for the period of analysis. DWiR/USGS sites A, C, M, and N reported significantly lower C values during the RO and CLF months. In addition, occasional outliers were observed from seven other sites O, P, Q, R, V, X). These observations were sporadic and did not occur consistently; however, the outlier

observations from sites R and Y could be attributed to a rare flow event in the DBL [characterized by Naftz (2014)] caused by unidirectional Q_{NS} through the causeway that happened infrequently at the New Breach. Specifically, this lake current is located at the bottom of the lake where Carrington Bay connects to Gilbert Bay (Figure 3). While this could explain the outliers at these two sites, there is not enough sample data to verify this hypothesis and attribute them to the DBL spillway. Based on results from the PCA and the compiled C time series which identified representative south section sampling locations, data from sites A, C, M, and N were removed from the comprehensive GSL dataset during RO and CLF months. Observations from all other sites were supplemented using linear interpolation to develop daily time series at each sampling location. Daily UBL C was then calculated by finding the spatial median across all sites in the filtered dataset and is assumed to be representative of lake conditions when considering the south section in its entirety (Figure 12).

Figure 12

Compiled Open Water C Time Series for the South Section UBL of the Great Salt Lake

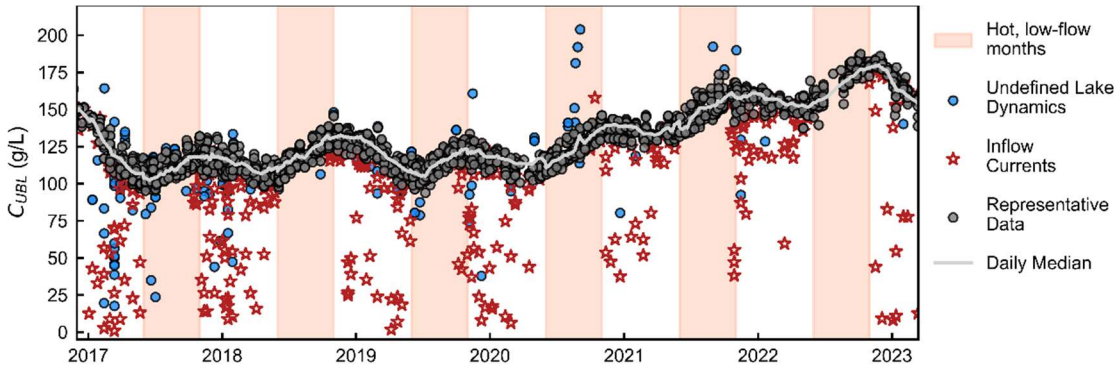

The outliers observed from the PCA and compiled time series are assumed to be due to strong freshwater currents from the BR through BR Bay and the Jordan River through FB which have been observed during field sampling events (C. Rumsey, personal communication, 28 September 2022). Across all three seasons, C at site M ranged from 7-169 g/L, site A ranged from 1-173 g/L, while representative C ranged from 102 - 198 g/L (Figure 13a). When comparing the distribution of the south section UBL representative C to the outlier sites near BR inflow, the spread of the outlier distributions is much larger with the tails extending down to values close to the inflows themselves during RO and CLF seasons. During HLF months, the median and spread of the BR outlier site distributions are almost identical to the representative C distribution. Farmington Bay exhibits a similar trend. The spread of the outlier site distributions is wider compared to the representative C distribution during RO and CLF, but identical to the representative C distribution during HLF (Figure 13b).

Figure 13

Box Plots of C Observations from Outlier Sites Found During the Principal Component Analysis

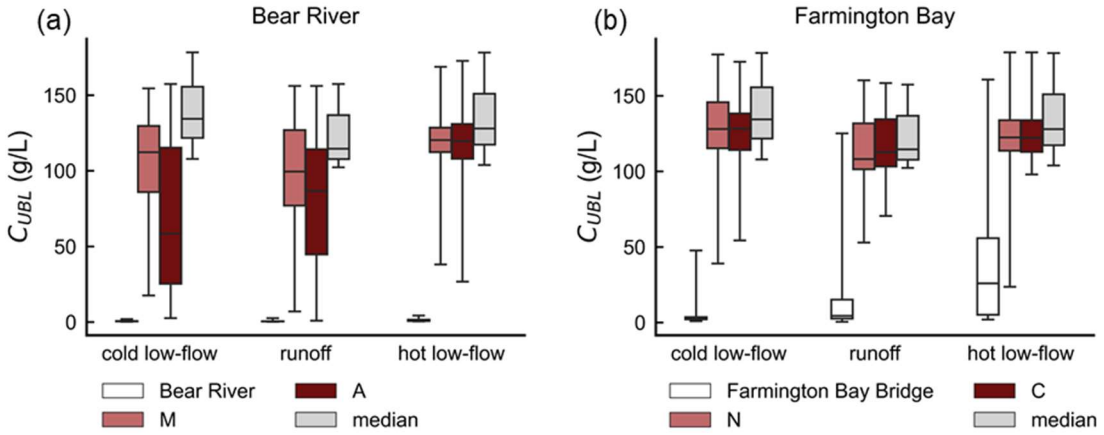

Note. Data utilized in the plots are from January 2017 to December 2022 for (a) the Bear River gage, sites A and M, representative south section UBL salinity (labeled median) and (b) the Farmington Bay Bridge gage, sites C and N, and representative south section UBL salinity.

Another key insight into lake dynamics is recent C values for sites A and M juxtaposed with sites C and N. Farmington Bay inflows have higher C compared to the BR inflows across all three seasons due to mass loading within Farmington Bay. Currents through FB Bay are also lower than BR Bay Bridge during RO and CLF moths as indicated by the wider range of C recorded at the BR outlier sites. Based on these observations, it can be presumed that FB inflows mix quicker into the south section and that the spatial extent of BR Bay inflows is wider than FB inflows. During HLF months, however, the results indicate that these lake currents do not reach the outlier sites as median salinity recorded at these sites are identical to the median south section salinity. Insights garnered

from the analysis of outlier sites within the comprehensive C dataset highlight seasonal and spatial filters that should be applied to ensure observations are representative of average south section conditions. Further, these results aid future work by providing and documenting the highest spatial and temporal resolution C dataset available at the GSL.

2.4.3 Representative South Section Salinity

After developing the representative UBL C series (Figure 12), the error analysis quantified a range of uncertainty associated with combining the individual datasets and assuming spatial homogeneity across the filtered sampling locations (Figure 14; Figure 15; Table 4). Averaging through space and combining independent datasets contributed the most uncertainty (σ = 3.97 g/L, 6.64 g/L,Figure 15). Generally, σ values were consistent but spikes in σ occurred mainly during CLF months where observations of undefined lake dynamics were left in the dataset, as noted above (Figure 14a; Figure 15c). Combining the average σ values, the median UBL C time series is presumed to be representative of UBL conditions $\pm$12 g/L (Table 4). This metric informs use of the representative C time series for lake management decisions. This series is also useful for analyzing entire south section salinity response to management actions but may present a challenge in determining site specific C given the range of uncertainty. This series further shows the importance of adopting standard operating procedures for future C monitoring.

Figure 14

Daily σ of UBL C for the %C, SC, and ρ Datasets

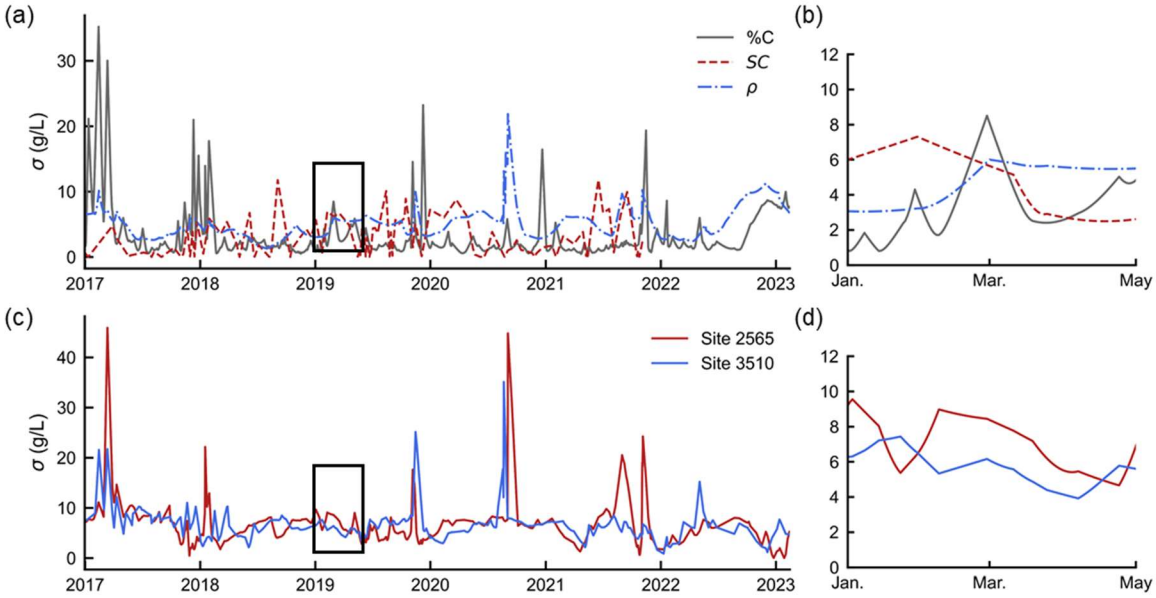

Note. Data utilized in the plots is from (a) January 2017 to December 2022 and (b) January 2019 to May 2019 and for data compiled from site 2565 and site 3510 from (c) January 2017 to December 2022 and (d) January 2019 to May 2019. The 2019 data window is included to show the general magnitude of σ across the subsets.

Table 4

Average Standard Deviation (σ), Total Standard Deviation (σ_T), and Associated 90% Confidence Interval for UBL Salinity (C)

Entity	Dataset	σ (g/L)	σ_T (g/L)	90% CI
BSC	YSI 556 Conductivity Meter	1.02	7.81	12.88
HDR, UGS, USGS	Anton Paar DMA 35 Density Meter			
DwiR	Atago Master S28α Refractometer			
BSC	Specific Conductance	3.97		

HDR, UGS, USGS DWiR	Density Percent Salinity	
BSC, UGS, USGS	GSL site 3510 GSL site 2565	6.64

Note. σ is the average standard deviation from each type of error in the representative UBL C dataset while σ_T is the propagated error within the UBL C dataset, calculated from each σ.

Figure 15

Representative UBL C Time Series and Calculated 90% Confidence Interval

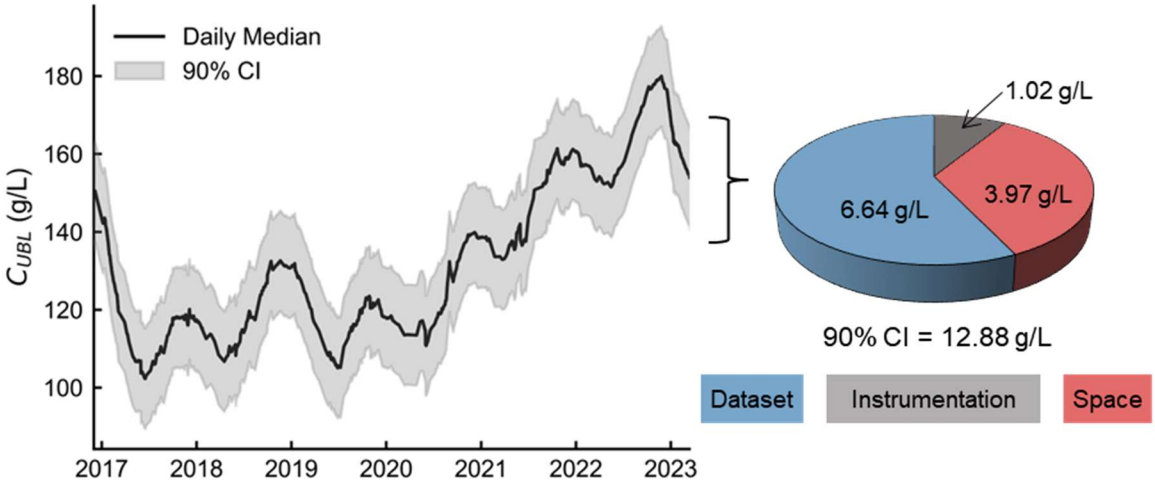

Note. Date utilized in the plots is from January 2017 to September 2023. The pie chart represents the standard deviation (σ) introduced into the C dataset from the three sources of error which was used to calculate the total standard deviation (σ_T) and confidence interval.

2.4.4 Seasonal Salinity Drivers

Seasonal correlation between C_{ubl} and E_{GSL}, New Breach M, and river Qs revealed the major drivers of changes in C within the GSL (Table 5;Figure 16). If the Theil-Sen

slope 95% confidence intervals (p value of 0.05) did not include zero, the correlation was determined to be significant. There was a significant, negative correlation with Q_{BR}, Q_{WR}, and Q_{GD} during RO and CLF showcasing the role river inflows play in dilution of the south section. M_{NS} contributes mass to the south section DBL which is then transferred to the UBL via turbulent diffusion across the layer interface, yet it only exhibited a positive correlation during CLF. The negative correlation during HLF is explained because M_{NS} is driven by the ρ differential between the two sections of the lake. As south section C increases during HLF, M_{NS} decreases. In contrast, the main source of south section mass export comes from M_{SN} yet it showed significant, positive correlations during HLF and CLF and no correlation during RO. These potentially counterintuitive results indicate that the short-term effects of mass exchange through the New Breach are outweighed by other salinity drivers. However, influencing mass exchange through the New Breach is still relevant to management efforts.

Table 5

Theil-Sen Slopes and Corresponding 95% Confidence Intervals Between C and Each Variable Included Within the PCA

Variable	RO		HLF		CLF	
	Slope	95% CI	Slope	95% CI	Slope	95% CI
E_d	3.02	[-3.28, 10.68]	**-4.17**	[-5.83, -2.80]	**-14.12**	[-20.51, -8.98]
M_{NS}	5.13	[-3.59, 13.03]	**-2.23**	[-3.64, -0.86]	**12.48**	[9.84, 14.8]
M_{SN}	-7.68	[-18.54, 1.69]	**4.22**	[2.88, 5.50]	**5.12**	[3.50, 6.77]
Q_{BR}	**-13.44**	[-20.40, -5.68]	1.11	[-4.35, 4.71]	**-6.67**	[-8.57, -4.55]
Q_{WR}	**-27.99**	[-44.71, -6.71]	**6.69**	[4.25, 8.95]	**-20.94**	[-24.47, -17.71]
Q_{GD}	-2.72	[-13.96, 10.42]	**-3.21**	[-5.21, -1.13]	**-22.22**	[-51.64, -6.75]
Q_{FB}	2.41	[-6.71, 11.38]	**4.93**	[1.31, 8.23]	**-9.94**	[-13.33, -6.60]

Note. Slopes that are bolded indicate a significant (p value < 0.05) linear relationship between log-transformed data.

Figure 16

Correlation Analysis Results

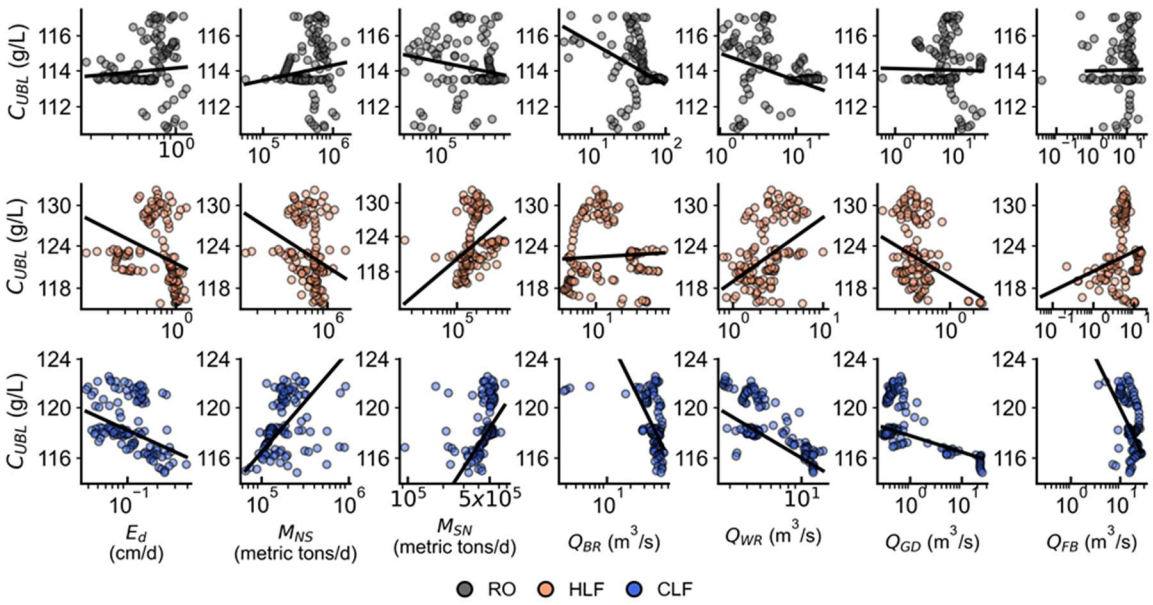

Note. Representative south section C is plotted against evaporation, New Breach salt fluxes, and river inflows from October 2019 through September 2020 separated and colored by season. Solid black lines indicate Theil Sen regression lines. RO refers to spring runoff months between March and June, HLF refers to hot, low river inflow months between July and October, and CLF refers to cold, low river inflow months between November and February.

This study presumed that E_d would be positively correlated with UBL C across all seasons since it is the only freshwater outflow. However, E_d exhibited significant, negative correlation during HLF and CLF. During HLF, water surface elevation decreased while C

within the south section increased because E_d outweighed river inflow exhibited by the highest E_d values occurring when inflow was lowest (Figure 17a; Figure 17b). However, the highest values of E_d occurred at the beginning of the period when temperatures were hottest therefore the largest values of E_d were paired with the lowest values of C explaining the negative correlation. During CLF, E_d values were clustered between 0 – 0.3 cm/d and outweighed by inflow volumes that rarely dropped below 30 m^3/d which caused lake level to rise (Figure 17a). Inflow volume outweighed E_d at the beginning of RO, but the balance was shifted toward E_d as soon as temperatures started to rise in May represented by the declining lake level between May and September. These results showed that Great Salt Lake level is primarily driven by river Q during CLF and the first half of RO and driven by E_d once temperatures rise during the second half of RO and the HLF season. They further indicated that shifts in C due to New Breach exchange are outweighed by fluctuations in lake level, which highlights the importance of constant and accurate gaging stations of the three GSL tributaries and the value of the USU head-discharge relationships for the New Breach.

Figure 17

Total, Average Daily River Q to the GSL Plotted Against E_d (a) and South Section Water Surface Elevation Time Series (b) from October 2019 to October 2020.

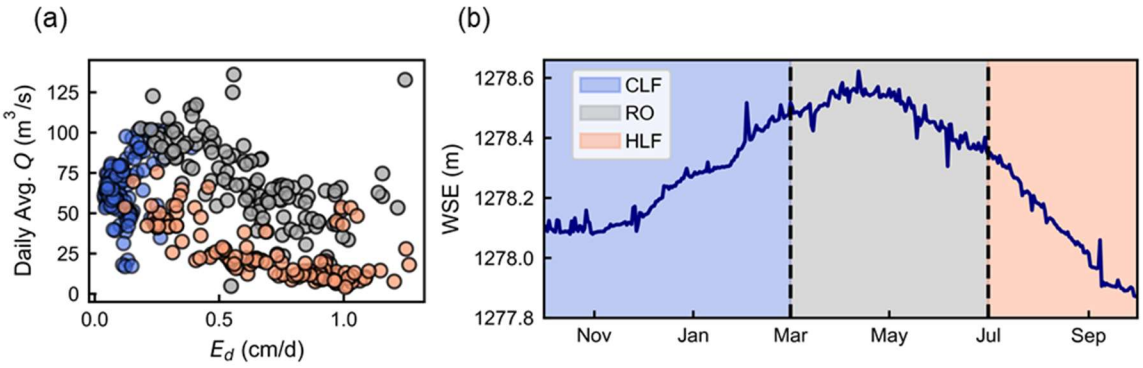

2.5 Discussion

Results from this study inform lake dynamics in response to hydrologic and anthropogenic influences and corresponding uncertainties associated with historically available salinity data. They also generally describe lake dynamics and seasonal salinity forcing; however, this study also highlights challenges associated with limited temporal and spatial datasets.

Lake Monitoring Implications

Data limitations pose challenges for lake management. Models are a commonly used tool to inform management decisions via predicting lake response to management strategies. However, hydrologic data with proper temporal and spatial resolution is not currently available at the Great Salt Lake. Further, to adaptively manage the Great Salt Lake, detailed knowledge of current conditions within the system is necessary to trigger management actions, which should be based upon reliable data.

During the period of analysis, open water C data was drawn from 31 locations with 27 found to be representative of south section conditions $\pm$12.3 g/L. Included in that uncertainty, C was found to vary with space by $\pm$3.97 g/L, across collection and analytical methods by $\pm$6.64 g/L, and due to instrumentation accuracy by $\pm$1.02 g/L. Sampling frequency is an additional source of error but was not evaluated due to the lack of data. The sites that were consistently found to be outliers in the analysis came from the DWiR dataset where sites A, C, M and N are measured in collaboration with USGS. These sites had the highest sampling frequency, approximately every two weeks. Additional insight into C mixing patterns may be found if sampling frequency at the other sites were to increase, especially at the sites where outlier observations weren't captured consistently. However, increasing sampling frequency would require significant, additional resources and may not be feasible due to accessibility issues at the lake. Coordinating sampling locations and standard operating procedure would decrease the total uncertainty from instrumentation and collection/analytical methods and is the most efficient way to improve open water C monitoring at the lake without incurring significant cost.

The need to coordinate measurement and analytical methods is not a new realization. At the date of this publication, UGS, USGS and BSC have adopted a standard operating procedure for ρ sampling and analysis based on results from the Round Robin Study performed in 2020 (Great Salt Lake Salinity Advisory Committee 2020a; Great Salt Lake Salinity Advisory Committee, 2020b). However, specific challenges exist with measuring ρ of hypersaline water. ρ measurements necessitate field collection of samples then transportation to a laboratory for analysis. Samples of highly saturated water contain

salt crystals in suspension (Anati, 1999). The time in transit increases the chance of changes to the number of crystals. Without the natural wave action of the lake, salt precipitation may also occur. Adopting refractometer measurements as the standard is appealing because they can be performed quickly and in-situ, but, like ρ, their accuracy is highly dependent on T. Human error is also introduced when reading the device because it requires estimating percent salinity from the scale within the eyepiece.

Path Forward

The challenges presented with ρ and $\%C$ measurements may be avoided when measuring C in the field via SC following a standardized methodology. SC measurement devices provide a digital reading and automatically adjust for temperature using a standard method. Multimeters and water quality sondes can be expensive, but they should not require laboratory analysis of water samples and now have the capability of measuring brine within the range experienced at the GSL. One significant challenge to overcome with SC measurements is that electrical conductivity does not increase monotonically with salt concentration, exemplified by results from the EQL experiment (Figure 8a). At a certain point, it begins to decrease. However, the range of open water C historically observed in the south section of Great Salt Lake is below this turning point and the regression equation developed in this study improved upon current conversion methods. Additionally, SC of the inflows to Great Salt Lake is monitored continuously. Error in mass balance calculations may be diminished if C within Great Salt Lake and salt loading from its tributaries were measured using the same parameter and at a higher temporal resolution.

SC measurements are recommended for future lake monitoring at current and any additional sites.

Monitoring of Additional Mass Balance Terms

In addition to C within the lake, monitoring of Great Salt Lake mass balance components can also be improved. This study found that BR Q was most significantly correlated with C across all three seasons. Previous studies have also determined that Great Salt Lake volume is most sensitive to changes in total river Q (Mohammed et al., 2012). Therefore, accurately tracking river inflow to the lake should be prioritized.

Current estimates for the BR and WR are insufficient due to significant geographical challenges. The Weber River gage, located at Plain City East of the lake, is upstream from the Ogden Bay Waterfowl Management Area, which is a protected, 20,000-acre wetland. Similarly, the BR gage at Corinne is 42 km northwest of the BR Bay Bridge. It is upstream of the BR Bay Migratory Bird Refuge and the BR Bay that's flanked by mineral evaporation ponds. Accurately tracking sinks, sources, and storage of water and salt in these areas is not currently performed but would be highly beneficial. Continuous monitoring of Q and SC at the BR Bay Bridge, like Farmington Bay Bridge, would allow for better estimation of water inflows and salt loading into the south section and evaluation of the effect BR mixing patterns have on M_{SN} through the New Breach. The current uncertainties in BR Q pose significant challenges for C and lake elevation modeling at GSL since the BR is the largest source of river inflow to the lake, thus until these challenges are resolved, it is recommended to replace the USGS Corrine Gage data with discrete water

quality and discharge measurements at the BR Bay Bridge when available or develop a correction to the Corrine gage data utilizing BR Bay Bridge observations

Other key gaps in the lake mass balance data currently exist. Water is pumped out of the Great Salt Lake for mineral extraction. The volume removed from the lake is reported, but C of the brine leaving the lake is not. Measuring C of the water pumped back to the GSL by the mineral companies would improve lake wide salt mass balance estimates. Contribution of salt mass and water volume from q is also not measured consistently. A constant, yearly value for q was determined by Waddell and Fields (1977) and has been used in modeling studies since. Increasing measurements of groundwater inflow to Great Salt Lake, though small when compared to streamflow, evaporation, and precipitation, would lessen the gap in current mass balance estimates and could facilitate accurate approximation of the ungauged inflow to Great Salt Lake.

2.6 Conclusion

This study compiled and converted, for the first time, all available water quality data that can be utilized to estimate C at the GSL since completion of the New Breach through the causeway in January 2017. Analysis of available GSL C datasets and components of the lake mass balance revealed the spatial and temporal patterns of C within the south section, informed use of historical salinity data by quantifying the variance introduced by combining independent datasets, and highlighted the seasonal influence of key GSL C drivers all of which showcased ways monitoring can be improved.

Available water quality datasets were able to be combined using previously published ρ and $\%C$ conversion equations along with the SC conversion developed within this study. C across open water sampling locations was found to respond similarly to the controls explored except for four sites nearest the river inflow locations. This revealed the spatial extent of inflow currents from the Bear River and Farmington Bay during spring runoff and cold low flow months and informed removal of observations from four sampling locations during these seasons within the compiled C dataset. Analysis of the variance introduced within the filtered south section C datasets showed that the daily median value across sampling locations was representative of south section conditions within ±12 g/L. Since the C dataset characterizes general lake conditions, it has the potential to aid future management decisions and modeling efforts. Seasonal influence of key GSL mass balance components was also determined through correlation analysis. Exchange at the New Breach influenced south section C, however fluctuations in the balance between river inflows and evaporation were the main drivers of change. Based on these conclusions, strategies to improve monitoring at the lake include: more coordination of sampling methods and locations and a recommended shift in standard operating procedure from ρ to SC measurements. GSL mass balance calculations and models could also be improved by accurately tracking flow through the Bear River Bay Bridge, groundwater contribution, and salt export from mineral extraction activities.

As conditions at the lake continue to evolve in response to anthropogenic and environmental stressors, there is an immediate need to determine the most effective means to adaptively manage salt concentrations. Because the lake is a complicated, dynamic

system, the most commonly used tool to inform management actions is modeling which requires data at appropriate spatial and temporal scales. Implementing the strategies discussed in this study would improve upon current practices by increasing salinity sampling frequency, diminishing uncertainty in combining multiple datasets, accurately tracking key components of the lake mass balance, and optimizing the use of private, state and federal resources; all of which aids future modeling efforts and sustainable salinity management at the Great Salt Lake.

3 MODELING GREAT SALT LAKE WATER LEVELS AND SALINITY IN RESPONSE TO ADAPTIVE MANAGEMENT ACTIONS

3.1 Introduction

Since the onset of the Anthropocene, many ecosystems have experienced significant loss of habitat and biodiversity resulting from land conversion and fragmentation, industrialization, infrastructure development, resource extraction, and waste production (Otto, 2018). These stressors also affect terminal saline lakes that sustain unique, diverse biota and are particularly vulnerable to human activity (Hassani et al., 2020). They exist on every continent, excluding Antarctica, and have experienced desiccation due to agricultural and urban water development within their watersheds (Williams, 1996; Wurtsbaugh, 2017). For example, the Aral Sea in Kazakhstan has lost 74% of its volume (Micklin, 1988), Lake Urmia in Iran has been reduced by 90% (AghaKouchak et al., 2024) while Owens Lake in CA, USA was completely lost in 1913 before making a recent reappearance due to management actions (Borlina et al., 2017).

The Great Salt Lake (GSL) in UT, U.S.A. is one of the world's largest and most ecologically and economically productive saline lakes. Its biodiverse food web and wetlands (Belovsky et al., 2011) support breeding and migration for millions of water and shorebirds and it is a critical link in the Pacific Flyway between North and South America (Donnelly et al., 2020). Brine shrimp cyst harvests are used as a food source by global commercial aquaculture operations (Wurtsbaugh 2014). Minerals are also extracted from the hypersaline brine, supplying 14% of the world's magnesium, various salt containing products, and potassium for fertilizer among others (Bioeconomics, 2012). These activities

generate approximately 6,500 jobs and contribute $1.9 billion (adjusted for inflation) annually to Utah's economy (Bioeconomics, 2012).

In recent history, the GSL has been highly modified and managed. An East-West rockfill railroad causeway was constructed in 1959 that segregates the lake into north and south sections (Marden et al., 2020*;*Figure 18); altering the spatial and temporal patterns of water and salt cycling within the lake (Brown et al., 2023). Its natural hydrologic balance has also been altered by significant upstream water withdrawal for agricultural and municipal use (Null and Wurtsbaugh, 2020). Since 2000, these diversions, compounded by a period of prolonged drought (Williams et al., 2020), have triggered significant decline in annual, average lake level and record high salt concentrations (GSL Strike Team, 2023). As a results, economic activities have suffered millions of dollars in damage (Potential Cost of Declining Great Salt Lake, 2019) with projected long-lasting harm to the ecological communities (Barnes and Wurtsbaugh, 2015; Lindsay et al., 2019; Perry, 2019).

Figure 18

The Great Salt Lake and its Bays, Tributaries, and Key Features

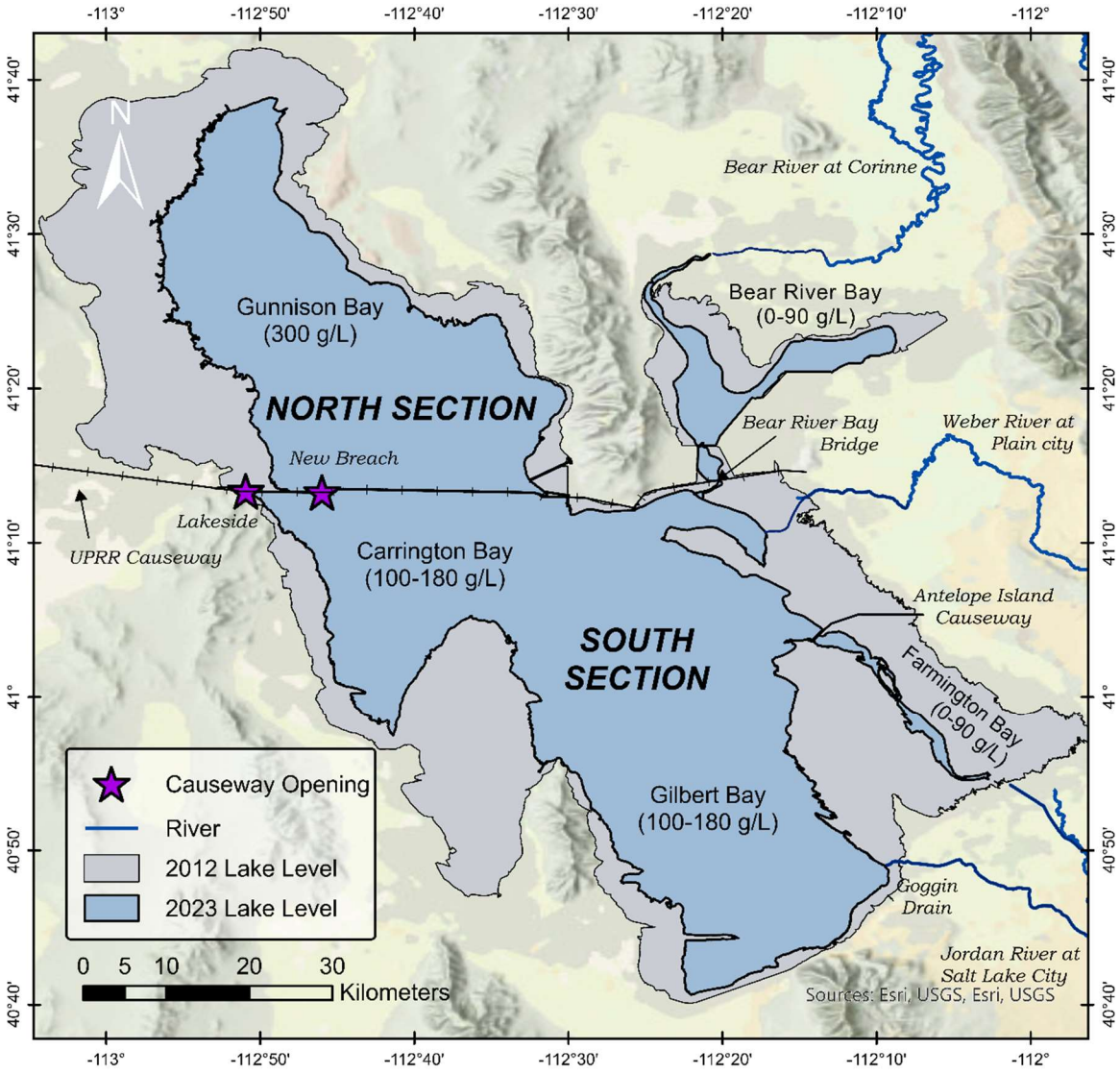

Efforts to minimize GSL desiccation have focused on adaptively managing south section lake levels and salinity. Such efforts are best informed by a detailed understanding of the hydrology and hydraulics of the lake such as the interactions between lake elevation, evaporation, and salinity driven by snowmelt, streamflow, climate shifts, and water/salt

cycling between the sections; made more complex by human activities. Prior work has sought to disentangle these complex relationships by quantifying, chronicling and characterizing changes in south section dissolved salt mass (Brown, 2023; Merck and Tarboton, 2023; Yang, 2020). Previous mass balance models have facilitated the simultaneous exploration of rates of change in lake elevation and water and salt mass in the GSL, but have not been updated for recent hydroclimatic conditions, major modifications to the causeway completed in 2017, or critical bi-directional flow between the north and south sections at the causeway (Waddell and Fields, 1977; Wold et al., 1996; Loving et al., 2000; Mohammed and Tarboton, 2012; White et al. 2015; Jewell, 2021; GSLIM, 2019). Further, the most comprehensive model used by the state of Utah has not been updated with newly developed methods to predict the bi-directional flow exchange (Dutta et al., 2024) and is inaccessible to other technical stakeholders because of the use of proprietary software.

There is a clear need to inform adaptive management of the GSL via development of an open source, process based, mass balance model that encompasses key water and salt mass fluxes, accurately quantifies flow through the causeway, and can predict lake level and salinity in response to historical conditions and recent management actions. This led to the development of a simplified mass balance model, the Utah State University Mass Balance Model (USU-MBM) that captures the complex bi-directional exchanges at the causeway and vertical mixing dynamics within the chemically stratified south section to evaluate adaptive management strategies.

3.2 Study Area

The GSL experiences an arid climate with high evaporation rates. Precipitation falls primarily in the form of snow during the winter months which is followed by substantial spring runoff (Baxter and Butler, 2020). Lake volume is understood to be most sensitive to the balance between river inflows and evaporation (Mohammed and Tarboton, 2012). Typically, lake levels decrease from July to October when temperatures are high, the climate is dry and evaporative volumes exceed river inflows. The inverse is true from November to June where inflow volume outweighs evaporative volume due to snowfall and spring snowmelt (White et al., 2015). GSL water surface elevation also varies at an interdecadal scale triggered by periods of drought or flood (Wang et al., 2010).

The lake's primary tributaries contribute about 66% of total inflows to the lake and include the Bear River (BR) (58% of known, total stream flows to the lake,(Null and Wurtsbaugh, 2020), the Weber River (WR) (15% of total stream flows), and the Jordan River (JR) (22% of total stream flows). The JR enters the lake through Farmington Bay (FB) and the Goggin Drain (GD), the BR flows through the Bear River Bay while WR flows through wetlands and then into the south section (Figure 18). Wurtsbaugh et al. (2017) estimated that these inflows have been depleted by approximately 39% since 1847 which has lowered the lake by 3.4 m (a 64% reduction in volume). 63% of diversions are for agriculture, 11% by cities, 13% by solar ponds and 13% attributed to other uses (Null and Wurtsbaugh, 2020). Groundwater contribution to the lake is not directly measured but has been estimated to be 0.093 km^3 per year (Waddell and Fields, 1977). Additionally,

mineral extraction companies routinely pump water from the north and south sections to evaporation ponds on either side of BR Bay and on the southwest corner of Gilbert Bay (Merck and Tarboton, 2023).

Salinity and nutrient dynamics within the lake are heterogenous due to the rockfill railroad causeway. All GSL tributaries flow to the south section causing distinct density and elevation gradients between the two sides. North of the causeway (Gunnison Bay) generally has a water surface elevation that is 0.3-0.6 m lower than the south section. These waters are typically reddish in hue and near saturation with respect to salt (330 g/L) while the south (Carrington Bay, Gilbert Bay) is a blueish hue with salt concentrations fluctuating between 100 and 180 g/L in response to seasons and water year conditions (Wurtsbaugh, 2014;Figure 18). The BR Bay and FB waters are more dilute, between 0 and 90 g/L (Figure 18). The south section experiences periods of distinct density stratification where a less dense, upper brine layer (UBL) sits above a more dense, deep brine layer (DBL) that has a concentration around 200 g/L (Merck and Tarboton, 2023). Jewell (2021) attributed DBL formation to hypersaline north section brine penetrating the south section through openings in the causeway and seepage across the entire length. Naftz (2014) further documented movement of north section water between Carrington Bay and Gilbert Bay as a high-density current during infrequent high southerly wind events that trigger uni-directional north to south (NS) flow through openings in the causeway. Fluctuations in DBL elevation are influenced by extreme wind events that are believed to induce mechanical mixing through the water column, however full DBL dissipation has only been observed when the causeway openings were closed

(Yang et al., 2020; Wurtsbaugh and Jones, 2012). South section mass loading also occurs from the tributaries; however causeway exchange flows have been understood to be the main driver of salt mass change since 2010 (C. Rumsey, personal communication, May 24, 2023).

The sections of the lake have experienced various levels of connectivity throughout the history of the causeway. Initially, two culverts allowed for limited water and salt mass exchange between the sections (Gwynn and Sturm, 1987). The Lakeside Breach was added in 1984 to counteract high south section elevation because of flooding; however, it became ineffective in the early 2000s when lake levels dropped significantly due to drought conditions. The culverts deteriorated and sank into the lakebed in 2013 and 2014, fully segregating the lake (White et al., 2015). In 2017, a 55 m bridge known as the New Breach was opened to reconnect the lake sections. It features an adjustable rock berm that is raised or lowered to control bidirectional flow exchange that is driven by the density and water surface elevation differences between the north and south sections (Rasmussen, 2022). In 2022, the berm was raised to an elevation of 1276.2 m to limit increasing salinity in the south section, lessening salt mass loading from the north. Despite this rise, the lake reached a record low water surface elevation (WSE) and high concentration. In response, the berm was raised above south section WSE to 1277.7 m, maximizing dilution during spring runoff 2023 and allowing UBL salinity to decrease to 125 g/L prior to summer 2023.

Multiple studies analyzing historical lake salinity and elevation data have been performed since the opening of the New Breach to inform these adaptive management decisions. Merck and Tarboton (2023) documented long-term movement of salt and

changes to salinity in time and space within the lake, primarily focusing on the occurrence and extent of density stratification in the south section. However, they did not quantify DBL/UBL volumes or salt mass transfer between the layers. Brown et al. (2023) calculated dissolved salt mass and major salt fluxes, chronicled salt movement and characterized salinity response within the south section to causeway adaptations since 2010. These studies focused on mass fluxes in the system but did not quantify rates of change in elevation or salt mass nor address the influences of fluctuating water levels on salinity.

Prior GSL modeling studies have been completed to meet varied objectives. White et al. (2015) used mass balance models to simulate proposed New Breach geometries and south section salinity response using the GSL Fortran Model capable of calculating bi-directional flow exchange through the old culverts as documented in Holley and Waddell (1976), Wold et al. (1997) and Loving et al. (2000). These simulations quantified south section salinity response to various bridge designs but did not segregate the south section into UBL/DBL layers. Following construction of the New Breach, new exchange flow models were developed by USU. The first was a computational fluid dynamics model of New Breach flows developed by Rasmussen (2022) using historical WSE and density data and the second was a machine learning model (Larsen, 2024) based upon hydrologic and hydraulic data. A lake wide model, the GSL Integrated Model (GSLIM), was also developed by Jacobs Engineering (GSLIM, 2019). It is a mass balance model integrating river, wetland, and lake modules that can track WSE and salinity in response to changes within the watershed; however, it quantified exchange flows using the Holley and Wadell

(1976) model. Further, GSLIM is proprietary and thus far is not able to predict salt mass to the accuracy desired.

While mass balance modeling approaches have previously been applied at the GSL, to the authors knowledge no model has been formulated with the ability to predict lake levels and salt concentrations from 2017 to present, incorporated new methods to predict New Breach exchange flows, or leveraged all available hydrologic datasets from various stakeholders. Therefore, the USU-MBM is presented herein; it has a simple formulation that incorporates a new method to predict New Breach exchange flows for various submerged berm elevations. It also quantifies UBL/DBL mass partitioning and predicts lake level and UBL salinity in response to recent berm management approaches which is critical to guide future management strategies.

3.3 Methods

3.3.1 Model Formulation

A mass balance approach was taken to simulate GSL lake level and salinity in both the north and south sections. Salt concentration (C), equivalent to salinity, is dependent on water volume (V) and total dissolved salt mass (M), both of which are time variable in the GSL. Therefore, model formulation incorporated both V and M balances to track C at a daily time step. Since current adaptive management of the GSL utilizes the New Breach and its submerged berm, the period of analysis for the USU-MBM is July 2017 until October 2023, which corresponds to the start of stable DBL conditions after opening of the New Breach through raising of the submerged berm to completely restrict exchange flows.

The simulation period was broken into a calibration period (July 2017 to December 2021) and a validation period (January 2022 to October 2023) as discussed in Chapter 3.3.3. Selection of the model time step was informed by GSL hydrologic data and a sensitivity to averaging data on daily, weekly, and monthly scales; a daily time step was chosen because it balances the uncertainty associated with averaging forcing data that vary over short timescales with computational efficiency (computation time for the USU-MBM over the entire simulation period was four minutes on average).

Mass Balance Equations

The GSL was divided into two control volumes to represent the north and south sections (Figure 19). Maintaining healthy salinity and lake levels in the open water portions of the south section are the focus for GSL managers, thus the south section control volumes include Carrington Bay and Gilbert Bay but do not account for Bear River Bay or Farmington Bay. The south control volume is further segregated into two volumes, the UBL and DBL to represent periodic density stratification. The north section was not partitioned as Merck and Tarboton (2023) detected a lack of stratification north of the causeway. They also found the north section, UBL and DBL to be vertically and horizontally homogenous. Thus, the north control volume and both south control volumes were treated as three continuously stirred tank reactors (CSTR) where influx of water V and M are instantaneously mixed causing vertical and horizontal homogeneity.

Figure 19

Conceptual Model Diagram Including Water and Salt Mass Fluxes

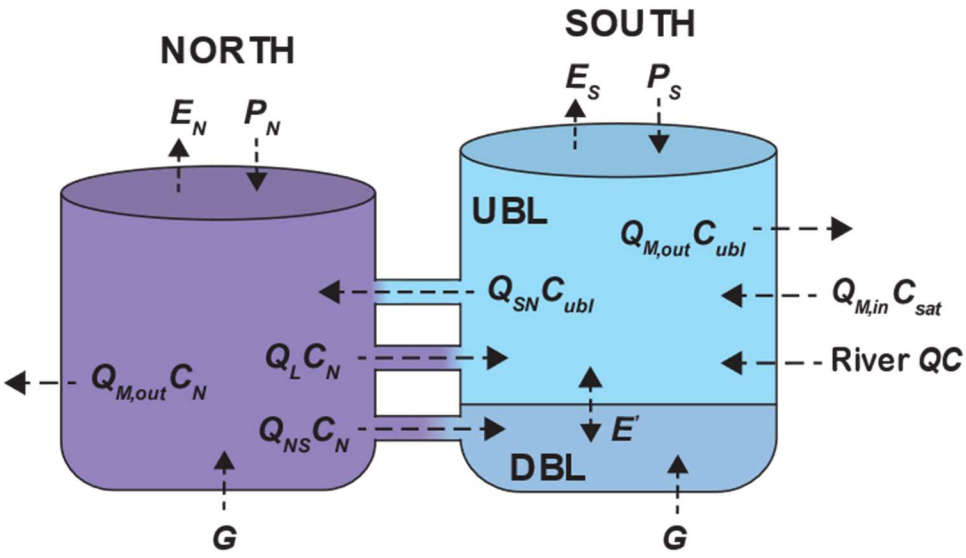

Note. River Q includes surface water inflows from the Bear River, Weber River, Goggin Drain, and Farmington Bay, River C is concentrations of the River Qs, E is evaporation, P is precipitation, G is groundwater contribution, $Q_{m,out}$ is withdrawal for mineral extraction activities, $Q_{m,in}$ is return flow from mineral extraction activities, Q_{SN} is south to north New Breach flow, Q_{NS} is north to south New Breach flow, Q_L is flow through Lakeside Breach, C_N is north section concentration, C_{ubl} is concentration of UBL and E' is mass transfer due to diffusion across the DBL/UBL interface.

Water is supplied to the lake via precipitation (P), surface water discharge from the Bear River (Q_{BR}), the Weber River (Q_{WR}), Goggin Drain (Q_{GD}), and Farmington Bay (Q_{FB}), groundwater (G), and return flows from mineral extraction activities, ($Q_{m,in}$). Lake V is lost to evaporation (E) and water pumped out for mineral extraction, ($Q_{m,out}$) (Figure 19). Water is exchanged between the control volumes via north to south (NS) flow through Lakeside

Breach (Q_L), and bidirectional flow through the New Breach (Q_{NS}, Q_{SN}) (Figure 19). Mineral extraction companies pump water out of both lake sections, thus $Q_{M,out}$ was tracked for the north section and the south section. UBL ~~V~~ fluxes included Q_{BR}, Q_{WR}, Q_{FB}, Q_{GD}, P, E, $Q_{M,out}$, $Q_{M,in}$, Q_{SN}, and Q_L, assuming Qs were fully mixed into the UBL and that the mineral companies pumped brine from the surface of the lake. Jewell (2021), Yang et al. 2020, and Wurtsbaugh and Jones (2012) analyzed drivers of DBL formation and determined that the DBL forms due to Q_{NS} thus DBL ~~V~~ fluxes included Q_{NS} and G (Figure 19). Given these assumptions and ~~V~~ fluxes, the water budget equations for the south section UBL (~~$V_{S,ubl}$~~), south section DBL (~~$V_{S,dbl}$~~) and the north section (~~V_N~~) are:

$$\frac{\partial \cancel{V}}{\partial t}_{S,ubl} = Q_{NS} - Q_{SN} + Q_L + Q_{BR} + Q_{WR} + Q_{FB} + Q_{GD} - Q_{M,out} + Q_{M,in} + P_s - E_s \quad (28)$$

$$\frac{\partial \cancel{V}}{\partial t}_{S,dbl} = Q_{ns} + G \quad (29)$$

$$\frac{\partial \cancel{V}}{\partial t}_{N} = Q_{SN} - Q_{NS} - Q_L - Q_{M,out} + P_N - E_N + G \quad (30)$$

where Q_{BR}, Q_{WR}, Q_{GD}, Q_{FB} = discharge from GSL tributaries [m^3/day], Q_L = discharge from Lakeside Breach [m^3/day], Q_{NS} = north to south discharge through the New Breach [m^3/day], Q_{SN} = south to north discharge through the New Breach [m^3/day], $Q_{M,out}$ = withdrawal from mineral exraction activities [m^3/day], $Q_{M,in}$= return flow from mineral extraction activities [m^3/day], P= precipitation [m^3/day], E= evaporation [m^3/day], and G = groundwater contribution [m^3/day]. The explicit Euler method with upwind differencing

was used to solve the governing water balance equations, determining V_{i+1} (Chapra, 1997; Hoffman, 2001)

Both M and V is exchanged between the UBL and DBLin the south section due to wind induced turbulent mixing. To represent this process in the USU-MBM formulation, a wind mixing algorithm was applied to supplement mass transfer calculated using methods determined by Munk and Anderson (1948) (see Eq. 40 to 46 below), as high GSL brine density precludes conventional methods. This mixing algorithm incorporates a V threshold to quantify M exchange between the DBL and UBL. Based upon limited historical DBL depth observations (C. Rumsey, personal communication, May 24, 2023), V_{dbl} is, on average, 9% of total south section volume (V_S) where $V_S = V_{ubl} + V_{dbl}$ If $V_{dbl,i+1} > 0.09 \times V_{S,i+1}$, a portion of $V_{dbl,i+1}$with concentration equal to the concentration at the beginning of the time step, $C_{dbl,i}$, is mixed into the UBL to maintain this threshold. C_i is then updated prior to quantifying M fluxes. This is calculated using:

$$V^* = V_{dbl,i+1} - 0.09 \times V_{S,i+1} \tag{31}$$

$$C^*_{ubl,i} = \frac{\forall_{ubl,i} C_{ubl,i} + \forall^* C_{dbl,i}}{\forall_{ubl,i} + \forall^*} \quad (32)$$

$$C^*_{dbl,i} = \frac{\forall_{dbl,i} C_{dbl,i} - \forall^* C_{dbl,i}}{\forall_{dbl,i} - \forall^*} \quad (33)$$

where C is in [kg/m^3] and $\forall^*$ = the difference between interim DBL volume and the DBL volume threshold [m^3].

M is contributed to the lake via river Q and exchanged via flow through the New Breach and Lakeside Breach. Mass is also exchange across the UBL/DBL interface due to diffusions. As noted, G is not monitored regularly at the lake. No data for Q or C was available, thus G was assumed to have no salt concentration. Following similar assumptions as the water budget equations and completely mixed systems, salt mass balance for the south section UBL $(\forall C)_{S,ubl}$, south section DBL, $(\forall C)_{S,dbl}$, and the north section, $(\forall C)_N$, are:

$$\frac{\partial(\forall C)}{\partial t}_{S,ubl} = \begin{matrix} Q_L C_{N,i} + Q_{BR} C_{BR} + Q_{WR} C_{WR} + Q_{FB} C_{FB} + Q_{GD} C_{GD} - Q_{SN} C^*_{ubl,i} \\ -Q_{M,out} C^*_{ubl,i} + Q_{M,in} C_{sat} + E'\left(C^*_{dbl,i} - C^*_{ubl,i}\right) \end{matrix} \quad (34)$$

$$\frac{\partial(\forall C)}{\partial t}_{S,dbl} = Q_{NS} C_{N,i} + E'\left(C^*_{ubl,i} - C^*_{dbl,i}\right) \quad (35)$$

$$\frac{\partial(\forall C)}{\partial t}_{N} = Q_{SN} C^*_{ubl,i} - Q_{NS} C_{N,i} - Q_L C_{N,i} - Q_{M,out} C_{N,i} \quad (36)$$

where C_{BR}, C_{WR}, C_{FB}, C_{GD} = salt concentration of GSL tributaries [kg/m^3], $C_{N,i}$ = salt concentration of the north section at time step i, $C_{ubl,i}$ = salt concentration of the UBL at time step i, $C_{dbl,i}$ = salt concentration of the DBL at time step i [kg/m^3], C_{sat} = salt concentration of water at saturation kg/m^3, and E' = turbulent diffusion coefficient [m^3/d]. Merck and Tarboton (2023) found that 25% of total $\forall$ pumped from the lake for mineral extraction returns to the south section at halite concentration, thus C_{sat} was assumed to be constant with a value of 275 g/L. Following the CSTR assumption, C of the brine removed from the north section along with Q_L and Q_{NS} were assumed to be equal to C_N while C of the brine removed from the UBL and Q_{SN} were assumed to equal C_{ubl}. The explicit Euler method was also used to calculate C_{i+1}. If UBL/DBL C equalized at the end of the time step or due to wind mixing, the DBL was mixed completely into the UBL, and DBL growth was allowed until the $\forall$ threshold was met again. For periods where $\forall_{S,dbl}$ is small during DBL formation (less than 10,000 m^3), the model sets $\frac{\partial C}{\partial t}_{S,dbl}$ equal to 0 to avoid unstable outputs in DBL C prior to full formation of the DBL.

Two lake processes have been observed but are not accounted in the USU-MBM; 1) seepage through the causeway and 2) salt crystal deposition/re-entrainment (Jewell, 2021; Oillon et al., 2019). Jewell (2021) found that seepage along the causeway contributed to DBL formation using data from 2008 to 2015. The causeway is routinely modified by the Union Pacific Railroad who add rock and fill material which locally alters seepage rates and introduces high uncertainty in any seepage estimate and corresponding salt transfer. Thus this aspect of the system is not included in the model formulation Jagniecki et al. (2021) observed salt precipitation from the water column in the north section during winter months when the water temperature (T) decreases and re-dissolution of salt from the north lakebed due to wave action when water T rises. Although this may be a significant source of M, specific methods to describe these dynamics at the GSL have not been developed.

Mass Balance Terms

Daily volume of precipitation P for each side of the lake was estimated by:

$$P = P_d \times A \tag{37}$$

where P = precipitation volume, unique for each lake section [m^3/d], P_d = precipitation depth [m/d] and A =surface area [m^2] that is a function of time and WSE. A is dependent on lake V, which is calculated for each section at each timestep based on the U.S. Geologic Survey's relationship between A and V for each bay as a function of WSE (Root, 2023). For this study, south section A and V were calculated using these tables by summing values for Carrington Bay and Gilbert Bay, excluding Farmington Bay and Bear River Bay which are not accounted for in the USU-MBM.

The same method was employed to calculate volume of E off the lake's surface:

$$E = E_d \times A \tag{38}$$

where E =evaporative volume unique for each section [m^3/d] and E_d= evaporative depth [m/d] which was calculated using Eq. 9-26 outlined in Chapter 2.3.2.

Groundwater contributions are not monitored at the GSL; a yearly total of 0.093 km^3/yr. was included herein based upon Loving et al. (2000). Due to lack of monitoring, G was assumed to be freshwater and was divided evenly between the north and south sections to estimate constant, daily groundwater contribution to the lake. Eq. 35 and 36 also includes the bulk turbulent diffusion coefficient at each time step i (E') which was estimated per Chapra and Martin (2004):

$$E' = \frac{A_i E_i}{\frac{H_i}{2}} \tag{39}$$

where A_i =surface area of the DBL/UBL interface[m^2], H_i =depth of the south section [m], and E_i = turbulent diffusion coefficient across the UBL/DBL interface [m^2/d] (Munk and Anderson, 1948):

$$E_i = \frac{E_0}{(1 + aR_i)^{0.5}} \tag{40}$$

where E_0 = the maximum diffusion coefficient [m^2/d], a = a tuning coefficient, and R_i = Richardson number. The maximum diffusion coefficient was calculated using (Sundaram and Rehm, 1973):

$$E_0 = cU^*$$

(41)

where c = a tuning coefficient and U^* = shear velocity [m/s]. The tuning coefficient c was calculated at each time step using (Chapra and Martin, 2004):

$$c = \frac{WSE_s - H_0}{34}$$

(42)

where WSE_s = daily WSE of the south section [m], and H_0 = the lowest point along the lakebed within the south section [m], equal to 1267 m. Both a and c became the primary tuning coefficients used to calibrate mass transfer between the south section layers during model calibration. Shear velocity at the surface, U^*, was taken as (Chapra and Martin, 2004):

$$U^* = \sqrt{\frac{\rho_{air} C_d v_w^2}{\rho}}$$

(43)

where ρ_{air} = density of the air (assumed equal to 1.2 kg/m^3), C_d = dimensionless drag coefficient (assumed equal to 1.3×10^{-3}), v_w is at model time step I [m/s], and ρ = density of the water [kg/m^3]. The Richardson number, a dimensionless number that relates the buoyancy to shear forces generated through the water column, was calculated using (Ford and Johnson, 1986):

$$R_i = -\frac{\left(\frac{g}{\rho}\right)\left(\frac{\partial \rho}{\partial z}\right)}{U^*/(z_s - z)^2} \quad (44)$$

where g = acceleration due to gravity (equal to 9.81 m/s^2), $\partial\rho/\partial z$ = the gradient of density with depth, z_s = WSE of the south section [m] and z = elevation at which the Richardson number is computed [m], in this case the DBL/UBL interface. The ρ gradient at DBL/UBL interface was computed with a finite divided difference (Chapra, 1997):

$$\frac{\partial \rho}{\partial z} = \frac{\rho_i - \rho_{i+1}}{z_i - z_{i+1}} \quad (45)$$

where ρ_i = density of the UBL [kg/m^3], ρ_{i+1}= density of the DBL [kg/m^3] , z_i= elevation of the midpoint of the UBL [m], and z_{i+1} = elevation at the DBL midpoint [m].

To calculate Q_{NS} and Q_{SN} as a function of lake conditions and New Breach berm geometry, an analytical formulation was developed based upon a USGS New Breach velocity profile dataset (from an ADCP up-looker) that allowed for consideration of four flow scenarios: 1) a no-flow case (berm height exceeds water surface elevation), 2) the most common bi-directional flow scenario (Q_{NS} and Q_{SN}), 3) unidirectional flow Q_{NS}, and 3) unidirectional flow Q_{SN}. The analytical formulation used energy conservation via Bernoulli's equation in a one-dimensional formulation of specific energy, referencing berm height, water surface elevations, density of the lake sections, and the location of the flow interface between the exchange flows, to estimate Q_{NS} and Q_{SN} via empirical rating curves fit to New Breach Q (Dutta et al., 2024):

$$Q_{NS} = 2.4H_I^{1.7}; \quad \text{berm elev.} = 1275 \text{ m} \tag{46}$$

$$Q_{NS} = 1.08 \times 10^{-8}(H_I - 2.97)^{14.97}; \quad \text{berm elev.} = 1276.2 \text{ m} \tag{47}$$

$$Q_{SN} = 4.51(H_T - H_I)^{1.64}; \quad \text{berm elev.} = 1275 \text{ m} \tag{48}$$

$$Q_{SN} = 1.85(H_T - H_I)^{0.97}; \quad berm\ elev. = 1276.2\ m \tag{49}$$

where Q is in [m^3/s] and α and b are dimensionless curve fit parameters, unique to each berm case, H_I = flow interface between NS and SN flow, and H_T= the height of the water flowing over the berm [m].

The flow interface was calculated using (Dutta et al., 2024):

$$H_I = \frac{\rho_N H_N - \rho_S H_S}{\rho_N - \rho_S} - \frac{C_{NS} \cdot V_{NS}^2}{2g} \cdot \frac{\rho_N}{\rho_N - \rho_S} + \frac{C_{SN} \cdot V_{SN}^2}{2g} \cdot \frac{\rho_S}{\rho_N - \rho_S} \tag{50}$$

where ρ_N = density of the north section [g/cm^3], ρ_S= density of the south section (assumed to be density of the UBL) [g/cm^3], H_N = height of the north section water surface [m] above the bottom of the New Breach (elev. 1272.9 m), and H_S = height of the south section water surface [m] above the bottom of the New Breach, V_{NS} = average NS flow velocity [m/s], V_{SN} =average SN flow velocity [m/s], g = gravitational constant, equal to 9.81 [m/s^2], and C_{NS}, C_{SN} = dimensionless coefficients to correct for friction loss and non-uniformity. For the 1275 m berm: C_{NS} = 1.71 and $C_{SN} = -1.84$. For the 1276.2 m berm: C_{NS} = 19.34 and

$C_{SN} = -0.43$. These coefficients are dependent on berm elevation and were developed by comparing flow interface calculations to the ADCP velocity data (Dutta et al., 2024). The height of the water above the berm was calculated using (Dutta et al., 2024):

$$H_T = H_S - \frac{C_{SN} \cdot V_{SN}^2}{2g} \tag{51}$$

Since H_T and H_I are dependent on V, which is unknown at each model time step, H_S was used as an initial value for H_T and an initial value of H_I was calculated using (Dutta et al., 2024):

$$H_{I,initial} = \frac{\rho_N H_N - \rho_S H_S}{\rho_N - \rho_S} \tag{52}$$

The rating curves were then solved to get initial Q_{NS} and Q_{SN}.

For the 1277.7 m berm case, flow scenario 4 occurs and the berm was treated as a broad-crested rock weir (Dutta et al., 2024):

$$Q_{SN} = C_w \cdot L \cdot {H_S}^{1.5} \tag{53}$$

where C_w = weir discharge coefficient, equal to 1.6 and calibrated based on USGS discrete Q measurements at the New Breach, L i= length of berm, equal to 30.5 m, and H_S is in [m]. These equations are a significant simplification of the hydraulics at the New Breach, but do cover a viable range of geometric conditions of the submerged berm specific to the New Breach geometry.

An adjustment was performed on the empirical rating curves before incorporating them into the model. Eq. 47-50 and Eq. 54 were applied over their corresponding time periods (2017/7/1 - 2022/7/21 for low elev. 1275 m, 2022/7/22 – 2023/2/13 for medium elev. 1276.2 m and 2023/2/14 – 2023/9/30 for high elev. 1277.7 m). Historical observations of ρ and WSE for the UBL and north section from the calibration/validation dataset were used as inputs to the rating curves. The outputs were then compared against discrete measurements of Q_{NS} and Q_{SN} at the New Breach, which were compiled from NWIS (USGS, 2023) and linearly interpolated to prepare a daily series. The average daily difference between the predicted and observed Q_{NS} and Q_{SN} was calculated for each berm elevation and reported as a percent of the predicted. The resulting percent error was incorporated into the model using:

$$Q_c = Q + Q \times \%_d \tag{54}$$

where Q_c = corrected Q [m^3/d] and $\%_d$ = percent difference, unique to each berm elevation and flow direction. The root mean squared percent error (RMSPE) for the raw and corrected rating curve outputs compared to the interpolated, observed Q values were calculated over the entire time series to evaluate the performance of this adjustment and validate its use within the USU-MBM.

3.3.2 Data Preparation

Forcing Data Preparation

From January 2017 to June 2022, the berm was at its lowest elevation of 1275 m. July 2022, it was raised to a medium elevation of 1276.2 m and in February 2023 it was

raised to its highest elevation of 1277 m fully segregating the sections. Forcing data including Q and C of river inflows, P_d over the lake, and climatic variables included in estimating E_d off GSL was compiled for the USU-MBM to capture the hydroclimatic conditions surrounding these management actions and for use in calculating terms within the mass balance.

During the simulation period, Q and C data for BR, WR, FB, GD, and Lakeside were compiled from the U.S. Geologic Survey's (USGS) National Water Information System (NWIS) database (USGS, 2023) using the dataretrieval package in python (Horsburgh et al., 2022). 15-minute continuous Q observations were available for BR, WR, FB, and GD while discrete measurements of Q at Lakeside Breach were taken approximately every two months (Table C3; Figure C1). The continuous Q data was averaged over each day while the discrete measurements at Lakeside were linearly interpolated to provide a daily time series for each site.

Previous GSL models have used Q_{BR} data from the USGS gage along the BR at Corinne, UT (10126000) approximately 42 km north and west of the BR-GSL confluence at BR Bay bridge. However increases/decrease in Q and salt mass loading occur between this gaging station and the BR Bay bridge (10010060) due to lateral stream inflows, the BR Migratory Bird Refuge and conveyance associated with the evaporation ponds on either side of BR Bay. Therefore a correction was performed in this study using a seasonal, linear regression between day of the water year and the difference between discrete Q measurements made at the BR Bay bridge and daily BR gage Q. This correction was applied via:

$$Q_{BR,pred} = Q_{BR,gage} + Q_c(WY) \quad (55)$$

where $Q_{BR,pred}$ is predicted BR flow through the BR Bay bridge [m3/d], $Q_{BR,gage}$ is Q measured at the BR gage [m3/d], and $Q_c(WY)$ is the $Q_{BR,gage}$ correction as a function of the day of the water year [m3/d]. RMSPE was calculated for the corrected and uncorrected BR gage Q compared to the BR Bay bridge discrete Q measurements to determine the effectiveness of this correction.

C of the flows from the BR, WR, GD, and FB was not directly measured, therefore, water quality data including specific conductance (SC) and ρ was compiled from NWIS (USGS, 2023) and converted to C in g/L following the methods employed in Chapter 2.3.2 (Table C3). 15-minute continuous SC data was available for water years 2019, 2022, and 2023. The gaps in the SC data for these sites were filled with ρ observations taken from samples collected monthly. A daily average of the continuous C data was performed; additional gaps in C time series were linearly interpolated between measurements. While ρ at the BR Bay bridge is generally higher than at the BR gage, there was clear trend to formulate an appropriate ρ correction. Instead, ρ at the BR Bay Bridge was prioritized and any missing data was provided by the BR gage.

Yearly withdrawals for each mineral company were compiled from a public USU dataset (Tarboton, 2024). Since 2017, four companies have harvested minerals including Cargill Salt Inc., Morton Salt Inc., and U.S. Magnesium LLC from the south section and Compass Minerals from the north section. Detailed information on the extraction operations are privately held, thus for this study published yearly withdrawal V from each

company corresponding to each side of the GSL was divided evenly across days within the year to calculate constant, daily $Q_{m,out}$. Daily P data was obtained from Oregon State University's PRISM Climate Group (Daly et al., 2008) using Climate Engine (Huntington et al., 2017). The data was reported at a 4 km grid resolution. Cells falling over the GSL were identified using a GSL lake shapefile provided by Tarboton (2024); the data within each cell was averaged to produce a daily time series of P_d for use in Eq. 38.

Hourly climate data including v_w, T_d, and site pressure (p_{site}), $T_{a,max}$ and $T_{a,min}$ was obtained from Utah State University's Utah Climate Center (USU, 2024) from three sites on the GSL (Figure C1; Table C2). 15-minute v_w was also measured by the USGS at the New Breach and compiled from NWIS (USGS, 2023; Table C2). A daily average was applied to the continuous data at individual collection sites. After evaluating the spatial variance of the datasets across the collection sites, a single, spatial average value for each variable was generated and understood to be representative of GSL conditions (Figure C2).

Testing Data Preparation

Historical observations of C, V, and M for each control volume were gathered over the entire simulation period for use establishing initial conditions and calibrating and validating the USU-MBM (Dunn, 2024b). UBL, DBL and north section C were derived from sample ρ, SC and T data while the UBL C dataset also included percent salinity ($\%C$) measurements. ρ and T data was compiled from the NWIS (USGS, 2023), the Utah Geologic Survey's (UGS) Brine Chemistry Database (UGS, 2020), and water quality monitoring reports from HDR Engineering published by the Utah Department of Water Quality (UDWQ, 2022). Five sites were available for the north arm, eleven sites reported

UBL and DBL samples and eighteen sites reported just UBL samples (Table C1; Figure C1). DBL and UBL SC data was collected at two sites in the south section by the Brine Shrimp Cooperative (BSC) and published in Brown et al. (2023) while the Department of Wildlife Resources (DWiR) collected $\%C$ measurements of the UBL at 15 sites. Additional details on the collection and analytical methods each entity used to develop these datasets are documented in Chapter 2.3.1.

To test the ability of the modeling approach to reproduce DBL and UBL C and $\forbar{V}$, a depth to DBL dataset, developed by the USGS using SC profiles taken at one site in Carrington Bay and one in Gilbert Bay (C. Rumsey, personal communication, May 24, 2023), was used to curate C, $\forbar{V}$ and interface elevation time series for the UBL and DBL. Daily DBL/UBL interface elevation was calculated individually for Carrington Bay and Gilbert Bay by linearly interpolating between observations of DBL depth and subtracting from daily, historical south section WSE observations.

To curate the C time series, C measurements above the calculated DBL interface within each bay were apportioned to the UBL, and below to the DBL. Whenever profile measurements were taken, values within the north section, UBL and DBL were averaged section, constituting a single representative value at the time of sampling. C measurements were then supplemented using linear interpolation to develop daily time series at each sampling location. Daily median UBL, DBL and north section C were calculated by averaging across sites, assuming spatial homogeneity, and are presumed to be representative of conditions within each control volume.

Measurement uncertainty, combining multiple independent data sets, applying various C conversion equations, and the spatial homogeneity assumption introduce uncertainty into the calibration/validation dataset. It is necessary to keep these uncertainties in mind when evaluating USU-MBM performance; therefore 90% confidence intervals (CI) were developed for the representative C time series. Development of the 90% CI for the UBL dataset is discussed in Chapter 2.3.4 while DBL and north section intervals were calculated in this chapter following the same method. The daily, north section dataset only included ρ observations thus the average standard deviation (σ) across all north section sites during the entire modeling period and the C resulting from the reported ρ measurement accuracy was calculated. The DBL dataset included ρ and SC data, thus it was broken into two subsets, one for each variable. Average σ through space and due to measurement uncertainty for both subsets were calculated. Variance from combining datasets was also explored by calculating average σ between the daily time series at BSC site L/USGS site B and BSC site K/USGS site *E*. A first order error analysis was performed on σ to determine total σ for the DBL and north section C time series due to these sources of uncertainty (Berthouex and Brown, 2002):

$$\sigma_T = \sqrt{\sum_{i=1}^{n} \sigma_1^2 + \sigma_2^2 + \sigma_3^2 + \cdots + \sigma_n^2} \tag{56}$$

where σ_T [g/L] = total standard deviation in C given all error sources, n = total number of error sources, and σ_1^2 , σ_2^2, σ_3^2, σ_n^2 [g^2/L^2] = average variance associated with each error

source. Using σ_T, 90% CI for the representative C time series were calculated using (Berthouex and Brown, 2002):

$$CI_{90\%} = \overline{C} \pm 1.65\sigma \quad (57)$$

where $CI_{90\%}$ = 90% confidence interval, $\overline{C}$ = daily median C [g/L] of the UBL, DBL or north section on any given day. These intervals were applied to the representative C time series and used to evaluate USU-MBM performance during the model formulation and calibration processes.

Continuous, 15-minute observations of north and south section WSE were available from NWIS (USGS, 2023; Table C2). The continuous data was averaged to determine daily WSE for both sections The USGS reported a ± 3 cm accuracy in their WSE data which was used in Eq. 58 to develop a 90% CI surrounding the historical WSE time series. This confidence interval was applied to the daily, historical WSE time series for the UBL and north section when comparing USU-MBM outputs to the historical observations. The USU-MBM incorporates both Gilbert and Carrington Bay into the UBL/DBL control volumes but the DBL depth dataset records individual depths within each bay. Therefore, a representative DBL elevation was determined by summing DBL volumes for Carrington Bay and Gilbert Bay using the DBL elevation data and the USGS WSE/A/V tables. This total DBL volume was then related to south section WSE using the curated WSE/A/V table described in Chapter 3.3.1 to produce a representative DBL elevation for the DBL control volume.

The curated historical WSE time series were converted to $\not{V}$ using the USGS WSE/A/ $\not{V}$ tables (Root, 2023). UBL $\not{V}$ was calculated by subtracting total DBL $\not{V}$ from total south section $\not{V}$. Combining the C and $\not{V}$ time series, daily M was then calculated for the UBL, DBL, and north section using (Chapra, 1997):

$$M_i = \not{V}_i \times C_i \tag{58}$$

where M_i is in [kg], $\not{V}_i$ is in [m^3], and C_i is in [kg/m^3] for any given layer. The published uncertainty in USGS WSE data (±3 cm) was also converted to $\not{V}$ using the USGS tables. Combining uncertainties from the $\not{V}$ and C time series, relative uncertainty in daily M was determined using (Berthouex and Brown, 2002):

$$\frac{\sigma_{M_i}}{\bar{M}_i} = \sqrt{\left(\frac{\sigma_{C_i}}{\bar{C}_i}\right)^2 + \left(\frac{\sigma_{\not{V}_i}}{\bar{\not{V}}_i}\right)^2} \tag{59}$$

where σ_{M_i} = standard deviation of the M within a given layer, $\bar{M}_i$ = average M within a given layer, $\left(\frac{\sigma_{C_i}}{\bar{C}_i}\right)^2$ = total, relative variance in C for a given layer, and $\left(\frac{\sigma_{\not{V}_i}}{\bar{\not{V}}_i}\right)^2$ = total, relative variance in $\not{V}$ for a given layer. A daily confidence interval for M (Eq. 58) was also calculated for use in evaluating USU-MBM performance.

3.3.3 Model Calibration and Validation

The beginning of the calibration period was July 2017, aligning with the start of stable DBL conditions. Based on historical observations, the DBL experienced abrupt increases and decreases in volume immediately following opening of the New Breach

(January – July 2017) due to complex mixing patterns triggered by abnormally large exchange flows. It was necessary to start the calibration period under stable DBL conditions because the physics of DBL initiation after breaching the causeway cannot be characterized with the simple 1D model formulation. December 2021 was selected as the end of the calibration period because it provided enough time within the validation period to validate the USU-MBM's performance under all three historical berm elevations.

Model calibration focused first on addressing underprediction in north and south section WSE. E_d was selected as the WSE calibration parameter because Eq. 9 was document to overpredict E_d by Mohammed and Tarboton (2012). A percent reduction in E_d for the north section ($\%E_N$) and south section ($\%E_S$) was determined by performing model runs over the calibration period to test various combinations of values ranging from 0.5 to 0.95. Separate values were explored for the north and south sections due to the extreme C differences between the two. A 10% reduction in E_S ($\%E_S = 0.9$) and a 25% reduction in E_N ($\%E_N = 0.75$) applied during the summer months (May to August) resulted in the lowest RMSE values between observed and predicted WSE and was incorporated into the USU-MBM (Table 6).

Table 6

Calibrated Parameters and Constants Used in the USU-MBM.

Variable	Value	Units
a	20	-
Cc	0.05	-
$\%E_S$	0.90	-
$\%E_N$	0.75	-
g	9.81	m/s^2

C_d	1.3×10^{-3}	-
ρ_a	1.2	kg/m^3
C_{sat}	275	g/L

The coefficients *a* and *c* used in the turbulent diffusion coefficient calculations were then calibrated to address error in south section M partitioning, effecting C outputs. The USU-MBM was run over the calibration period with a incremented within the suggested range of [10, 30] (Chapra and Martin, 2004). The equation for c was not developed for hypersaline environments. Due to the extreme ρ of GSL waters, a reduction factor (Cc) was explored by incrementing Cc values between 0.05 and 0.95 to determine an appropriate percent reduction in *c*. Based on RMSE results, optimized *a* and Cc were 20 and 0.05, respectively (Table 6).

Terminal Lakes have long residence times; thus model validation was performed as an extension of the calibration period to avoid initial condition biases that may mask model performance. RMSE values during the validation period were calculated for USU-MBM predictions of: elevation of the north section, UBL, and DBL (derived from $\forall_N$, $\forall_S$, and $\forall_{dbl}$) and C_{dbl}, C_{ubl}, C_N. Due to this methodology, when evaluating RMSE results it is important to note that any propagated errors passing through the calibration period are maintained and captured within the validation period.

3.3.4 Impacts of Forcing Data Error

USU-MBM performance is affected by the accuracy of the forcing data and the methods used to calculate Q_{NS}, Q_{SN}, and Q_{BR}. An error analysis was performed to understand how these errors propagate through the system by running a series of model simulations.

The entire simulation period was considered to ensure USU-MBM sensitivity was evaluated under all Q, climatic and New Breach berm conditions. Each mass balance term was either increased or decreased individually within a given simulation based on the upper and lower bounds of their associated error. P had a reported ±10% error based on analysis performed by Daly et al. (2008). Error in surface water Q and C, excluding corrected Q_{BR}, was based on values documented by the USGS; ± 5% for Q (Oberg et al., 2005), ± 0.001 g/cm^3 for ρ (USGS, 2019a) and ± 5% for SC (USGS, 2019b). Climate data error due to instrumentation accuracy reported within manufacturer documentation was determined to be ± 0.5 °C for T, ± 0.3 m/s for v_w, and ± 0.3 hPa for p_{site} (University of Utah, n.d.). For the Q_{NS}, Q_{SN} and Q_{BR} correction, the RMSPE of the corrected time series was designated. The RMSE for C_{ubl} between results from each simulation and the simulation of historical conditions was calculated to determine the most effective ways to improve the USU-MBM and how this could impact future decisions informed by the model.

3.3.5 Management Scenarios

With the calibrated USU-MBM, simple management scenarios were simulated to exemplify the model's ability to simulate berm management strategies and to explore how adaptations to the New Breach berm affect UBL C within the UBL. Three management scenario simulations were performed; one where the berm was at a low elevation of 1275 m throughout the entire simulation period, one with the berm at a medium elevation of 1276.2 m, and one with the berm at a high elevation where the south section is fully isolated, 1279 m. These berm conditions were chosen within the simulations to isolate the effect each berm elevation has on C and WSE over the range of conditions experienced at

the lake since the New Breach was constructed. UBL C outputs from each of the three simulations were compared against the simulation of historical conditions that incorporated a low berm elevation July 2017 – June 2022, medium berm July 2022 – February 2023, and berm elev. 1277.7 m February 2023 – September 2023. This comparison was made to evaluate the influence of each berm elevation, efficacy of previous adaptive management decisions, and the success of the berms as a management tool.

3.4 Results

3.4.1 Rating Curve Adjustment

After analyzing the performance of the rating curves during model formulation, the 1275 m and 1276.2 m berm case equations were found to underpredict Q_{SN} while the 1277.7 m equation performed well (Figure 20a); necessitating a positive correction factor for the 1275 m and 1276.2 m Q_{SN} predictions (1.68 and 1.5, respectively). For Q_{NS}, the 1275 m equation predictions were in good agreement with peak Q observations, but failed to predict the low Q_{NS} values, requiring a negative correction factor (-0.45). The 1276.2 m Q_{NS} equation slightly underpredicted Q (Figure 20b); however, measured and predicted Q_{NS} was small thus the 1276.2 m Q_{NS} equation was not corrected. Historically, when the berm is at 1277.7 m, Q_{NS} is zero therefore no correction factor was calculated for this case. These corrections were applied throughout the entire simulation period. The raw Q_{SN} rating curve outputs across all berm conditions had an RMSPE of 157% while the corrected Q_{SN} RMSPE was 67%. For Q_{NS}, the uncorrected RMSPE was 184% and the

corrected RMSPE was 85%; showing that these corrections improved rating curve performance for both flow directions.

Figure 20

New Breach Rating Curve Correction Results for (a) Q_{SN} and (b) Q_{NS}

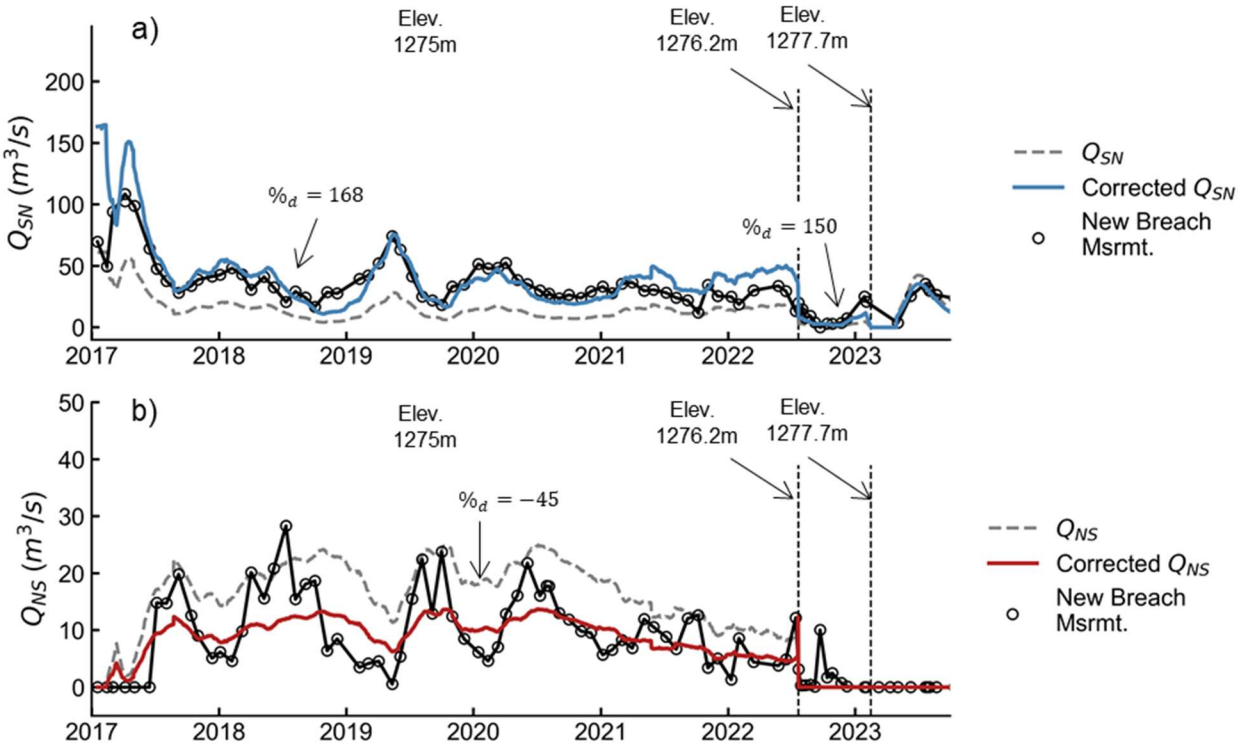

3.4.2 Data Preparation

Forcing data was prepared for the USU-MBM including P, surface water Q and C, and climate variables (Figure 21; Figure S3). Results from the forcing data preparation show that the smallest contributor of inflow volume to the GSL was Q_{GD}, followed by Q_L, Q_{WR}, then Q_{FB} while the largest contributor was Q_{BR} (Figure 21c). $\forall$ gained via P can exceed surface water inflow volumes during storm events but does not cumulatively

contribute more V than the GSL tributaries (Figure 21a). More north section brine is pumped out of the GSL than south section brine while return flows are like inflow volumes from GD (Figure 21b). Finally, of the surface water inflows, FB had the highest C due to mass loading within FB before entering the south section while all other inflows exhibited relatively low C (Figure 21d).

Figure 21

Daily Time Series of the Prepared Forcing Data from Water Year 2020

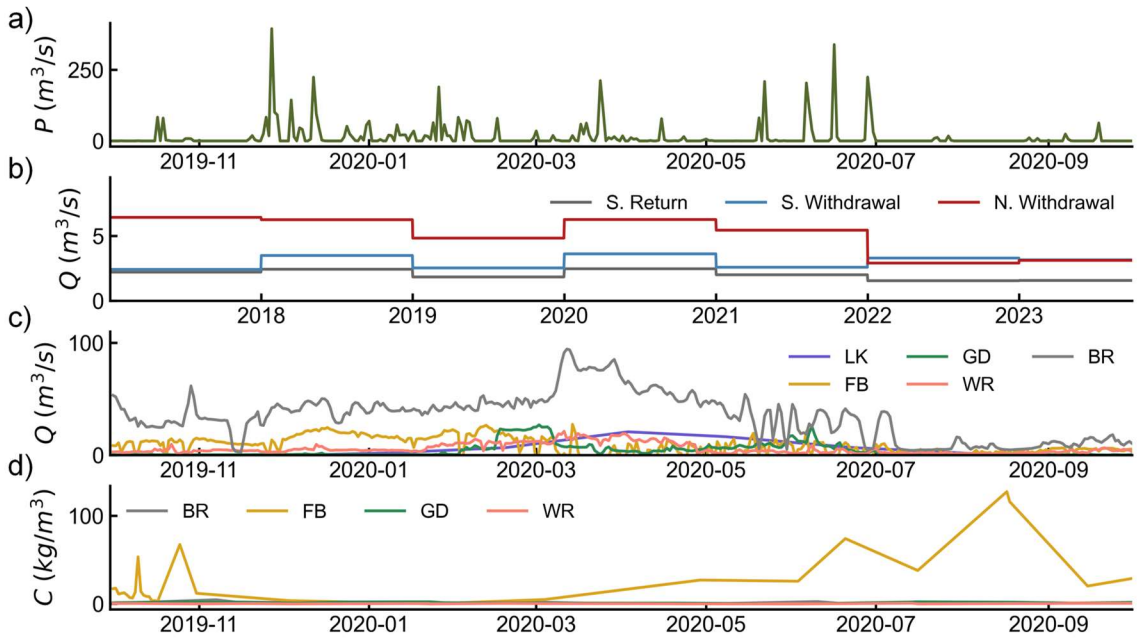

Note. In plot (a) precipitation data is converted to a volumetric flow rate for comparison to the other volume fluxes, plot (b) includes withdrawal and return Q from the mineral extraction activities, (c) includes river Qs and (d) includes C of the river Qs (C). Data in plot (b) is shown for the entire simulation period to showcase yearly shifts in flow volumes from the mineral extraction activities.

Given the large contribution of flow from the BR compared to other river inflows, it was necessary to apply a correction to the BR gage data to better account for the significant deviation in Q_{BR} between the BR gage and the BR Bay Bridge as discussed in chapter 3.3.2 (Figure 22). During winter and spring runoff, Q through the BR Bay Bridge is higher than values observed at the BR gage due to P falling over BR Bay between the two locations paired with low E rates (Figure 22a). During summer and fall, the flows are generally the same (Figure 22b) with the potential to be lower during late summer when E rates are highest; exemplified by the negative Q differences around day 200 (Figure 22a). RMSPE between the raw $Q_{BR,gage}$ and BR Bay Bridge measurements during the period of analysis was 88%, while the RMSPE for the corrected BR gage data was 68%; demonstrating improved estimation of Q_{BR} for use in the model.

Figure 22

Bear River Discharge Correction Results

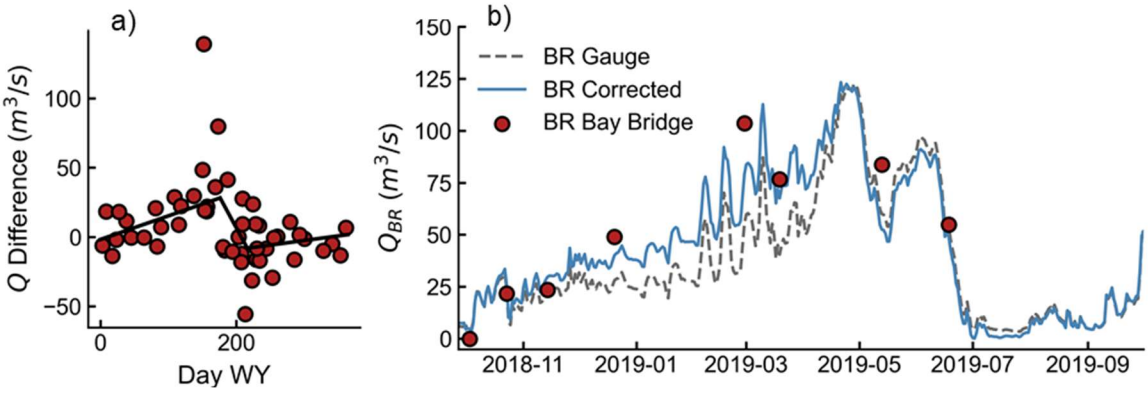

Note. Plot (a) shows the difference between Bear River discharge, Q, at the BR gage and the BR Bay Bridge versus day of the water year, WY. Plot (b) shows the corrected Q_{BR} series used in the model for water year 2019.

A first order error analysis was performed on C_{UBL}, C_{DBL}, and C_N from the calibration/validation dataset and produced a range of uncertainty associated with the prepared data. 90% CI for the UBL was ±16 g/L, ±52 g/L for the DBL, and ±24 g/L for the north section (Table 7). The largest source of uncertainty for the UBL came from combining datasets (UBL σ = 6.64 g/L) but came from averaging through space for the DBL and north section (DBL σ = 18.8 g/L, north section σ = 14.9 g/L) (Table 7). Spatial variability within the DBL was the highest, which may be partially explained because the depth to DBL dataset used to calculate DBL elevation within Carrington and Gilbert Bay was derived using data from only one site in each. Because this dataset may not describe DBL elevation accurately at every point, an artificial decrease in the vertically averaged DBL C at sites where the DBL was shallower than recorded is probable. This exemplifies the need for increased monitoring of the DBL to deepen understanding of its dynamics and further evaluate modeling assumptions.

Table 7

Average Standard Deviation (σ), Total Standard Deviation (σ_T) and Associated 90% Confidence Interval for UBL, DBL, and North Section C.

Layer	Entity	Dataset	σ (g/L)	σ_T (g/L)	90% CI
*UBL	BSC	YSI 556 Conductivity Meter	1.02	7.81	±12.88
	USGS, UGS, HDR	Anton Paar DMA 35 Density Meter			
	DWiR	Atago Master S28α Refractometer			
	BSC	SC	3.97		
	USGS, UGS, HDR	ρ			
	DWiR	$\%S$			
	BSC, USGS, UGS	GSL site 3510, 2565	6.64		
DBL	BSC	YSI 556 Conductivity Meter	1.44	25.66	±42.34

	USGS, UGS, HDR	Anton Paar DMA 35 Density Meter			
	BSC	SC	18.80		
	USGS, UGS, HDR	ρ			
	BSC, USGS, UGS	GSL site 3510, 2565	17.41		
North Section	USGS, UGS, HDR	Anton Paar DMA 35 Density Meter	1.36	14.95	±24.67
		ρ	14.89		

Note. *σ is the average standard deviation from each source of error in the datasets while σ_T is the propagated error within the datasets, calculated from each σ using Eq.(57).

3.4.3 Model Calibration and Validation

Water Surface Elevation

One of the core objectives in calibrating the USU-MBM was to evaluate and refine its ability to predict GSL WSE since the New Breach was opened (Figure 23). WSE outputs during the calibration period for the north section and UBL of the south section generally show good agreement with historical observations (south section RMSE = 0.13 m, north section RMSE = 0.16 m) suggesting that the calibrated model accounts for most ~~V~~ fluxes in the system. Calibration period RMSE for the DBL was 0.22 m (Figure 23c). In general, modeled and observed DBL elevation (and corresponding ~~V~~) followed the same trend; however, the USU-MBM did not capture the abrupt shifts in observed DBL elevation during the calibration period. There is significant uncertainty in the historical DBL WSE time series because the depth to DBL dataset used to calculate historical DBL ~~V~~ had limited spatial and temporal resolution which necessitated interpolation. Given these uncertainties, the accuracy of the predicted trend in DBL ~~V~~ suggests that the ~~V~~ threshold method is valid

for use in partitioning ~~V~~ between the UBL and DBL and no further calibration was necessary

Figure 23

WSE Results for the North Section, UBL and DBL from the Calibration and Validation Simulations

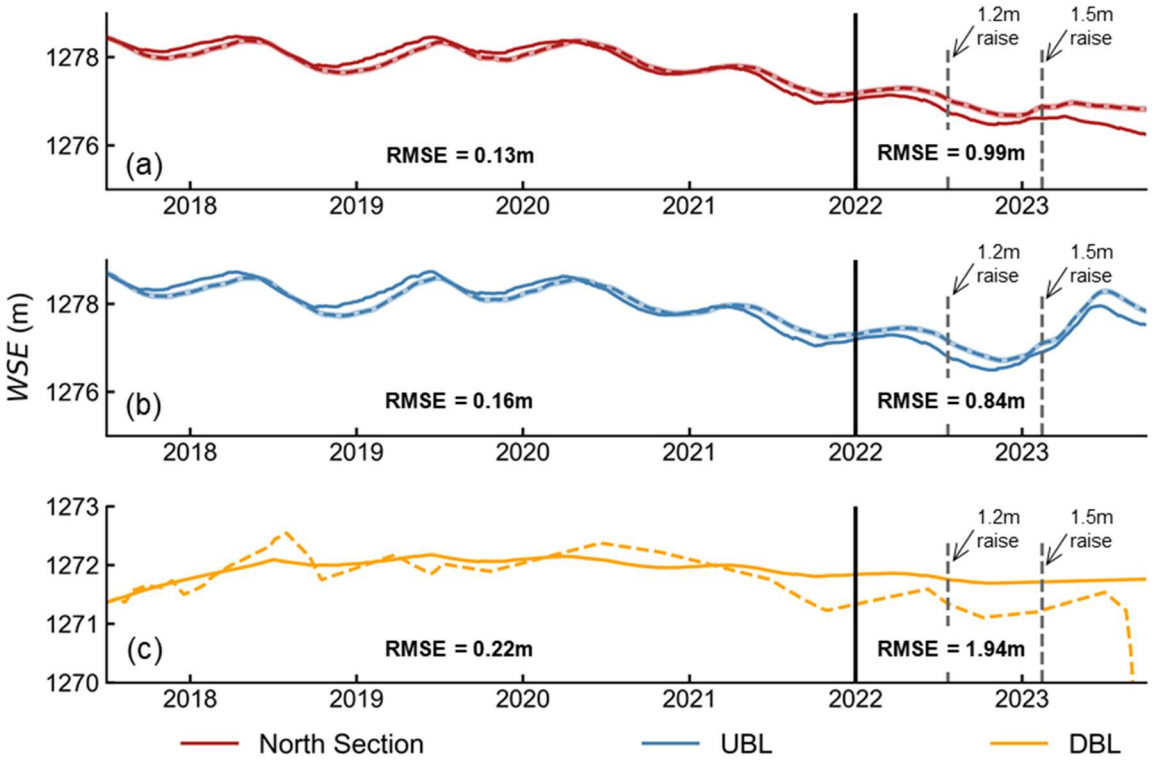

Note. USU-MBM predictions are indicated by the solid lines while calibration/validation data is indicated by the dashed lines surrounded by the calculated 90% confidence intervals (shaded regions). The black vertical line separates the calibration period (left) from the validation period (right) while the dashed gray lines indicate timing of New Breach berm raises.

Another desired aspect of the model is to capture WSE across varied New Breach berm conditions which was evaluated during model validation. During the validation period, the USU-MBM underpredicted both north and south section WSE but overpredicted DBL elevation, primarily during 2023 (Figure 23a, b, c). However, it captured the seasonal trend. This showcases the calibrated model's ability to quantify New Breach exchange flows under a variety of berm geometries and indicates that the model relies on precise WSE predictions to accurately quantify NS flow through the New Breach as demonstrated by the overprediction in DBL elevation. While WSE RMSE values during the validation period were higher than the calibration period, they were influenced by errors propagated from the calibration period and can be attributed to uncertainties in the historical forcing data rather than the model formulation since both north and south section WSE was underpredicted.

Salt Concentration

The second key objective for the USU-MBM was accurate prediction of GSL C, with a priority to the south section as discussed previously. C outputs from the calibration period (Figure 24) showed that UBL and DBL C matched the trend in the calibration data and fell well within the 90% CIs (UBL RMSE = 7 g/L, DBL RMSE = 9 g/L). During the calibration period, predicted C_N followed a seasonal trend aligning with oscillations in V_N while observed C_N remained constant (north section RMSE = 19 g/L). This disparity suggests the USU-MBM does not fully capture seasonal dynamics of north section M, indicated by interannual fluctuations in M_N (Figure 25a, d). While there may be unaccounted mass fluxes within the north section, given the simplifications of the system,

the closeness of fit suggests that the dominant M and $\forall$ fluxes are represented in the USU-MBM and that it is able to replicated C observations within the north section, UBL and DBL across a variety of hydroclimatic conditions.

During validation, the USU-MBM underpredicted M_{ubl} but overpredicted C_{ubl} due to underpredicting WSE (Figure 23b, Figure 24b, Figure 25b). These results indicate that for the USU-MBM, the trend in UBL C is dominated by WSE fluctuations, but the magnitude is determined by M. Conversely, during the validation period C_{dbl} was overpredicted despite overprediction in WSE due to overprediction of M_{dbl} (Figure 23c, Figure 24c, Figure 25c). This suggest that C_{dbl} is mainly driven by mass fluxes. Except for the north section, predicted C values fell within the 90% confidence surrounding the validation data. This exemplifies the model's ability to accurately predict south section C under varied New Breach berm geometries and hydroclimatic conditions and further validates the methods used to partition M and $\forall$ between the UBL and DBL.

Figure 24

Salinity (C) Results for the North Section, UBL and DBL from the Calibration and Validation Simulations

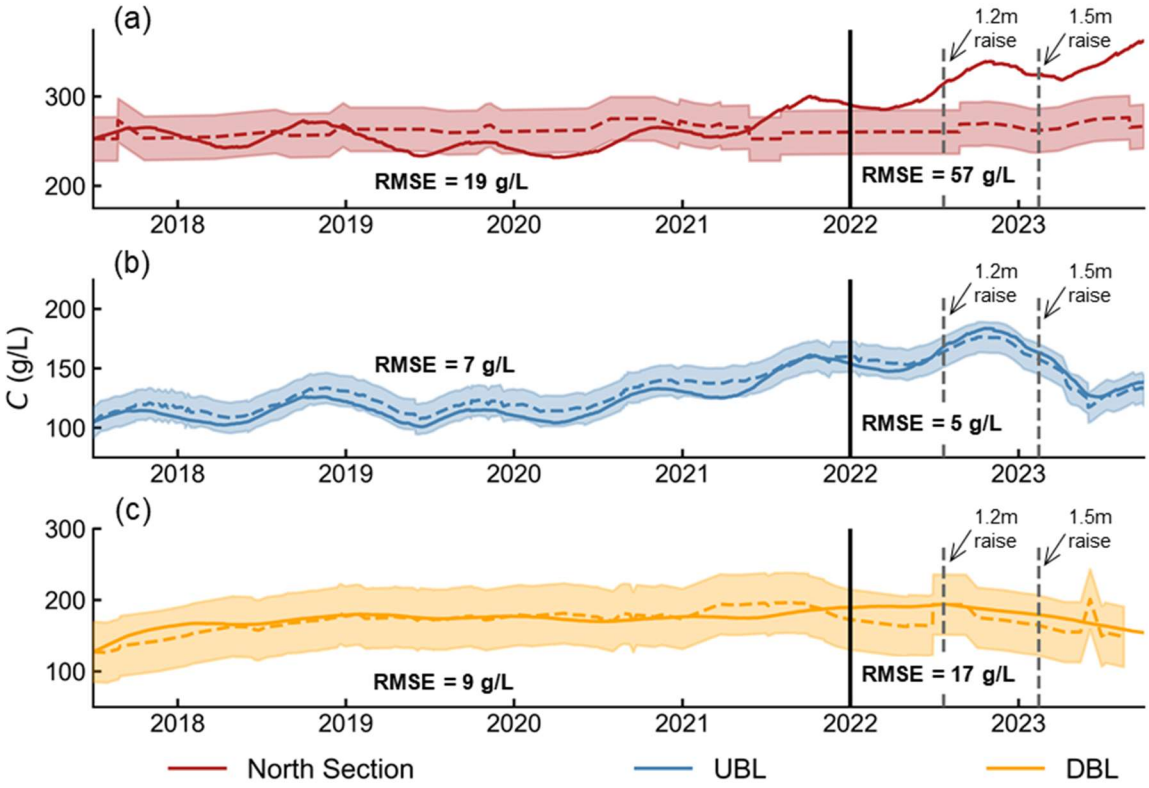

Note. USU-MBM predictions are indicated by the solid lines while calibration/validation data is indicated by the dashed lines surrounded by calculated 90% confidence intervals (shaded regions). The black vertical line separates the calibration period (left) from the validation period (right) while the dashed gray lines indicate timing of New Breach berm raises.

Figure 25

Total Dissolved Salt Mass (M) Results for the North Section, UBL and DBL from the Calibration and Validation Simulations

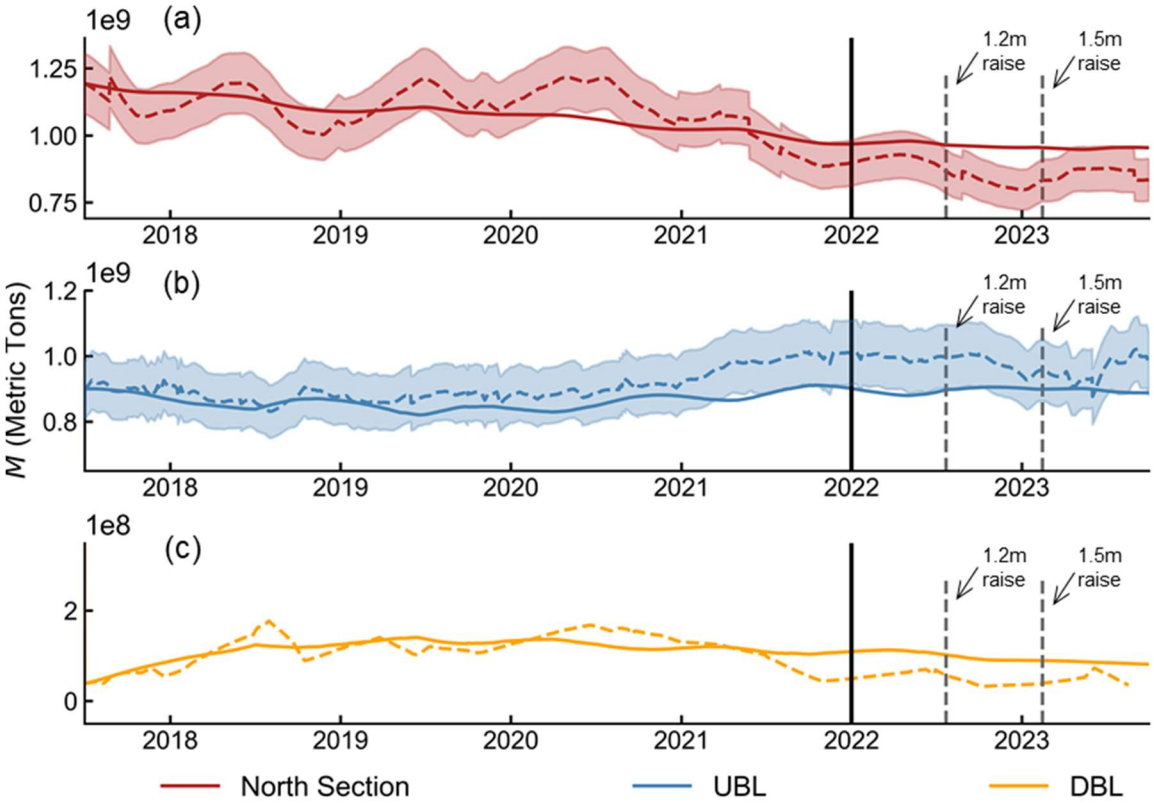

Note. USU-MBM predictions are indicated by the solid lines while calibration/validation data is indicated by the dashed lines surrounded by calculated 90% confidence intervals (shaded regions). The black vertical line separates the calibration period (left) from the validation period (right) while the dashed gray lines indicate timing of New Breach berm raises.

3.4.4 Impacts of Forcing Data Error

The calibrated USU-MBM demonstrated strong performance in predicting historical WSE and C despite uncertainties in the forcing data and estimation methods used

to quantify mass balance terms. The error impact analysis was conducted to explore any additional means to improve model performance and identify management goals for consideration at the GSL. Based on RMSE results, the model was most sensitive to uncertainty in Q_{NS}, Q_{SN} and $Q_{BR,pred}$ (Table 8;Figure 26). It was hypothesized that maximizing salt influx ($+Q_{NS}$, $-Q_{SN}$) to the south section would increase UBL C and minimizing salt influx ($-Q_{NS}$, $+Q_{SN}$) would decrease UBL C. However, both scenarios caused a decrease (Figure 26a). Mass loading to the UBL results from mass transfer across the UBL/DBL interface due to the C gradient while UBL mass export occurs via Q_{SN}. When Q_{SN} is minimized, more M is retained causing C of the UBL to be higher and mass transfer across the layers to be lower. The decrease in M transfer across the layers into the UBL may have offset the mass retention from decreasing Q_{SN} (Figure 26a). This may also explain the observed trend in the isolated Q_{SN} simulation (Figure 26); where increasing Q_{SN} caused a slight increase in UBL C while decreasing Q_{SN} decreased UBL C. When Q_{NS} was isolated (Figure 26c), maximizing Q_{NS} resulted in higher UBL C and minimizing Q_{NS} caused lower UBL C. Increasing M in the DBL triggers more mass transfer to the UBL because it increases the C gradient and vice versa which aligns with the results shown.

Table 8

Error Impact Analysis Results

Variable	Uncertainty	RMSE (g/L)	
		High	Low
Q_{BR}	±68%	27.6	50.5
$Q_{WR,\,FB,\,GD,\,L}$	±5%	1.1	1.1
$C_{WR,\,FB,\,GD}$	±0.001 g/cm^3	0.8	1.2
P_S, P_N	±10%	2.9	3.0

E_S, E_N	±0.5 °C, ±0.3 m/s, ±0.3 hPa	4.4	4.0
Q_{NS}	±85%	8.4	15.2
Q_{SN}	±67%	2.7	7.4
$+Q_{NS}$, $-Q_{SN}$	+85%, -67%	2.8	
$-Q_{NS}$, $+Q_{SN}$	-85%, +67%	14.8	

Note. Ranges of error in GSL mass balance terms used in the error impact analysis are designated as uncertainty. RMSE values are between UBL C from each error simulation and the simulation ran under historical conditions from July 2017 to October 2023.

Figure 26

UBL C Outputs from the Forcing Data Error Analysis

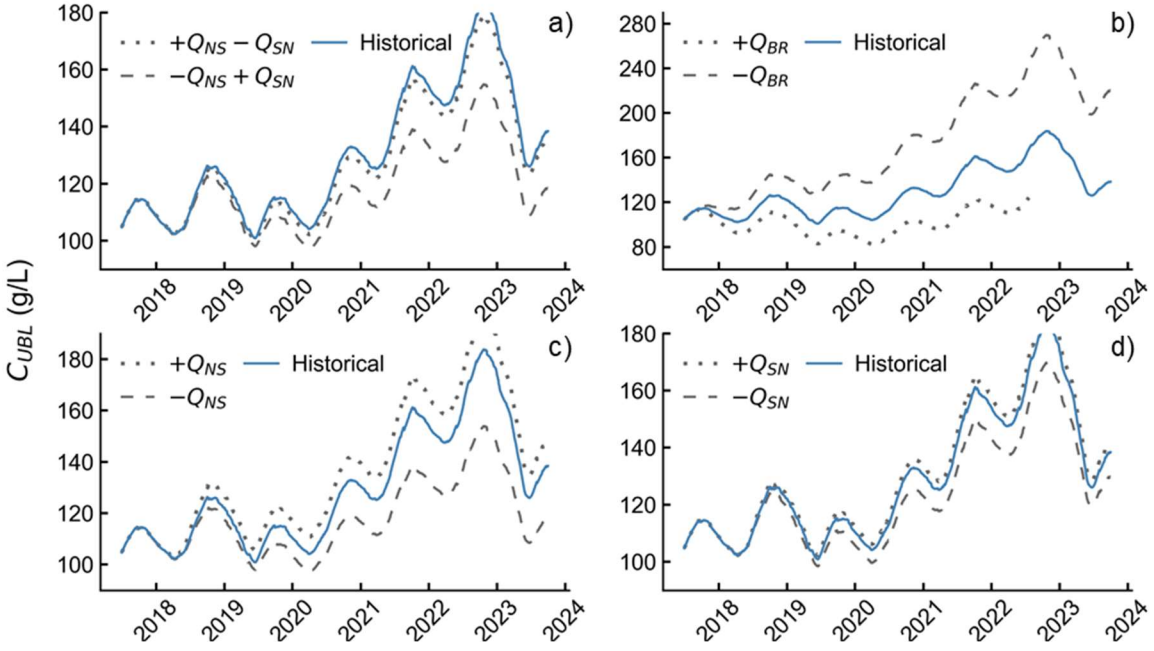

Note. Plot (a) includes results for both New Breach flow directions, plot (b) includes results for Q_{BR}, plot (c) includes results for isolated Q_{NS} (c) and plot (d) for isolated Q_{SN}.

Uncertainty in the rating curves is significant, however UBL C was most sensitive to the BR gage data regression (Figure 26b). Maximizing Q_{BR} caused lower UBL C while minimizing caused higher UBL C. It is also important to note that when Q_{BR} was minimized, south section WSE equalized with the north section. This caused the 1276.2 m Q_{NS} rating curve to produce a value that exceeds what the system can experience which threw an error in the USU-MBM, explaining the lack of (-Q_{BR}) C data after July 21st, 2022.

3.4.5 Management Scenarios

Adaptive management at the GSL has focused primarily on altering the New Breach berm to control UBL C. Results from the management scenarios informs this work by showcasing how berm adaptations can be utilized to effectively manage UBL C and demonstrating the USU-MBM's ability to perform simulations of berm management strategies (Figure 27). C outputs from all four berm conditions (historical, low berm, medium berm, high berm) did not deviate from each other until 2019 when WSE began to decrease due to drought conditions and increased surface water diversions (Figure 23b); indicating that C may be more sensitive to New Breach exchange flows when river Q is lower. After 2020, C did not increase as drastically for the medium berm case compared to the historical and low berm cases because it maximized south section mass export while minimizing mass loading from the north section. Despite cutting off all mass loading from the north section, the high berm case behaved similarly to the medium berm case. These results indicate that blocking Q_{NS} is the most effective use of berm adaptations and that the gain in V from isolating the south section is offset by the retention in M. Further, UBL C from the medium berm case simulation was lower compared to the high berm case

simulation beginning in spring 2023 which shows that keeping the berm at the medium elevation is a productive mechanism for maximizing salt export and minimizing salt import to the south section.

Figure 27

UBL C Outputs from the Historical and Management Scenario Simulations

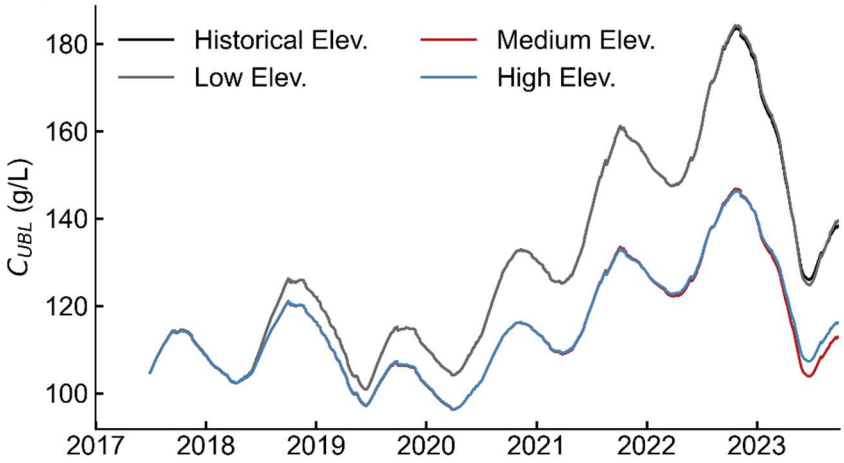

3.5 Discussion

Results from this study demonstrate the validity of the USU-MBM while the error impact analysis highlights future adaptations as understanding of lake processes and hydrologic monitoring evolves. They also exemplify how it can be applied to evaluate future adaptive management decisions.

3.5.1 Model Performance

Water Surface Elevation

Hydrologic observations at the GSL, particularly during the recent drought/flood cycle, have highlighted the connection between C and WSE. Thus, it is important to have

accurate predictions of WSE to make informed, proactive management decisions for the lake to avoid additional negative impacts on GSL ecologic communities and economic production. The USU-MBM adequately predicted WSE of the north section and UBL indicating that it accounted for most water V fluxes in the system. However, it consistently underpredicted WSE starting in 2021 which results from uncertainty in the forcing data including potential, ungauged inflows, uncertainty in groundwater contributions to the lake, and quantity of return flows from mineral extraction activities (Lukens et al., 2024). The error in WSE predictions could also result from uncertainty in the evaporation method or BR gage data correction given the influence error in these estimation methods had on UBL C during the error impact analysis. For the DBL, the RMSE values during the calibration and validation were significant, but it is important to keep in mind that the historical observations of DBL depth used to prepare the calibration data were limited spatially and temporally. For this reason, and the other sources of uncertainty, increased hydrologic monitoring at the GSL and improvement in evaporation estimation methods will be critical for future modeling and management efforts.

Salt Concentration

Brine flies and brine shrimp are dependent on south section C remaining within a healthy range ($100 < C_{ubl} < 160$ g/L). If C_{ubl} falls outside this range, it effects individuals and population growth which in turn affects the water and shore birds who feed on them (Marden, 2020), emphasizing the necessity of accurate predictions of UBL and DBL C. Modeled UBL C was within an appropriate range of uncertainty, but underpredicted C. This is driven by underpredictions in north section M resulting from the USU-MBM's inability

to capture the observed seasonality in M_N. The only M flux into the DBL is Q_{NS}, thus underpredictions in DBL M and C are compounded by uncertainty in the rating curves. Since M transfer between the layers is dependent on the C gradient, underprediction of DBL C and uncertainty in M export from the UBL via Q_{SN}, further contributes to the underprediction of M and C within the south section. Causeway seepage also contributes M to the DBL (Jewell, 2021) but has not been thoroughly investigated and was not accounted for in the USU-MBM which is another reason for underprediction of DBL C and M transfer between the two layers. Currents along the south section lakebed have been observed (Naftz et al., 2014) which can lead to redissolution of precipitated salt and may be another relevant M flux that is not well understand or incorporated into the USU-MBM, further explaining the model's performance.

3.5.2 Management Scenarios

From the management scenario simulations, the berm was found to have the most influence on UBL C by altering mass flux. New Breach Qs were small compared to river Qs, showing that the berm has little effect on total lake ~~V~~; however, New Breach Qs were the largest mass flux in the system. This indicates that if south section ~~V~~ gets too low and C gets too high, the berm should be used to minimize M import to the south section via Q_{NS} and maximize M export via Q_{SN} by maintaining a medium elevation rather than fully isolating the south section. In contrast, the berm may not be useful in increasing south section C. If the berm is lowered, Q_{NS} will be higher, but Q_{SN} will also increase thus the net M in the south section would most likely remain unchanged. The berm can be used as an emergency measure, such as the raise in February 2023, but long-term management of

south section C will require reducing diversion from upstream tributaries to maintain the hydrologic balance of the GSL. Further, sequestering salt in the north section is an appropriate adaptive management strategy, but if too much is exported from the south section, a series of wet years may cause the south section to be too dilute which effects the ecologic productivity of the brine shrimp communities.

3.5.3 Model Utility and Future Work

The USU-MBM was successfully formulated to predict GSL C and WSE, quantify New Breach exchange flows under varied berm elevations, and predict south section chemical stratification. However, it is important to keep model assumptions and performance in mind when using it to inform lake management. The USU-MBM is particularly useful in predicting long term C and WSE of the UBL and WSE of the north section. In the future, increased monitoring of GSL inflows including continuous monitoring of flow through the BR Bay Bridge may improve these estimates given the model's sensitivity to uncertainty in Q_{BR} and that changes in south section C are mainly driven by WSE fluctuations. The USU-MBM did not incorporate a process-based method to partition M and V between the UBL and DBL. Thus, these outputs could be improved by development of specific wind mixing equations for hypersaline environments.

Adaptive management strategies can also be developed using the USU-MBM , given its ability to predict New Breach exchange flows. Like the model application performed within this study, the USU-MBM can be used to explore the influence of varying the berm elevation and to determine the optimal timing for berm alterations. Since the USU-MBM failed to capture north section M dynamics, it should not be used to predict

north section C until this process is better understood. If this were achieved, it would further improve estimates of UBL and DBL C which are of primary interest to lake managers. With the current USU-MBM formulation, future lake conditions cannot be evaluated because it utilizes historical time series for the forcing data. However, since the USU-MBM is open access, it can easily be paired with climate and streamflow predictive models to evaluate the future health of the lake.

3.6 Conclusion

The primary purpose of this study was to inform adaptive management of the GSL by developing an open access, process-based mass balance model of the Great Salt Lake. Historical observations of salinity informed a simple model framework that includes control volumes for the two segregated lake sections, with the south section further segregated into upper and lower brine layers. Key V and M fluxes are tracked within the model in addition to bi-directional flow exchange between the control volumes and salt mass and water volume partitioning between the south section layers. With this simple formulation, the USU-MBM captured C and WSE in response to historic inputs of streamflow, climate, and adaptive management actions.

Based on results from this study, it was concluded that a two-layer model for the south section is necessary to accurately predict UBL C, the magnitude of which has implications for the health of the ecologic communities. USU-MBM performance regarding WSE indicated the need for increased hydrologic monitoring at the Great Salt Lake, mainly continuous monitoring of Bear River Bay Bridge Qs, increased monitoring

of groundwater contribution, and evaluation of E estimates off hypersaline water bodies. Temperature effects on north section M and contribution of salt mass to the south section via causeway seepage should be evaluated in the future to expand usage of the USU-MBM, given that the model underpredicted M for both sections. A key feature of the USU-MBM is its ability to predict New Breach exchange flows given various berm elevations, the primary focus of adaptive management actions at the GSL. Based on USU-MBM application, it was concluded that using the berm to minimize mass import to the south section and maximizing mass export to the north section is the most productive mechanism for decreasing C within the upper brine layer. Further, coupling the USU-MBM with predictive climate and streamflow models will enable forecasting GSL conditions under varying climate regimes.

It has been shown that the USU-MBM developed herein is a tool that can quantitatively evaluate adaptive management strategies. Application of this tool will facilitate informed lake management decisions that aim to balance human, ecologic, and economic needs as conditions within and around the lake continue to change.

4 CONCLUSION

Since 1847, the Great Salt Lake has lost more than 48% of its volume (Wurtsbaugh, 2016) which has caused irreversible damage to its diverse ecologic communities (Barnes and Wurtsbaugh, 2015), hindered economic productivity (Potential Cost of Declining Great Salt Lake, 2019), and decreased air quality affecting human health (Perry, 2019). Recent lake management efforts have focused on optimizing water use within the GSL watershed and adaptively managing salinity levels by utilizing the submerged berm at the New Breach. To inform these decisions, it is crucial to have data at appropriate spatial and temporal scales to increase understanding of the system and evaluate the lake's response to management actions. In addition, modeling tools are key to determining the effect of proposed solutions under a variety of future conditions. Given the historic low lake level recorded in November 2022 and the implications of lake desiccation, the objective of this study was to aid management efforts at the lake by compiling and evaluating available hydroclimatic data and developing a model that accurately predicts lake level and salinity in response to varying berm elevations and hydroclimatic conditions.

Outcomes of Chapter 1 included: documentation of available inflow, climate and water quality data at the lake, a method to combine open water salinity data from various entities and proxy measurements, provision of representative salinity time series for the north and south section of the GSL, and determination of key drivers of salinity within the south section. The main contribution from Chapter 2 was creation, documentation and application of an open source, process-based mass balance model of the lake that is capable

of accurately quantifying lake level and salinity response to historical conditions and management actions.

Results from both chapters highlight the need for increased hydrologic monitoring at the GSL. The correlation analysis performed in Chapter 1 between salinity and mass balance terms revealed that variation in UBL salinity is most heavily influenced by the balance between river inflows, primarily from the Bear River, and evaporation. This was confirmed by the modeling effort in Chapter 2. South section total dissolved salt mass remained fairly constant at the time scale evaluated, thus fluctuations in UBL salinity outputs were attributed to seasonality in lake elevation. The GSL mass balance model utilized all available inflow data and the best available evaporation methods, yet underpredicted north and south section WSE indicating a gap in inflow data and a limited understanding of evaporation. To better predict salinity/WSE and manage the lake in the short-term, there is a clear need for improved methods to estimate evaporation off the GSL and more precise monitoring of the Bear River inflows and groundwater contribution to the lake.

Based on mass fluxes calculated in the model, salt mass loading to the GSL and exchange between the sections is small relative to the total dissolved salt mass already accumulated in the lake, thus monitoring open water salinity and accurately predicting New Breach exchange flows becomes crucial for accurate, long-term predictions of salinity. Analysis of available salinity data in Chapter 1 revealed the need to adopt standard operating procedures and sampling locations to monitor open water salinity. This would aid combination of data from different entities that monitor the lake and allow for

development of more accurate and representative salinity time series. In addition, model outputs of north section salinity indicate missing salt mass fluxes which were attributed to seasonal mass increases and decreases in the north section likely resulting from temperature shifts and wave action. Improved understanding of this process and open water salinity monitoring would aid evaluation of GSL models and short-term and long-term changes in total salt mass in response to management actions.

Results from Chapter 2 demonstrate that the GSL mass balance model is a valid tool for informing management decisions. Model outputs were within the range of uncertainty associated with the calibration data and confirm that the model can predict WSE and salinity of the south section in response to berm alterations. Based on model simulations performed with varying berm heights and historical forcing data, the New Breach berm was determined to be a productive, short-term tool. Raising the berm minimizes south section salinity by decreasing mass loading via north to south exchange and maximizes south section dilution by decreasing south to north exchange. However, long term management of the lake will require increasing inflows to the lake. Finally, the current model formulation has the capacity to be paired with forecasts of streamflow and climate. This would allow for more detailed evaluation of berm management alternatives and development of a comprehensive adaptive management plan for the GSL.

Development of adaptive management strategies at the GSL has previously been limited due to uncertainty in hydrologic monitoring and an inability to accurately predict WSE and salinity in response to management actions. The research conducted herein improves upon current knowledge by highlighting key gaps in hydrologic monitoring and

understanding of lake processes and provides a novel model of the lake for use in evaluating management alternatives. As conditions at the lake continue to evolve, this tool can help lake managers make informed decisions on how to best preserve the GSL while balancing human, ecologic and economic needs.

5 ENGINEERING SIGNIFICANCE

Mass balance models are significant in the field of engineering, primarily water resource management. Population growth, urbanization and a changing climate have decreased water quantity and quality of water resources within the Western United States that are already under duress. Sustainable and effective management of these critical resources requires an understanding of the implications of water and land use changes and an evaluation of different management strategies to identify policies that help balance human and ecological needs. Mass balance models facilitate this evaluation as they provide a quantitative framework for understanding how changes in policy affect water systems such as river networks, lakes, reservoirs, aquifers, and groundwater. They can be utilized to simulate policy scenarios impacting water allocation and conservation, project future water demand, or evaluate environmental impacts among other uses.

The model developed herein for the GSL is a prime example of the efficacy of mass balance models. It allows GSL managers to evaluate the water surface elevation and salinity of the GSL in response to streamflow, climate, and changes to internal water and cycling resulting from alterations to the New Breach berm. If the USU-MBM were paired with streamflow and climate predictive models, it would facilitate quantification of future lake conditions in response to hypothetical water and land use changes. The USU-MBM can pinpoint total inflow volume required to maintain the health of the lake which helps establish a maximum threshold for consumptive water use. It further allows for identification of effective New Breach berm adaptive management strategies that can help maximize resiliency of the GSL in the face of altered flow regimes and climatic conditions.

While the USU-MBM was developed specifically for the GSL, the model framework can be applied to terminal lakes worldwide. Its methodology allows for quantification of water levels and the concentration and potential chemical stratification of conservative constituents and can easily be adapted to the specific limnological characteristics of other closed basin lakes.

REFERENCES

AghaKouchak, A., Norouzi, H., Madani, K., Mirchi, A., Azarderakhsh, M., Nazemi, A., Nasrollahi, N., Farahmand, A., Mehran, A., and Hasanzadeh, E. (2015). Aral Sea syndrome desiccates Lake Urmia: Call for action. *Journal of Great Lakes Research*, *41*(1), 307–311. https://doi.org/10.1016/j.jglr.2014.12.007

Allen, R. G., L. S. Pereira, D. Raes, and M. Smith. (1998). Crop evapotranspiration guidelines for computing crop water requirements. *FAO Irrigation and drainage* (56): 328.

Anati, D. A. (1999). The salinity of hypersaline brines: Concepts and misconceptions. *International Journal of Salt Lake Research*, *8*(1), 55–70. https://doi.org/10.1007/BF02442137

Assessment of Potential Costs of Declining Water Levels in Great Salt Lake. (2019). ECONorthwest. Retrieved from https://documents.deq.utah.gov/water-quality/standards-technical-services/great-salt-lake-advisory-council/activities/DWQ-2019-012913.pdf

Barnes, B. D., and Wurtsbaugh, W. A. (2015). The effects of salinity on plankton and benthic communities in the Great Salt Lake, Utah, USA: A microcosm experiment. *Canadian Journal of Fisheries and Aquatic Sciences*, *72*(6), 807–817. https://doi.org/10.1139/cjfas-2014-0396

Baxter, B. K., and Butler, J. K. (2020). Climate Change and Great Salt Lake. In B. K. Baxter and J. K. Butler (Eds.), *Great Salt Lake Biology* (pp. 23–52). Springer International Publishing. https://doi.org/10.1007/978-3-030-40352-2_2

Belovsky, G. E., Stephens, D., Perschon, C., Birdsey, P., Paul, D., Naftz, D., Baskin, R., Larson, C., Mellison, C., Luft, J., Mosley, R., Mahon, H., Van Leeuwen, J., and Allen, D. V. (2011). The Great Salt Lake Ecosystem (Utah, USA): Long term data and a structural equation approach. *Ecosphere*, *2*(3), art33. https://doi.org/10.1890/ES10-00091.1

Berthouex, P. M., and Brown, L. C. (2002). *Statistics for Environmental Engineers*.

Bioeconomics, Inc. (2012). *Economic significance of the Great Salt Lake to the State of Utah.* Prepared for the State of Utah Great Salt Lake Advisory Council, Salt Lake City, Uta. Retrieved from https://documents.deq.utah.gov/water-quality/standards-technical-services/great-salt-lake-advisory-council/activities/DWQ-2012-006864.pdf

Borlina, C. S., and Rennó, N. O. (2017). The Impact of a Severe Drought on Dust Lifting in California's Owens Lake Area. *Scientific Reports*, *7*(1), 1784. https://doi.org/10.1038/s41598-017-01829-7

Brown, P. D., Bosteels, T., and Marden, B. T. (2023). Salt load transfer and changing salinities across a new causeway breach in Great Salt Lake: Implications for adaptive management. *Lakes and Reservoirs: Science, Policy and Management for Sustainable Use*, *28*(1). https://doi.org/10.1111/lre.12421

Brown, P. M. B. L. C., and Hambley, D. F. (2002). Statistics for Environmental Engineers. *Environmental and Engineering Geoscience*, *8*(3), 244–245. https://doi.org/10.2113/8.3.244

Chapra, S.C. (1997) Surface Water Quality Modeling. McGraw-Hill Publisher, New York.

Chapra, and Martin. (2004). *Lake2K: A Modeling Framework for Simulating Lake Water Quality (Version 1.2)*.

Daly, C., Halbleib, M., Smith, J. I., Gibson, W. P., Doggett, M. K., Taylor, G. H., Curtis, J., and Pasteris, P. P. (2008). Physiographically sensitive mapping of climatological temperature and precipitation across the conterminous United States. *International Journal of Climatology*, *28*(15), 2031–2064. https://doi.org/10.1002/joc.1688

Donnelly, J. P., King, S. L., Silverman, N. L., Collins, D. P., Carrera-Gonzalez, E. M., Lafón-Terrazas, A., and Moore, J. N. (2020). Climate and human water use diminish wetland networks supporting continental waterbird migration. *Global Change Biology*, *26*(4), 2042–2059. https://doi.org/10.1111/gcb.15010

Dunn, D. (2024a). Great Salt Lake Salinity, Climate, and Inflow Data, HydroShare

Dunn, D. (2024b). Great Salt Lake Mass Balance Model Data Collection, HydroShare, Dutta, S., Crookston, B.M., Dunn, D., Larsen, E., and Talukdar, M.I.H. (2024). *Predicting Temporal Evolution of Salt Mass Within the Great Salt Lake under Adaptive Berm Management and Changing Lake Conditions* (Report No. 4747). Utah Water Research Lab, Utah State University.

Ford, D. E., and Johnson, L. S. (1986). *An assessment of reservoir mixing processes. Technical report E-86-7*. Vicksburg, MS: Ford, Thornton, Norton and Associates, Ltd. (for the U.S. Army Engineer Waterways Experiment Station). Retrieved from https://usace.contentdm.oclc.org/digital/collection/p266001coll1/id/2728/

Great Salt Lake Integrated Water Resources Management Model (GSLIM). (2019). [Evaluation]. Jacobs engineering. Retrieved from https://documents.deq.utah.gov/water-quality/standards-technical-services/great-salt-lake-advisory-council/DWQ-2022-028692.pdf

Great Salt Lake Salinity Advisory Committee. (2020a). *Round Robin of Methods to Estimate the Salinity of Great Salt Lake Waters*. Utah Geological Survey. https://doi.org/10.34191/OFR-727

Great Salt Lake Salinity Advisory Committee. (2020b). *Standard Operating Procedure—Great Salt Lake Water Density Measurement and Salinity Calculation*. Utah Geological Survey. https://doi.org/10.34191/OFR-728

Great Salt Lake Salinity Advisory Committee. (2021). *Influence of Salinity on the Resources and Uses of Great Salt Lake*. Utah Geological Survey. https://doi.org/10.34191/OFR-736

Great Salt Lake Strike Team. (2023). *Great Salt Lake Policy Assessment: A Synthesized Resource Document for the 2023 General Legislative Session*. Retrieved from https://gardner.utah.edu/wp-content/uploads/GSL-Assessment-Feb2023.pdf?x71849

Great Salt Lake Strike Team. (2024). *Great Salt Lake Data and Insights Summary: A Synthesized Resource Document for the 2024 General Legislative Session*. Retrieved from https://d36oiwf74r1rap.cloudfront.net/wp-content/uploads/2024/01/GSL-Insights-Summary-Jan2024.pdf

Gwynn, W., and Sturm, P. (1987). *Effects of Breaching the GSL Causeway, Great Salt Lake, Utah—Physical and Chemical Changes August 1, 1984-July, 1986*. Utah

Geological and Mineral Survey. Retrieved from https://ugspub.nr.utah.gov/publications/water_resources_bulletins/WRB-25.pdf

Hassani, A., Azapagic, A., D'Odorico, P., Keshmiri, A., and Shokri, N. (2020). Desiccation crisis of saline lakes: A new decision-support framework for building resilience to climate change. *Science of The Total Environment*, *703*, 134718. https://doi.org/10.1016/j.scitotenv.2019.134718

Helsel, D. R., Hirsch, R. M., Ryberg, K. R., Archfield, S. A., & Gilroy, E. J. (2020). *Statistical methods in water resources: U.S. Geological Survey Techniques and Methods, book 4, chapter A3, 458 p.* [Supersedes USGS Techniques of Water-Resources Investigations, book 4, chapter A3, version 1.1]. https://doi.org/10.3133/tm4a3

Hoffman, J. D. (2001). *Numerical methods for engineers and scientists* (2nd ed.). Marcel Dekker, Inc. Retrieved from http://freeit.free.fr/Finite%20Element/Hoffman,_Numerical_Methods_for_Engineers&Scientists,2001.pdf

Holley, E., R., M. ASCE, and K. M. Waddell. (1976). "Stratified Flow in Great Salt Lake Culvert." Journal of Hydraulics Division, 17. https://doi.org/10.1061/JYCEAJ.000459

Horsburgh, J. S., A. S. Jones, S. S. Black, T. O. Hodson (2022). USGS dataretrieval Python Package Usage Examples, HydroShare, http://www.hydroshare.org/resource/c97c32ecf59b4dff90ef013030c54264

Huntington, J., Hegewisch, K., Daudert, B., Morton, C., Abatzoglou, J., McEvoy, D., and T., Erickson. (2017). Climate Engine: Cloud Computing of Climate and Remote Sensing Data for Advanced Natural Resource Monitoring and Process Understanding. Bulletin of the American Meteorological Society, http://journals.ametsoc.org/doi/abs/10.1175/BAMS-D-15-00324.1

Jagniecki, E., Rupke, A., Kirby, S., and nkenbrandt, P. I. (2021). *Salt Crust, Brine, and Marginal Groundwater of Great Salt Lake's North Arm (2019 To 2021)*. Utah Geological Survey. https://doi.org/10.34191/RI-283

Jewell, P. W. (2021). Historic low stand of Great Salt Lake, Utah: I: Mass balance model and origin of the deep brine layer. *SN Applied Sciences*, *3*(8), 757. https://doi.org/10.1007/s42452-021-04691-5

Larsen, E. (2024). Rapid Prediction of Buoyancy-Driven Exchange Flows at the Great Salt Lake: ML Models and a 1D Shallow water approach. Utah State University.

Levesque, V.A., Oberg, K.A. (2012). Computing discharge using the index velocity method: U.S. Geological Survey Techniques and Methods 3–A23, 148 p. Retrieved from http://pubs.usgs.gov/tm/3a23

Lindsay, et al. (2019). Effects of salinity on microbialite-associated production in Great Salt Lake Utah. *Ecology Society of America*, *100*(3). https://doi.org/10.1002/ecy.2611

Loving, B. L., Waddell, K. M., Miller, C. W., Utah. Division Of Forestry, F. A. S. L. & Tooele County. (2000) *Water and salt balance of Great Salt Lake, Utah, and simulation of water and salt movement through the causeway, -98*. [Salt Lake City,

Utah: U.S. Dept. of the Interior, U.S. Geological Survey ; Denver, CO: Branch of Information Services distributor] [Image] Retrieved from the Library of Congress, https://www.loc.gov/item/2001337137/.

Lukens, E., E. K. Turney, S. Null, B. Neilson (2024). Measurement and Infrastructure Gap Analysis in Utah's Great Salt Lake Basin, HydroShare, https://doi.org/10.4211/hs.8bf055dbe78b46d184cc7a4bb53931c7

Madison, R. J. (1970). Effects of a Causeway on the Chemistry of the Brine in Great Salt Lake Utah. *Water Resources Bulletin, 14.* Retrieved from https://ugspub.nr.utah.gov/publications/water_resources_bulletins/WRB-14.pdf

Marden, B., Brown, P., and Bosteels, T. (2020). Great Salt Lake Artemia: Ecosystem Functions and Services with a Global Reach. In B. K. Baxter and J. K. Butler (Eds.), *Great Salt Lake Biology* (pp. 175–237). Springer International Publishing. https://doi.org/10.1007/978-3-030-40352-2_7

Merck, M. F., and Tarboton, D. G. (2023). The Salinity of the Great Salt Lake and Its Deep Brine Layer. *Water*, *15*(8), 1488. https://doi.org/10.3390/w15081488

Micklin, P. P. (1988). Desiccation of the Aral Sea: A water management disaster in the Soviet Union. *Science, 241*(4870), 1170-1176. https://doi.org/10.1126/science.241.4870.1170

Mohammed, I. N. (2006). *Modeling the Great Salt Lake*. Utah State University.

Mohammed, I. N., and Tarboton, D. G. (2012). An examination of the sensitivity of the Great Salt Lake to changes in inputs: GREAT SALT LAKE SENSITIVITY INDEX. *Water Resources Research*, *48*(11). https://doi.org/10.1029/2012WR011908

Munk, W., and Anderson, E. (1948). *Notes on a Theory of the Thermocline*. Journal of Marine Research.

Naftz, D. L., Millero, F. J., Jones, B. F., and Reed Green, W. (2011). An Equation of State for Hypersaline Water in Great Salt Lake, Utah, USA. *Aquatic Geochemistry*, *17*(6), 809–820. https://doi.org/10.1007/s10498-011-9138-z

Naftz, D. L., Carling, G. T., Angeroth, C., Freeman, M., Rowland, R., and Pazmiño, E. (2014). Density-Stratified Flow Events in Great Salt Lake, Utah, USA: Implications for Mercury and Salinity Cycling. *Aquatic Geochemistry*, *20*(6), 547–571. https://doi.org/10.1007/s10498-014-9237-8

Null, et al. (2013).

C*an the causeway in the Great Salt Lake be used to manage salinity? Friends of Gre at Salt Lake Newsletter Vol 19 No. 1 and 2: 14-15*. Retrieved from http://works.bepress.com/wayne_wurtsbaugh/143/

Null S.E., Wurtsbaugh W.A. (2020) Water Development, Consumptive Water Uses, and Great Salt Lake. In: Baxter B., Butler J. (eds) Great Salt Lake Biology. Springer, Cham. https://doi.org/10.1007/978-3-030-40352-2

Oberg, K., Morlock, S., and Caldwell, W. (2005). *Quality Assurance Plan for Discharge Measurements Using Acoustic Doppler Current Profilers*. U.S. Geologic Survey; Scientific Investigations Report 2005-5183. Retrieved from https://pubs.usgs.gov/sir/2005/5183/SIR_2005-5183.pdf

Otto, S. P. (2018). Adaptation, speciation and extinction in the Anthropocene. *Proceedings of the Royal Society B: Biological Sciences*, *285*(1891), 2018-2047. https://doi.org/10.1098/rspb.2018.2047

Perry, K. D. , Crosman, E. T. , & Hoch, S. W. (2019). Results of the Great Salt Lake Dust Plume Study (2016–2018) (Tech. Rep.). Department of Atmospheric Sciences, University of Utah. Retrieved from https://d1bbnjcim4wtri.cloudfront.net/wp-content/uploads/2019/12/10101816/GSL_Dust_Plumes_Final_Report_Complete_Document.pdf

Rasmussen, M.T., Dutta, S., Neilson, B.T., & Crookston, B.M. (2021). CFD Model of the Density-Driven Bidirectional Flows through the West Crack Breach in the Great Salt Lake Causeway. *Water*.

Rasmussen, M. (2022). *Using Computational Fluid Dynamics to Predict Flow Through the West Crack Breach of the Great Salt Lake Railroad Causeway*. Utah State University.Rasmussen, M.T., Dutta, S., Neilson, B.T., & Crookston, B.M. (2021). CFD Model of the Density-Driven Bidirectional Flows through the West Crack Breach in the Great Salt Lake Causeway. *Water*.

Schemel, L. E. (2001). Simplified conversions between specific conductance and salinity units for use with data from monitoring stations. Interagency Ecological Program Newsletter, 14(1), 17–18. USGS Publications Warehouse. Retrieved from https://pubs.usgs.gov/publication/70174311

Shuttleworth, W. J.. (1993). Evaporation. In D. R. Maidment (Ed.), *Handbook of hydrology* (1st ed., pp. 4.1-4.47). McGraw Hill. Spieweck F, Bettin H (1992).

Review: solid and liquid density determination. Technisches Messen 59:285–292. https://doi.org/10.1524/teme.1992.59.78.285

Spieweck F, Bettin H (1992). Review: solid and liquid density determination. Technisches Messen 59:285–292. https://doi.org/10.1524/teme.1992.59.78.285

Sundaram, T. R., and Rehm, R. G. (1973). The seasonal thermal structure of deep temperate lakes. *Tellus*, *25*(2), 157–168. https://doi.org/10.1111/j.2153-3490.1973.tb01602.x

Tarboton, D. (2024). Collection of Great Salt Lake Data, HydroShare, http://www.hydroshare.org/resource/b6c4fcad40c64c4cb4dd7d4a25d0db6e

Tarboton, D. (2024). Collection of Great Salt Lake Data, HydroShare, http://www.hydroshare.org/resource/b6c4fcad40c64c4cb4dd7d4a25d0db6eToppi ng, J. (1972). *Errors of observation and their treatment* (4th ed.). London, UK: Chapman and Hall. Retrieved from https://www.scribd.com/document/56353608/Errors-and-Treatment-Topping-1972

Turnipseed, D. P., & Sauer, V. B. (2010). Discharge measurements at gaging stations. U.S. Geological Survey Techniques and Methods book 3, chap. A8, 87 p. Retrieved from https://pubs.usgs.gov/tm/tm3-a8/tm3a8.pdf

University of Utah, Department of Atmospheric Science. (n.d.). Hatut Station Metadata Page. MESOWEST. Retrieved June 7, 2024, from https://mesowest.utah.edu/cgi-bin/droman/station_total.cgi?stn=HATUT and unit=0

U.S. Geological Survey (2002). Processing of water samples (ver. 2.0): U.S. Geological Survey Techniques of Water-Resources Investigations, book 9, chap. A4, accessed Aug 1, 2022, from http://pubs.water.usgs.gov/twri9A. https://doi.org/10.3133/twri09A5

U.S. Geological Survey. (2023). National Water Information System data available on the World Wide Web (USGS Water Data for the Nation) [Data set]. U.S. Geological Survey. Retrieved October 10, 2023, from http://waterdata.usgs.gov/nwis/2023

Utah Department of Water Quality. (2022). *Union Pacific Railroad Great Salt Lake Permanent East Culvert Closure and Bridge construction Project*. Retrieved from https://documents.deq.utah.gov/water-quality/facilities/401-wq-cert/DWQ-2022-001884.pdf

Utah Geological Survey (2020). Great Salt Lake brine chemistry database: Online, https://geology.utah.gov/docs/xls/GSL_brine_chem_db.xlsx.

Utah State University -. "Utah Climate Center." *USU Climate Center*, climate.usu.edu/. Accessed 24 Jan. 2024.

Vanderplas, Jacob T. *Python Data Science Handbook: Tools and Techniques for Developers*. O'Reilly, 2016. Retrieved from https://jakevdp.github.io/PythonDataScienceHandbook/

Waddell, K. M., and Fields, F. K. (1977). *Model for Evaluating the Effects of Dikes on the Water and Salt Balance of Great Salt Lake Utah*. Retrieved from https://ugspub.nr.utah.gov/publications/water_resources_bulletins/WRB-21.pdf

Wang, S.-Y., Gillies, R. R., Jin, J., and Hipps, L. E. (2010). Coherence between the Great Salt Lake Level and the Pacific Quasi-Decadal Oscillation. *Journal of Climate*, *23*(8), 2161–2177. https://doi.org/10.1175/2009JCLI2979.1

White, J. S., Null, S. E., and Tarboton, D. G. (2015). How Do Changes to the Railroad Causeway in Utah's Great Salt Lake Affect Water and Salt Flow? *PLOS ONE*, *10*(12), e0144111. https://doi.org/10.1371/journal.pone.0144111

Williams, W. D. (2002). Environmental threats to salt lakes and the likely status of inland saline ecosystems in 2025. *Environmental Conservation*, *29*(2), 154–167. https://doi.org/10.1017/S0376892902000103

Williams, A. P., Cook, E. R., Smerdon, J. E., Cook, B. I., Abatzoglou, J. T., Bolles, K., Baek, S. H., Badger, A. M., and Livneh, B. (2020). Large contribution from anthropogenic warming to an emerging North American megadrought. *Science*, *368*(6488), 314–318. https://doi.org/10.1126/science.aaz9600

Wold, S. R., Thomas, B. E., and Waddell, K. M. (1997). *Water and salt balance of Great Salt Lake, Utah, and simulation of water and salt movement through the causeway* (Open-File Report 95–428; p. 76). Retrieved from https://pubs.usgs.gov/of/1995/0428/report.pdf

Wurtsbaugh, W. A. (2014). Management of the Great Salt Lake Ecosystem: Water, Economic Values and Competing Interests. *Watershed Sciences Faculty Publications*, Paper 594. Retrieved from https://digitalcommons.usu.edu/wats_facpub/594

Wurtsbaugh, W. A., and Jones, E. F. (2012). The Great Salt Lake's Deep Brine Layer and Its Importance for Mercury Bioaccumulation in Brine Shrimp (*Artemia franciscana*). *Watershed Sciences Faculty Publications*, Paper 551. Retrieved from https://digitalcommons.usu.edu/wats_facpub/551

Wurtsbaugh, W. A., Miller, C., Null, S. E., DeRose, R. J., Wilcock, P., Hahnenberger, M., Howe, F., and Moore, J. (2017). Decline of the world's saline lakes. *Nature Geoscience*, *10*(11), 816–821. https://doi.org/10.1038/ngeo3052

Yang, S., Johnson, W. P., Black, F. J., Rowland, R., Rumsey, C., and Piskadlo, A. (2020). Response of density stratification, aquatic chemistry, and methylmercury to engineered and hydrologic forcings in an endorheic lake (Great Salt Lake, U.S.A.). *Limnology and Oceanography*, *65*(5), 915–926. https://doi.org/10.1002/lno.11358

APPENDICES

Appendix A. USU UWRL EQL Experiment Data

Figure A1

Density, ρ, and Specific Conductance, SC, Data from the Repeat Measurements Performed in the USU UWRL EQL Experiment

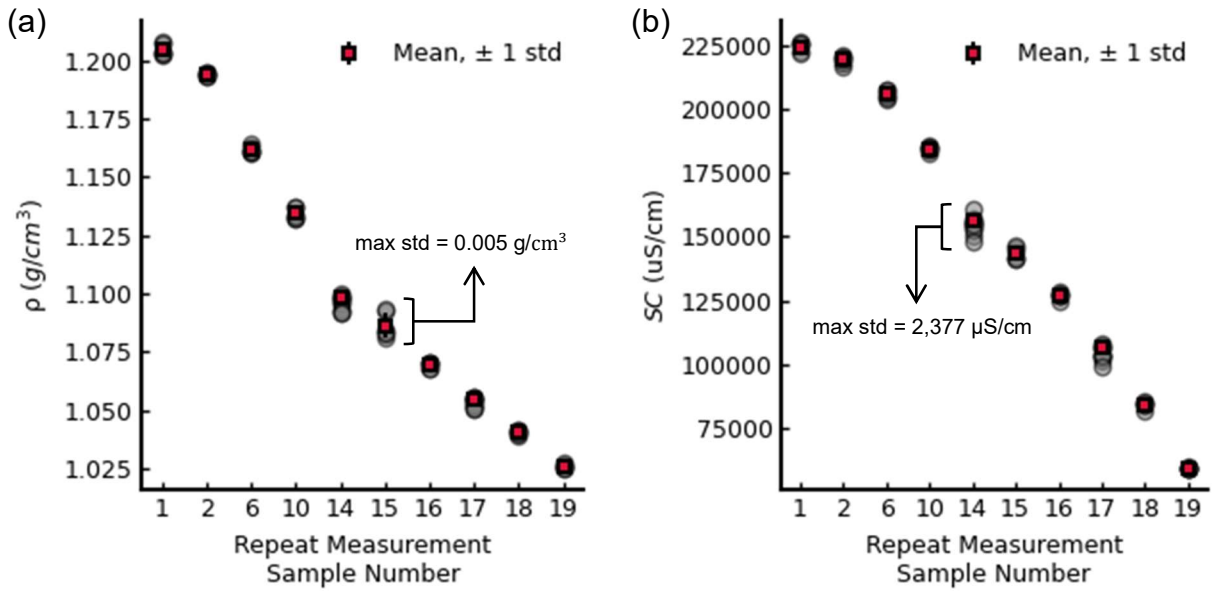

Note. Samples were prepared to cover a range of SC and ρ. Repeat measurements were performed on samples 1, 2, 6, 10, 14-19.

Table A1

Average North and South Section Ion Composition in Percent Weight

Site	Section	Period	Na % WT	Mg % WT	K % WT	Ca % WT	Cl % WT	SO4 % WT
AIS	S	Mar 2017 – Aug 2020	30.29	3.52	2.19	0.17	56.28	7.54
AS2	S	May 2017 - Sep 2020	31.35	3.62	2.23	0.17	55.35	7.28
AC3	S	May 2017 - Sep 2020	31.75	3.62	2.27	0.17	54.89	7.30
FB2	S	Aug 2017 - Sep 2020	31.93	3.57	2.21	0.18	54.83	7.28
RT4	S	May 2017 - Sep2020	31.75	3.55	2.21	0.18	54.93	7.39

		south section average	31.42	3.58	2.22	0.17	55.26	7.36
SJ-1	N	Mar 2017 - Sep 2020	29.02	4.17	2.62	0.10	56.80	7.28
LVG 4	N	Aug 2017 - Sep 2020	30.47	3.92	2.37	0.10	55.61	7.54
RD2	N	Aug 2017 - Sep 2020	30.94	4.08	2.41	0.10	55.16	7.31
		north section average	30.14	4.06	2.46	0.10	55.86	7.38
		Average	30.78	3.82	2.34	0.14	55.56	7.37

Table A2

Mass of Each Salt Used to Create the USU UWRL EQL Stock Solution

Salt	Desired M (g)	Actual M (g)	Actual M of Salt (g)
NaCl	46.95	46.95	46.94
MgCl26H2O	13.88	13.88	6.50
MgSO4	3.13	3.13	3.12
K2SO4	3.13	3.14	3.14
CaSO4	0.28	0.28	0.28
		Total M (g)	59.98
		Sample *TDS* (g/L)	299.89

Table A3

Mass of Salts Used to Create USU UWRL EQL Solutions of Varying Salt Concentration

Sample	1			2			3			4		
Salt	*M* (g)	Actual *M* (g)	Actual salt *M* (g)	*M* (g)	Actual *M* (g)	Actual salt *M* (g)	*M* (g)	Actual *M* (g)	Actual salt *M* (g)	*M* (g)	Actual *M* (g)	Actual salt *M* (g)
NaCl	46.95	46.95	46.95	21.91	21.91	21.91	18.78	18.80	18.80	15.65	15.65	15.65
MgCl2 6H2O	13.88	13.87	6.49	6.48	6.48	3.03	5.55	5.54	2.60	4.63	4.47	2.09
MgSO4	3.13	3.13	3.13	1.46	1.46	1.46	1.25	1.25	1.25	1.04	1.05	1.05
K2SO4	3.14	3.13	3.13	1.46	1.45	1.45	1.25	1.25	1.25	1.05	1.05	1.05
CaSO4	0.28	0.28	0.28	0.13	0.13	0.13	0.11	0.11	0.11	0.09	0.09	0.09
	Total *M* (g)		59.98	Total *M* (g)		27.98	Total *M* (g)		24.01	Total *M* (g)		19.92
	Sample *TDS* (g/L)		299.90	Sample *TDS* (g/L)		139.92	Sample *TDS* (g/L)		120.07	Sample *TDS* (g/L)		99.61

Sample	5			6			7		
Salt	*M* (g)	Actual *M* (g)	Actual salt *M* (g)	*M* (g)	Actual *M* (g)	Actual salt *M* (g)	*M* (g)	Actual *M* (g)	Actual salt *M* (g)
NaCl	12.52	12.51	12.51	9.39	9.40	9.40	6.26	2.26	6.26
MgCl2 6H2O	3.70	3.70	3.70	2.78	2.78	1.30	1.85	1.85	0.87
MgSO4	0.83	0.84	0.84	0.63	0.63	0.63	0.42	0.42	0.42
K2SO4	0.84	0.83	0.83	0.63	0.62	0.62	0.42	0.42	0.42
CaSO4	0.07	0.08	0.08	0.06	0.06	0.06	0.04	0.04	0.04
	Total *M* (g)		17.96	Total *M* (g)		12.00	Total *M* (g)		8.00
	Sample *TDS* (g/L)		89.79	Sample *TDS* (g/L)		60.02	Sample *TDS* (g/L)		40.00

Table A4

Data Sheet for the USU UWRL EQL Experiment Using the Stock Solution

*Sample	*TDS* (g/L)	*SC* (uS/cm)	Sample M (g)	Sample V (mL)	Sample ρ (g/cm^3)	$T(C)$	Corrected ρ (g/cm^3)	Repeat
1	300	217579	11.95	9.9	1.21	24.72	1.21	
2	290	221306	11.82	9.9	1.19	23.17	1.19	
2	290	220181	11.81	9.9	1.19	23.17	1.19	y
2	290	218258	11.80	9.9	1.19	23.17	1.19	y
2	290	216961	11.82	9.9	1.19	23.17	1.19	y
2	290	219612	11.80	9.9	1.19	23.17	1.19	y
2	290	220435	11.81	9.9	1.19	23.17	1.19	y
3	280	215626	11.72	9.9	1.18	23.12	1.19	
4	270	214979	11.62	9.9	1.17	22.2	1.17	
5	260	212705	11.60	9.9	1.17	22.06	1.17	
6	250	205187	11.52	9.9	1.16	21.85	1.16	
6	250	207500	11.50	9.9	1.16	21.85	1.16	y
6	250	206283	11.49	9.9	1.16	21.85	1.16	y
6	250	204718	11.48	9.9	1.16	21.85	1.16	y
6	250	207658	11.49	9.9	1.16	21.85	1.16	y
6	250	204015	11.48	9.9	1.16	21.85	1.16	y
7	240	199218	11.47	9.9	1.16	21.74	1.16	
8	230	195173	11.35	9.9	1.15	21.65	1.15	
9	220	188888	11.28	9.9	1.14	21.6	1.14	
10	210	184395	11.25	9.9	1.14	21.62	1.14	
10	210	185179	11.25	9.9	1.14	21.62	1.14	y
10	210	185607	11.20	9.9	1.13	21.62	1.13	y
10	210	183023	11.22	9.9	1.13	21.62	1.13	y
10	210	184882	11.20	9.9	1.13	21.62	1.13	y
10	210	184209	11.21	9.9	1.13	21.62	1.13	y
11	200	183269	11.16	9.9	1.13	21.5	1.13	
12	180	173360	11.11	9.9	1.12	21.5	1.12	
13	160	164160	10.94	9.9	1.10	21.37	1.11	
14	140	150648	10.84	9.9	1.10	21.38	1.10	
14	140	154581	10.80	9.9	1.09	21.38	1.09	y
14	140	148208	10.80	9.9	1.09	21.38	1.09	y
14	140	152917	10.81	9.9	1.09	21.38	1.09	y
14	140	153231	10.82	9.9	1.09	21.38	1.09	y

14	140	153837	10.84	9.9	1.10	21.38	1.10	y
15	120	138883	10.66	9.9	1.08	21.32	1.08	
16	100	120732	10.51	9.9	1.06	21.3	1.06	
17	80	101550	10.41	9.9	1.05	21.29	1.05	
17	80	102545	10.40	9.9	1.05	21.29	1.05	y
17	80	103452	10.41	9.9	1.05	21.29	1.05	y
17	80	103678	10.40	9.9	1.05	21.29	1.05	y
17	80	102961	10.44	9.9	1.05	21.29	1.05	y
17	80	99373	10.39	9.9	1.05	21.29	1.05	y
18	60	81394	10.30	9.9	1.04	21.46	1.04	
19	40	55092	10.14	9.9	1.02	21.77	1.03	
20	20	37787	10.01	9.9	1.01	21.28	1.01	

**Note.* This experiment was run on samples created by diluting the prepared stock solution, five repeat measurements were performed on sample 2, 6, 10, 14, and 17

Table A5

Data Sheet for the USU UWRL EQL Experiment on Separate Prepared Solutions

*Sample	*TDS* (g/L)	*SC* (uS/cm)	Sample M(g)	Sample V(mL)	Sample ρ (g/cm^3)	$T(C)$	Corrected ρ (g/cm^3)
1	300	221736	11.94	9.9	1.21	22.44	1.21
1	300	225803	11.90	9.9	1.20	22.44	1.20
1	300	226540	11.90	9.9	1.20	22.44	1.20
1	300	225784	11.95	9.9	1.21	22.44	1.21
1	300	222581	11.91	9.9	1.20	22.44	1.20
1	300	224835	11.89	9.9	1.20	22.44	1.20
2	140	156078	10.88	9.9	1.10	22.46	1.10
2	140	155035	10.86	9.9	1.10	22.46	1.10
2	140	160758	10.86	9.9	1.10	22.46	1.10
2	140	155845	10.87	9.9	1.10	22.39	1.10
2	140	156873	10.86	9.9	1.10	22.39	1.10
2	140	155578	10.87	9.9	1.10	22.39	1.10
3	120	146337	10.69	9.9	1.08	22.52	1.08
3	120	142045	10.71	9.9	1.08	22.52	1.08
3	120	141015	10.71	9.9	1.08	22.52	1.08
3	120	141466	10.81	9.9	1.09	22.56	1.09
3	120	145458	10.81	9.9	1.09	22.56	1.09
3	120	144065	10.72	9.9	1.08	22.56	1.08
4	100	128343	10.57	9.9	1.07	22.5	1.07
4	100	124312	10.59	9.9	1.07	22.5	1.07
4	100	127065	10.59	9.9	1.07	22.5	1.07
4	100	126646	10.58	9.9	1.07	22.42	1.07
4	100	127703	10.56	9.9	1.07	22.42	1.07
4	100	127218	10.56	9.9	1.07	22.42	1.07
5	80	107886	10.42	9.9	1.05	22.33	1.05
5	80	107412	10.43	9.9	1.05	22.33	1.05
5	80	106481	10.44	9.9	1.05	22.42	1.06
5	80	106484	10.44	9.9	1.05	22.42	1.06
5	80	103398	10.44	9.9	1.05	22.38	1.06
5	80	105790	10.42	9.9	1.05	22.38	1.05
6	60	84805	10.30	9.9	1.04	22.23	1.04
6	60	85683	10.28	9.9	1.04	22.23	1.04
6	60	83557	10.28	9.9	1.04	22.23	1.04
6	60	84413	10.29	9.9	1.04	22.23	1.04

6	60	81448	10.30	9.9	1.04	22.22	1.04
6	60	83700	10.29	9.9	1.04	22.22	1.04
7	40	59193	10.14	9.9	1.02	22.23	1.02
7	40	59061	10.16	9.9	1.03	22.23	1.03
7	40	58856	10.14	9.9	1.02	22.23	1.03
7	40	59377	10.15	9.9	1.03	22.26	1.03
7	40	58979	10.15	9.9	1.02	22.26	1.03
7	40	59020	10.14	9.9	1.02	22.26	1.02

**Note.* This experiment was performed on samples of varying concentration created individually, five repeat measurements were performed on each.

Appendix B. Water Activity Coefficient Table

Table B1

Water Activity Coefficient Values for a Range of Total Dissolved Solids and Temperatures

	T (°C)						
TDS (g/L)	-20	-10	0	10	20	30	40
0	1	1	1	1	1	1	1
50	0.974	0.973	0.973	0.973	0.973	0.973	0.973
100	0.944	0.943	0.942	0.941	0.941	0.94	0.94
150	0.907	0.905	0.903	0.902	0.901	0.9	0.9
175	0.885	0.882	0.88	0.878	0.877	0.877	0.876
200	0.859	0.856	0.854	0.852	0.851	0.85	0.85
225	0.829	0.826	0.824	0.822	0.821	0.821	0.821
250	0.795	0.792	0.79	0.788	0.788	0.788	0.789
275	0.755	0.752	0.751	0.75	0.751	0.752	0.753
300	0.709	0.707	0.707	0.708	0.709	0.712	0.714
325	0.656	0.656	0.658	0.661	0.664	0.668	0.672
350	0.595	0.599	0.603	0.608	0.614	0.62	0.626
375	0.528	0.535	0.542	0.55	0.559	0.568	0.577
400	0.454	0.465	0.476	0.488	0.5	0.513	0.526

Appendix C. GSL Hydroclimatic Data Collection Information

Figure C1

Forcing and Calibration Data Collection Site Map Including Locations of the Open Water Sampling Sites, Lake Elevation Gages, Inflow Gages, and Climate Stations

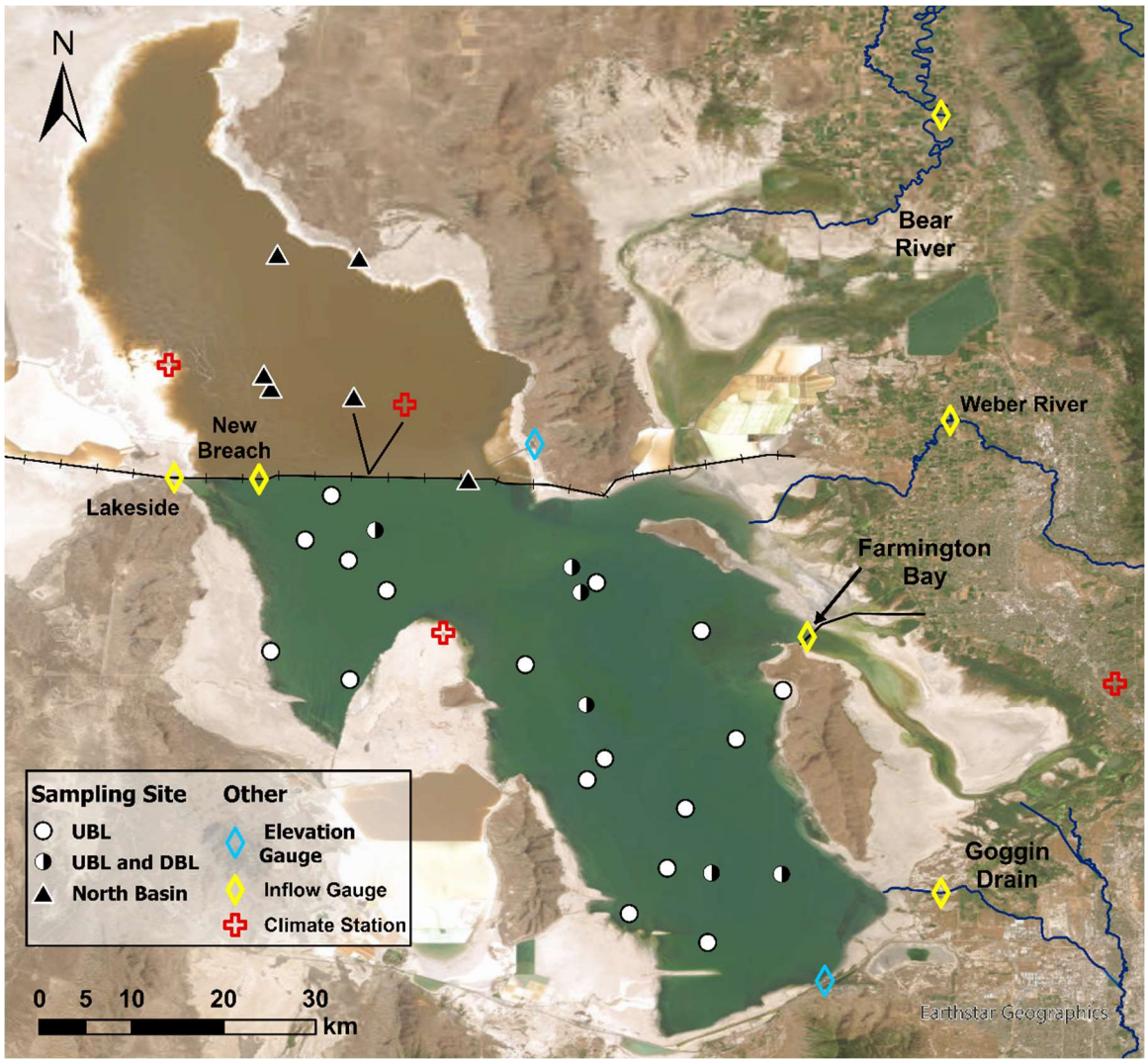

Figure C2

Time series of the Prepared Climate Data Used in Calculating Evaporation off the Great Salt Lake from Water Year 2020

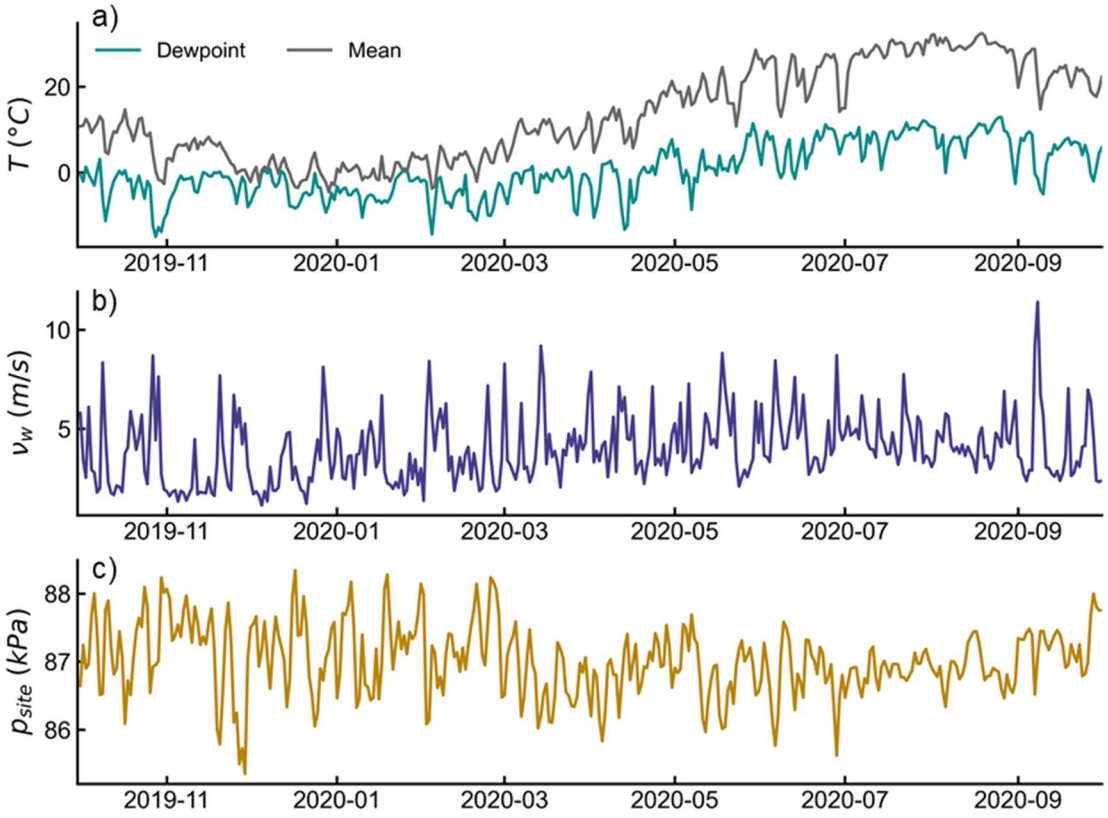

Table C1

Great Salt Lake Open Water Salinity Sampling Datasets

Layer	Number of Sites	Entities	ρ (g/cm^3)	*SC* (*µS/cm*)	*%C*
UBL	29	USGS, UGS, HDR, BSC, DWiR	✓	✓	✓
DBL	11	USGS, UGS, HDR, BSC	✓	✓	
North section	7	USGS, UGS, HDR	✓		

Table C2

Great Salt Lake Elevation and Climate Datasets

Entity	Site	Lat	Lon	Elevation (ft)	v_w (m/s)	p_{site} (kPa)	T_{max}, $T_{,min}$ (°C)	WSE (m)	Freq.
UCC	Hat Island	41.33	-112.85	4242.13	✓	✓	✓	✓	Hourly
	Gunnison Island	41.07	-112.59	4242.13	✓	✓	✓	✓	
	MARSH	41.22	-112.67	4212.93	✓	✓	✓	✓	
USGS	10010025	41.22	-112.77	4216.93	✓				15-minute
	10010100	41.26	-112.50	4189.8				✓	
	10010000	40.73	-112.21	4186.8				✓	

Table C3

Great Salt Lake Tributary and Causeway Exchange Datasets

Entity	Site	ID	Lat	Lon	Q_D (cfs)	Q_C (cfs)	SC_D (uS/cm)	SC_C (uS/cm)	ρ_D (g/cm^3)
USGS	Bear River near Corinne, UT	10126000	41.58	-112.85	✓	✓	✓	✓	✓
	Bear River Bay Bridge	10010060	41.23	-112.34	✓		✓		✓
	Weber River at Plain City, UT	10141000	41.28	-112.09	✓	✓	✓	✓	✓
	Goggin Drain	10172630	40.82	-112.10	✓	✓	✓	✓	✓
	Farmington Bay	41040112134801	41.07	-112.23	✓	✓	✓	✓	✓
	Lakeside	10010020	41.22	-112.85	✓		✓		✓
	WCB SN Flow	10010025	41.22	-112.77	✓		✓		✓
	WCB NS Flow	10010026			✓		✓		✓
USU	WCB South	--	41.22	-112.77				✓	✓
	WCB North	--						✓	✓

Note. "C" subscript represents 15-minute continuous measurements while "D" subscript represents discrete measurements